THESIS FOR THE DEGREE OF DOCTOR OF PHILOSOPHY IN THERMO AND FLUID DYNAMICS

Thermodynamic Cycles for Low- and High-Temperature Waste Heat Recovery from Heavy-Duty Engines

An Experimental and Simulation Study

JELMER RIJPKEMA

Department of Mechanics and Maritime Sciences
CHALMERS UNIVERSITY OF TECHNOLOGY

Gothenburg, Sweden 2021

Thermodynamic Cycles for Low- and High-Temperature Waste Heat Recovery from Heavy-Duty Engines
An Experimental and Simulation Study
JELMER RIJPKEMA
ISBN 978-91-7905-486-1

Doktorsavhandlingar vid Chalmers tekniska högskola
Ny serie nr. 4953
ISSN 0346-718X

Department of Mechanics and Maritime Sciences
Chalmers University of Technology
SE-412 96 Gothenburg
Sweden
Telephone: +46 (0)31-772 1000

Chalmers Reproservice
Gothenburg, Sweden 2021

Thermodynamic Cycles for Low- and High-Temperature Waste Heat Recovery from Heavy-Duty Engines
An Experimental and Simulation Study
Thesis for the degree of Doctor of Philosophy in Thermo and Fluid Dynamics
JELMER RIJPKEMA
Department of Mechanics and Maritime Sciences
Chalmers University of Technology

Abstract

To reduce the environmental impact of heavy-duty vehicles, it is critical to reduce their CO_2 emissions by improving the engine efficiency. A promising way to do this is by extracting waste heat from the engine during operation and converting it into useful work. This thesis presents a comprehensive evaluation of the performance of thermodynamic cycles for waste heat recovery from heavy-duty engines. First, by identifying the combination(s) of heat source, working fluid, and thermodynamic cycle that maximizes the performance. Then, by evaluating the performance of the most promising solutions using experimental investigations and detailed simulations.

The potential for waste heat recovery was investigated with steady-state simulations considering two low-temperature and two high-temperature heat sources, a wide variety of working fluids, and four thermodynamic cycles: the organic Rankine cycle (ORC), the transcritical Rankine cycle, the trilateral flash cycle, and the organic flash cycle. The best overall performance was obtained with the ORC using acetone, benzene, cyclopentane, ethanol, or methanol as the working fluid, or with R1233zd(E), MM, or Novec649 if a non-flammable and non-toxic fluid was preferred. The engine coolant was the best performing low-temperature heat source, recovering 1.5 % of the engine power, and the exhaust gas was the best performing high-temperature heat source, recovering up to 5 %. By combining multiple heat sources in series, almost 8 % was recovered. Using a dual-loop system with the engine coolant and exhaust gas as the heat source, fuel consumption was reduced by over 5 %, rising to 9 % if the engine coolant temperature was increased to 140 °C.

Two test setups were constructed to experimentally investigate the performance of the simulated systems. The high-temperature setup consisted of an Rankine cycle with water using the exhaust gases as the heat source while the low-temperature setup recovered heat from the engine coolant using an ORC with R1233zd(E) as the working fluid. Based on the experimental findings, models of both setups were developed to predict their performance over a driving cycle. The low-temperature system was able to recover 0.73 % of the total energy required by the engine, while the high-temperature system could recover 3.37 %.

Keywords: expander, heavy-duty Diesel, internal combustion engine, long haul truck, low-temperature, organic flash cycle, organic Rankine cycle (ORC), transcritical Rankine cycle, trilateral flash cycle, waste heat recovery

List of publications

This thesis is based on the work contained in the following publications:

Publication A J. Rijpkema, K. Munch and S. B. Andersson, "Thermodynamic Potential of Twelve Working Fluids in Rankine and Flash Cycles for Waste Heat Recovery in Heavy Duty Diesel Engines," *Energy*, 2018.

Publication B J. Rijpkema, S. B. Andersson and K. Munch, "Thermodynamic Cycle and Working Fluid Selection for Waste Heat Recovery in a Heavy Duty Diesel Engine," *SAE Technical Paper 2018-01-1371*, 2018.

Publication C J. Rijpkema, K. Munch and S. B. Andersson, "Combining Low- and High-Temperature Heat Sources in a Heavy Duty Diesel Engine for Maximum Waste Heat Recovery Using Rankine and Flash Cycles," *ETA 2018, Energy and Thermal Management, Air-Conditioning, and Waste Heat Utilization*, 2019.

Publication D J. Rijpkema, S. Thantla, J. Fridh, S. B. Andersson and K. Munch, "Experimental Investigation and Modeling of a Reciprocating Piston Expander for Waste Heat Recovery from a Truck Engine," *Applied Thermal Engineering*, 2020.

Publication E J. Rijpkema, O. Erlandsson, S. B. Andersson and K. Munch, "Exhaust Waste Heat Recovery from a Heavy-Duty Truck Engine: Experiments and Simulations," *Energy (Submitted)*, 2021.

Publication F V. Singh, J. Rijpkema, X. Li, K. Munch, S. B. Andersson and S. Verhelst, "Optimization and Evaluation of a Low Temperature Waste Heat Recovery System for a Heavy Duty Engine over a Transient Cycle," *SAE Technical Paper 2020-01-2033*, 2020.

Publication G J. Rijpkema, S. B. Andersson and K. Munch, "Experimental Results of an Organic Rankine Cycle with R1233zd(E) for Waste Heat Recovery from the Coolant of a Heavy-Duty Truck Engine," *Energy Conversion and Management (Submitted)*, 2021.

Publications not included in the thesis

Publication H J. Rijpkema, K. Munch and S. B. Andersson, "Thermodynamic Potential of Rankine and Flash Cycles for Waste Heat Recovery in a Heavy Duty Diesel Engine," *4th International Seminar on ORC Power Systems*, 2017.

Publication I J. Rijpkema, F. Ekström, K. Munch and S. B. Andersson, "Experimental Results of a Waste Heat Recovery System with Ethanol using the Exhaust Gases of a Light-Duty Engine," *5th International Seminar on ORC Power Systems*, 2019.

Publication J V. Singh, J. Rijpkema, K. Munch, S. B. Andersson and S. Verhelst, "On the Effects of Increased Coolant Temperatures of Light Duty Engines on Waste Heat Recovery," *Applied Thermal Engineering*, 2020.

Acknowledgements

I would like to start by thanking my "Swedish parents" Karin Munch and Sven Andersson. As my supervisors they made me feel welcome from the first day that I met them. It is a great feeling to know that your supervisors fully support you on both a professional and a personal level. I would also like to thank my project leader and the former head of the CaPS division, Ingemar Denbratt, for his support and especially for the opportunity to build my own experimental setup, an experience that will last a lifetime.

The opportunity to collaborate with industrial partners was not only insightful and valuable, but also a pleasure. For their collaboration, I would like to personally thank Arne Andersson, Fredrik Ekström, Henrik Salsing, Johan Linderyd, Jonas Aspfors, Ola Rolandson, Oliver Dingel, Olof Erlandsson, Sasan Sarmast, and Thomas Reiche. I also owe a big thank you to Sandhya Thantla from KTH and Vikram Singh from Lund University. Of course, I cannot forget Gunnar Latz whose support at the beginning of my PhD was a great help. The funding from the Energy Agency is also gratefully acknowledged.

Next in line are the research engineers, who fully deserve their title because experimental research would be impossible without them. Alf, Anders B., Lars, Patrik, Robert, and Tim, it was very nice to work with and learn from such highly skilled colleagues. Above all I enjoyed the good atmosphere; the best times during my PhD were spent in the lab. Special thanks go out to Anders Mattsson, who was as much part of this research as I was and who taught me the most during my years at Chalmers. It was a great pleasure to combine our skills and I enjoyed our technical discussions and pleasant collaboration.

I thoroughly enjoyed the nice atmosphere in our division. Long lasting "fikas", pizza lunches, and awesome after-works made our division great, so thanks to all of my colleagues. I am especially thankful to Marco for being a great roommate and always available for a nice discussion (or two), and to Michael, whose special skill at finding shortcuts always leads to interesting places. Our US trip was one of the best experiences during my time at Chalmers. Also, thank you, Gerben, Vignesh, Andreas, Zhiqin, Sreelekha, Mindaugas, and Dario for the good company. And thank you, Elenor, you are indispensable for our division.

Without the infinite support of my parents, Joke and Johannes, I would not have written this thesis. Their view of life made me who I am and I feel lucky to be a part of that. More gratitude goes to my brother, Douwe, and his lovely family, Jule, Lea, and Jannik as well as to my second family, Anne, Ron, Jeroen, Vincent, and Aimée. Of course, I would not be who I am without all the good friends in my life, so thank you for being there. If there is anybody that deserves gratitude for this thesis, it is my girlfriend Marleen. Her love and support gave me the foundation for completing this thesis and I could not have done it without her. Her dedication and priorities in life are an inspiration to me and I will strive to return the love that she showed me. And, finally, Maja. No words can express my gratitude for you. From now on, everything I do will be for you.

To Maja

The steam engine has done much more for science
than science has done for the steam engine

– Lord Kelvin

Nomenclature

A	area	(m^2)
AU	global heat transfer coefficient	(W/K)
c_p	specific heat capacity	(J/kg/K)
C_d	discharge coefficient	(-)
D	diameter	(m)
D_h	hydraulic diameter	(m)
f_a	supply cut-off ratio	(-)
f_p	exhaust cut-off ratio	(-)
h	specific enthalpy	(J/kg)
MW	molecular weight	(kg/kmol)
$\dot{m}$	mass flow rate	(kg/s)
N	rotational speed	(rpm)
Nu	Nusselt number	(-)
p	pressure	(Pa)
Pr	Prandtl number	(-)
$\dot{q}$	heat flux	(W/m^2)
Q	heat transfer	(J)
$\dot{Q}$	heat transfer rate	(W)
r_p	pressure ratio	(-)
Re	Reynolds number	(-)
s	entropy	(J/kg/K)
t	time	(s)
T	temperature	(K)
V	volume	(m^3)
V_s	swept volume	(m^3)
U	overall heat transfer coefficient	($W/m^2/K$)
$\dot{V}$	volume flow rate	(m^3/s)
W	work	(J)
$\dot{W}$	power	(W)
x	vapor quality	(-)

Greek symbols

α	heat transfer coefficient	($W/m^2/K$)
γ	heat capacity ratio	(-)
η	efficiency	(-)
ϵ	effectiveness	(-)
ϕ_f	filling factor	(-)
λ	thermal conductivity	(W/m/K)
μ	dynamic viscosity	(Pa.s)
ρ	density	(kg/m^3)
τ	torque	(Nm)

Subscripts

amb	ambient
bpv	bypass valve
c	cycle
ch	channel
cond	condenser
cool	coolant
corr	correction
cp	compression
crit	critical
el	electrical / element
eng	engine
evap	evaporator
ex	exhaust
exh	exhaust
exp	expander
fv	flash vessel
int	internal
is	isentropic
leak	leakage
liq	liquid
mech	mechanical
mxr	mixer
n	nominal
pmp	pump
pp	pinch point
sat	saturated
sh	shaft
si	sink
so	source
su	suction
sub	subcooled
sup	superheated
th	theoretical / thermodynamic
thr	throat
tv	throttling valve
vap	vapor
w	wall
wf	working fluid

Abbreviations

CAC	charge air cooler
BPV	bypass valve
BTE	brake thermal efficiency
CFD	computational fluid dynamics
EATS	exhaust aftertreatment system
EGR	exhaust gas recirculation
EGRC	exhaust gas recirculation cooler
ESC	European stationary cycle
HD	heavy-duty
HT	high-temperature
ICE	internal combustion engine
HW	highway
GHG	greenhouse gas
GWP	global warming potential
LD	light-duty
LT	low-temperature
ODP	ozone depletion potential
OEM	original equipment manufacturer
OFC	organic flash cycle
TFC	trilateral flash cycle
ORC	organic Rankine cycle
TRC	transcritical Rankine cycle
SV	safety valve
VFD	variable frequency drive
WHR	waste heat recovery
WHTC	world harmonized transient cycle

Contents

Part I
Extended Summary

1 Introduction

1.1 Motivation

Anthropogenic emissions of greenhouse gases (GHG), and particularly CO_2, have risen to levels without precedent in human history. This is having a widespread impact on human and natural systems, leading to warming of the atmosphere and oceans, diminishing snow and ice cover, and rising sea levels [1]. Fig. 1.1 shows how atmospheric CO_2 levels (plotted in black) and temperatures (plotted in orange) have evolved since 1850 [2].

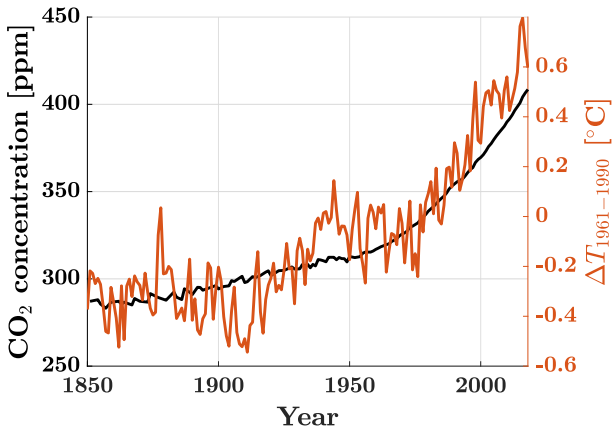

Fig. 1.1: The CO_2 concentration and the average atmospheric temperature deviation from the 1961 – 1990 baseline since 1850 [2].

A few economic sectors - industry, residential and commercial, energy, agriculture, and transport - are responsible for the majority of the GHG emissions worldwide. The relative contributions of these sectors within the European Union (EU) in 2017 [3] are shown in Fig. 1.2. The transport sector is one of the largest contributors, being responsible for over 25 % of all GHG emissions. Also visualized in Fig. 1.2 are the relative contributions of the different modes of transport: aviation, maritime, and road. The road transport contribution can be further broken down into contributions due to cars, light-duty (LD) trucks, and heavy-duty (HD) trucks and buses. This breakdown reveals that heavy-duty trucks and buses account for more than 5 % of the total GHG emissions in Europe [3]. This is similar to the contributions in the United States (US), where medium- and heavy-trucks are responsible for almost 6.5 % of all GHG emissions [4], and to the global contributions with emissions from heavy-duty road freight estimated at over 5 % of the total energy-related GHG emissions [5]. It is thus clear that reducing GHG emissions from heavy-duty trucks could significantly reduce overall GHG emissions.

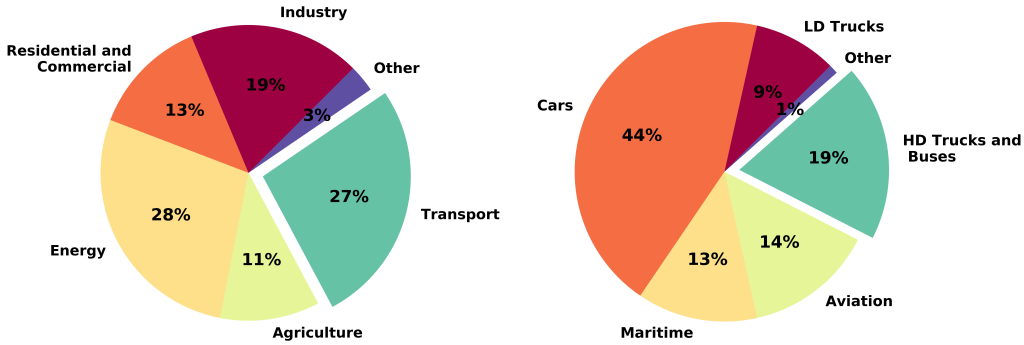

Fig. 1.2: GHG emissions for the EU in 2017 showing the relative contributions of major sectors (left) and the shares of the individual modes within the transport sector (right) [3].

Most vehicles within the transport sector are powered by an internal combustion engine (ICE). In an internal combustion engine, a fuel-air mixture is combusted and the subsequent expansion produces power that can be used to propel the vehicle. Nowadays, over 90 % of HD truck engines are Diesel engines, mainly because of the high energy density of Diesel fuel, the reliability and efficiency of the engines, and their high torque relative to their size [5]. Burning the fuel is the direct cause of CO_2 emitted to the atmosphere. These emissons can be reduced by improving the efficiency of the engine, which causes the fuel consumption at a given power level to be reduced. Accordingly, countries including the US, Canada, India, Japan, and China adopted mandatory fuel efficiency standards for heavy-duty vehicles [6]. Similarly, the EU recently adopted CO_2 emission standards for HD vehicles that require emissions to be reduced by 15 % from 2025 onward and 30 % from 2030 onward, relative to the 2019 baseline [7].

Although increasing the engine efficiency helps reduce GHG emissions from individual HD vehicles, it does not necessarily mean that the total emissions will decrease. In fact, an increase in efficiency could even increase the rate of resource consumption due to a rising demand; an effect known as *Jevon's paradox* [8]. Parallel increases in efficiency and GHG emissions have indeed been observed for HD vehicles: Fig. 1.3 shows that HD engine efficiencies have risen from 1990 onward, but so too have GHG emissions for the EU and US. In the EU, emissions have increased by approximately 20 % relative to the 1990 baseline [9] and projections suggest that emissions in 2050 will be 33 % higher than the 1990 baseline [3]. Furthermore, burning fossil fuels to propel vehicles is inherently unsustainable because fossil fuels are finite resources. Therefore, in the long-term, it will be necessary for HD vehicles to transition to powertrains that rely on hydrogen and electricity. However, it is currently expected that most HD vehicles will continue to be powered by internal combustion engines until at least 2050 [5]. Consequently, there is an urgent need for research and regulations to stimulate and facilitate the development and production of efficient engines for the coming years.

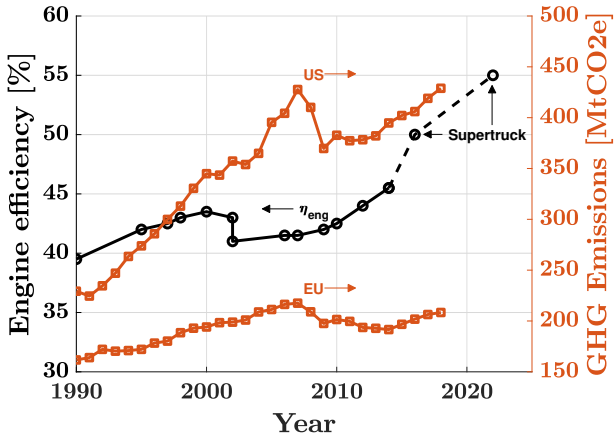

Fig. 1.3: In black, changes in heavy-duty engine efficiency since 1990. The two last points show the (estimated) outcomes of the Supertruck I and II research programs [10]. In orange, the GHG emissions in million tonnes of CO_2 equivalent for heavy-duty trucks and buses in the EU [9] and medium- and heavy-duty trucks in the US [11].

1.2 Scope

Engine efficiency is a measure of the proportion of the energy contained in the fuel that is converted into useful work. This energy is released when the fuel is mixed with air and combusted in the engine. Energy not converted into useful work is primarily dissipated to the environment in the form of heat. Thus, if an engine is 40 % efficient, 60 % of the energy in the fuel is lost as heat. Engine efficiency can be increased by altering the design of the engine so that less heat is lost. A more indirect way to improve the engine efficiency is to recover (a part of) the wasted heat and converting it into useful work. As the description suggests, this process is called waste heat recovery (WHR). One way to recover waste heat is to use a thermodynamic cycle, i.e. a system comprising a series of connected thermodynamic processes that is designed to transfer energy or produce work and ultimately returns to its initial state.

This thesis investigates the performance of thermodynamic cycles for waste heat recovery from heavy-duty truck engines with the purpose of increasing engine efficiency. The potential for waste heat recovery of different heat sources within the engine is assessed, where the heat sources are classified as either high-temperature or low-temperature, depending on the temperature of the available energy. The performance of the cycle and its separate components is evaluated for a variety of working fluids, using both simulations and experiments.

1.3 Research Questions

Within the domain of waste heat recovery from heavy-duty truck engines, four research questions were formulated to guide the work presented in this thesis:

- Which heat source(s) offer the greatest potential for waste heat recovery, taking into account both low- and high-temperature sources?
- According to simulations, which combination(s) of heat source, working fluid and thermodynamic cycle deliver the best thermodynamic performance?
- According to experiments, what is the actual performance of the combination of a heavy-duty Diesel engine and a waste heat recovery system, both for low- and high-temperature heat sources?
- What are the key aspects governing the thermodynamic performance of waste heat recovery systems for heavy-duty engines?

1.4 Outline

This introduction is followed by Chapter 2, which introduces the theoretical framework needed to understand waste heat recovery from engines, including the important aspects of the low- and high-temperature heat sources in a heavy-duty Diesel engine, the selected thermodynamic cycles, the main cycle components, and the working fluids. Chapter 3 describes the experimental setups used in this thesis, which include two different heavy-duty Diesel engines, a high-temperature waste heat recovery setup, and a low-temperature waste heat recovery setup. Chapter 4 explains the two approaches used to model thermodynamic cycles: 0D modeling for evaluating the thermodynamic performance and 1D modeling for more detailed evaluation of the performance of individual components, which were calibrated and validated against the experimental results. Chapter 5 summarizes the publications included in this thesis and their findings. This is followed by a discussion of the findings in Chapter 6, which focuses primarily on comparing waste heat recovery from low- and high-temperature heat sources, the effect of elevated coolant temperatures, and heat rejection from a truck. Finally, Chapter 7 and 8 conclude the thesis by highlighting the most relevant findings and by offering suggestions for further research on waste heat recovery systems for heavy-duty engines.

2 Waste Heat Recovery from Engines

Waste heat recovery enables the transformation of waste heat into other useful forms of energy without requiring the input of additional electrical energy and is regarded as an effective technology for green and sustainable development in various industries [12]. For example, organic Rankine cycles (ORC) for waste heat recovery have been commercially operated since 1995 using energy sources such as biomass combustion, geothermal heat, solar radiation, or industrial waste heat [13]. The idea of recovering waste heat from engines is also not new: in 1976, Patel and Doyle [14] reported an experimental study on an ORC for recovering waste heat from the exhaust gases of a heavy-duty engine. Based on their test results they concluded that a system with optimal components should be able to improve fuel economy by 15 % over a duty cycle. Today, these figures seem optimistic: most modern studies suggest that the achievable reductions in fuel consumption are between 2 and 10 % [15–17].

The interest for waste heat recovery from internal combustion engines has not been purely academic either. Most automotive OEMs have already investigated and developed prototype systems, although no commercial application has been realized. In 2007, Honda [18] tested an ORC for recovering heat from the exhaust gases of a hybrid vehicle. Similarly, in 2008 and 2012, BMW [19, 20] conducted experimental studies on heat recovery from the coolant and exhaust gases using the ORC. More recently, Volkswagen [21] and Volvo Cars [22, 23] have presented results on ORC systems for waste heat recovery in hybrid vehicles. There has also been industrial interest in waste heat recovery for heavy-duty applications. In the US, several organizations and universities are participating in the Supertruck II program [24], an initiative to improve the brake thermal efficiency (BTE) of heavy-duty engines using waste heat recovery among other technologies. In this program, Cummins, Daimler, and Peterbilt [15] aim to improve the BTE from 50 to 55 % with waste heat recovery as one of the key pathways. Other OEMs that have expressed interest in the topic include MAN [21], Scania [25], and Volvo Group [26].

The purpose of this chapter is to establish the theoretical foundations needed to understand the rest of the thesis. Section 2.1 provides a brief overview of the heavy-duty engine and its most relevant engine operating points and heat sources as well as several waste heat recovery methods for engines. Section 2.2 explores thermodynamic cycles for waste heat recovery in more detail. This is followed by a description of the main cycle components in Section 2.3 and the key properties of working fluids in Section 2.4.

2.1 Internal Combustion Engines

In an internal combustion engine fuel is burned or oxidized in order to convert the chemical energy contained in the fuel into mechanical power [27]. The first successful internal combustion engines were created by modifying steam engines, but dedicated designs soon appeared: in 1876, Nikolaus Otto successfully implemented the four-stroke process in stationary spark-ignition engines and in 1886, Karl Benz and Gottlieb Daimler independently developed the light, high-speed engine from which most modern gasoline engines are descended [28]. Six years later, Rudolf Diesel patented a new kind of internal combustion engine that is now known as the Diesel or compression-ignition engine [27]. Initially used only for stationary applications, the Diesel engine entered mass production in the 1920s [29] and has since become one of the world's most widely used engine types. Today, a great variety of Diesel engines, both naturally-aspirated and turbocharged, are used for power generation and the propulsion of automobiles, trucks, locomotives, and marine vessels [27]. Engines for vehicle applications are usually categorized as light-duty (LD), medium-duty (MD), or heavy-duty (HD), based on their vehicle weight classifications [30]. This thesis focuses on heavy-duty Diesel engines for long haul trucks.

The basic lay-out of a heavy-duty Diesel engine is depicted schematically in Fig. 2.1. Ambient air entering the engine is compressed by the turbocharger compressor and cooled by the charge air cooler (CAC) before entering the cylinders. Fuel is then injected into the cylinders and the fuel-air mixture is compressed, causing it to ignite and release its energy. Some of the energy released during combustion is transferred to the coolant. After combustion, the exhaust gas leaves the cylinders. A portion of the exhaust gas is cooled in the exhaust gas recirculation cooler (EGRC), mixed with the intake air, and returned to the cylinders. The remainder is expanded in the turbocharger turbine and leaves the exhaust via the exhaust aftertreatment system (EATS), still containing a substantial amount of useful energy.

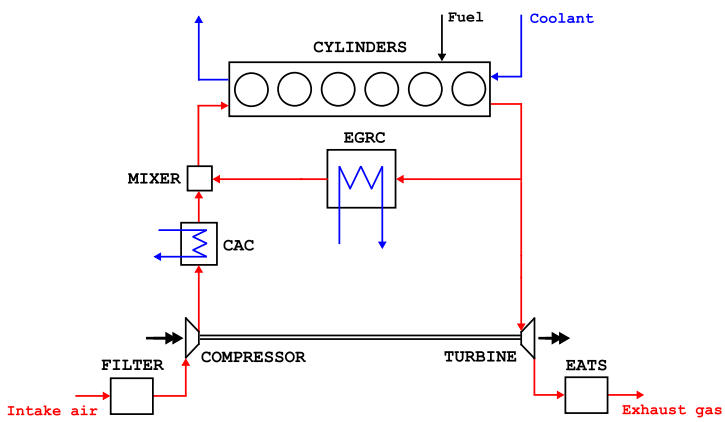

Fig. 2.1: Schematic depiction of a heavy-duty Diesel engine with exhaust gas recirculation.

The operating conditions of an engine are determined by its operating point, i.e. its speed and load. Engine operating points are commonly referred to using the classification of the European stationary cycle (ESC) even though the ESC has been superseded by the world harmonized stationary cycle (WHSC) as a test cycle for emission measurements. Under this classification, the engine speed is indicated by one of the letters A, B, or C, corresponding, respectively, to low, intermediate, and high speed. The engine load is indicated by a number (25, 50, 75, or 100), which corresponds to the percentage of the engine's maximum load at the engine speed indicated by the preceding letter. During a test cycle, an engine must be operated for a prescribed time at different operating points; its emissions are measured at each point and averaged over the cycle using a set of weighting factors [31], as shown on the left of Fig. 2.2. However, while the ESC weighting factors are used for emission certification, they do not accurately reflect the relative amounts of time spent at the corresponding operating point during a typical real driving cycle. Fig. 2.2 also shows the weighting factors for the ESC operating points that reflect the actual relative amount of time spent at each operating point during a typical high-way driving cycle for a long haul truck [32].

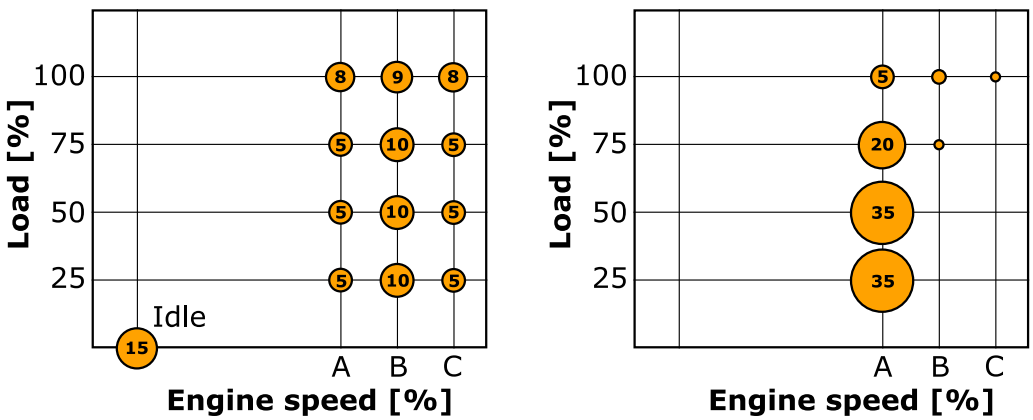

Fig. 2.2: Weighting factors for different operating points in the European stationary cycle (left) and a typical long haul driving cycle (right).

To reduce the adverse impact of transportation on the environment, considerable effort has been invested into finding ways to the reduce emissions of the internal combustion engine, such as CO_2, NO_x, particulate matter, and unburned hydrocarbons. CO_2 emissions can be reduced by increasing engine efficiency and thereby reducing the brake specific fuel consumption (bsfc). Many different strategies for increasing the efficiency of heavy-duty engines have been investigated, including combustion efficiency improvements, cylinder deactivation, using renewable fuels, predictive powertrain control, reducing losses, waste heat recovery, and hybridization [15, 33–35]. Future concepts that may further increase the efficiency include full electrification, hydrogen combustion, fuel cell vehicles, and free piston engine generators [5, 36].

2.1.1 Waste Heat Recovery Methods

Several technologies exist that could potentially be used to increase engine efficiency via waste heat recovery. Four options that have attracted particular research interest for heavy-duty engines are introduced below.

Turbocompounding

In a turbocompound engine, an extra power turbine is added downstream of the turbocharger turbine to extract energy from the exhaust gases. The extra turbine is driven directly by the exhaust gases and can be either coupled to an electric generator or mechanically coupled to the engine. Mechanical coupling requires an extra reduction gear drive, which increases the complexity and costs of the system. Electrical coupling has the advantage that the turbine speed becomes independent of the engine speed, although the additional generator increases costs and adds to the packaging [37]. The main drawback of turbocompounding is that it increases back-pressure in the exhaust manifold, meaning that the engine must do more work to expel the exhaust gases and thus reducing engine efficiency. Its advantages include relative simplicity, low volume, and low cost [38]. Turbocompounding is used in a number of commercial heavy-duty engines produced by manufacturers including Detroit Diesel, Iveco, Volvo, and Scania. The current technology shows the potential for fuel consumption reductions between 1 and 5 % [38–40]. However, such reductions are not achieved under all operating conditions; at low engine load, turbocompounding may even cause a slight increase in fuel consumption [40].

Thermoelectric generators

A thermoelectric generator (TEG) is a solid-state device that transforms heat into electricity by means of the Seebeck effect, which is the ability of a material to produce current when submitted to a temperature gradient [39]. While the major drawback of TEGs is their low thermodynamic efficiency (< 4 %) [41], their small packaging, lack of moving parts, and direct conversion of heat to electrical energy make them attractive for automotive applications [42]. Experimental studies on a Scania prototype truck with two TEGs showed that up to 1 kW of electrical power could be generated over a range of engine operating points [43]. In another experimental study, He et al. [44] used a TEG for waste heat recovery from the exhaust gases of a heavy-duty Diesel engine, obtaining up to 1.4 kW of electrical power and a thermodynamic efficiency of around 4 % over the world harmonized transient cycle (WHTC).

Thermoacoustic engines

A relatively new WHR technology is the thermoacoustic engine (TAE), which converts heat energy into high amplitude acoustic waves and subsequently into electric power. TAEs have the main advantage that they can be used wherever a suitable heat source exists. The onset temperature difference required for the device to start producing power depends on its design and operating conditions, but it can be relatively low compared to other technologies [45]. TAEs have been studied extensively over the years in contexts including cryogenic, cold generation, heat pumps, electric power generation, and waste heat recovery; they have also recently been considered for waste heat recovery in automotive applications [46]. Simulations suggested that a maximum acoustic power of almost 0.5 kW could be obtained with a thermodynamic efficiency of 13 % in a heavy-duty engine [47]. In another simulation study, the same authors predicted a maximum acoustic power of more than 2 kW in heavy-duty applications [48].

Thermodynamic cycles

Among the most promising technologies for waste heat recovery are those that use thermodynamic cycles to capture heat from the engine during operation and convert it into useful power. Different cycles have been studied and since these technologies are the focus of this thesis, they are discussed in detail in Section 2.2.

2.1.2 Heat Sources

A heavy-duty engine has four major sources that could potentially be targeted for waste heat recovery: the CAC, the coolant, the EGRC, and the exhaust gases. The potential of a heat source not only depends on the quantity of the available energy but also on the quality, which is reflected by its temperature. The EGRC and exhaust gases are classified as high-temperature heat sources, while the CAC and engine coolant are classified as low-temperature sources. The maximum quantity of energy available from the heat source can be calculated by subtracting the energy under ambient conditions from the energy under exhaust outlet conditions:

$$\dot{Q}_{\text{loss}} = \dot{m}_{\text{exh}}(h_{\text{exh,out}} - h_{\text{amb}}) \tag{2.1}$$

The quality of an energy flow can be evaluated by converting it into an exergy flow based on the mean temperature ($\overline{T}$) at which the energy is available [49]:

$$\dot{X}_{\text{loss}} = \dot{Q}_{\text{loss}} \frac{\overline{T} - T_{\text{amb}}}{\overline{T}} \tag{2.2}$$

To illustrate the amounts of available quantity and quality from the different heat sources over the full operating range of a heavy-duty Diesel engine, the ranges of the relative contributions of the heat losses and exergy losses are visualized in Fig. 2.3. These ranges, taken from an heavy-duty engine model [50], show that the sources with the most pronounced differences between their relative heat and exergy loss are the coolant (due to its relatively low temperature between 80 and 95 °C) and the EGRC (due to its relatively high temperature between 400 and 600 °C). The temperature of the CAC is typically between 100 and 200 °C, while that of the exhaust gases is usually between 200 and 350 °C. The label Other represents other heat losses in the engine, primarily heat losses in the exhaust piping and the EATS.

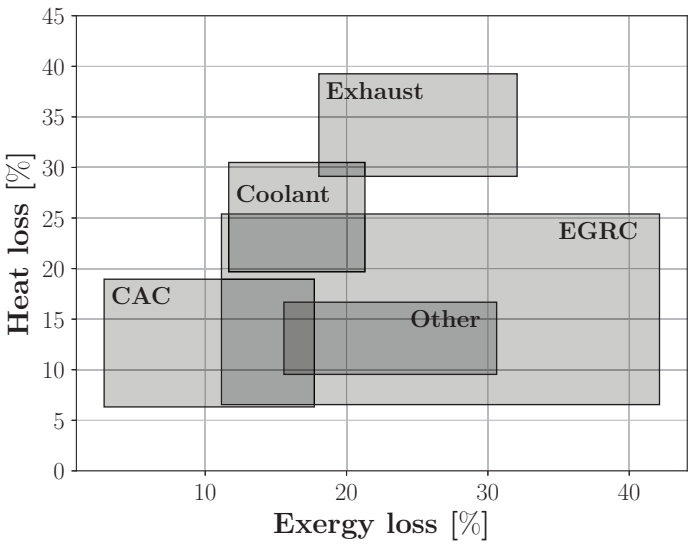

Fig. 2.3: Heat loss and exergy losses for the different heat sources in a heavy-duty Diesel engine over its full operating range [50].

2.2 Thermodynamic Cycles

The use of thermodynamic cycles for waste heat recovery from energy sources including geothermal, solar, biomass, industrial heat, and internal combustion engines has been studied extensively [13]. Thermodynamic cycles consist of sequences of thermodynamic processes involving heat transfer and work so that the system undergoes various changes in temperature and pressure before returning to its original state. Some of the heat taken from heat source is converted into mechanical work while the rest is rejected to a heat sink. This section provides an overview of major areas of research on waste heat recovery from engines using thermodynamic cycles, with particular emphasis on the last four cycles as these were selected for further investigation in the remainder of this thesis.

2.2.1 Brayton Cycle

The Brayton cycle involves adiabatic compression of a gas using a compressor, heat addition at constant pressure, adiabatic expansion in a turbine (typically coupled to the compressor), followed by cooling at constant pressure. Advantages of this cycle include a low number of moving parts, vibration-free operation, high durability, low weight, and good compatibility with vehicle electrification strategies. In addition, the Brayton cycle is readily integrated into existing engine designs because of the ability to use ambient air as the working fluid. Unfortunately, its low efficiency in automotive applications is a major barrier to its practical use in current applications [51]. A simulation based study on the use of an inverted Brayton cycle for WHR from the exhaust gases of a 3.0 L Diesel engine was reported by Di Battista et al. [52], who found that mechanical recoveries of up to 3.5 % were possible. The Brayton cycle could also be used for WHR from the exhaust gases of a series hybrid electric vehicle; simulations conducted by Nader et al. [51] suggested that the fuel economy of a 1.2 L gasoline engine could be improved by up to 7.0 % in this way. A case involving a larger engine was studied by Uusitalo et al. [53], who used simulations to evaluate the performance of a supercritical Brayton cycle with different working fluids for WHR from an 18 MW Diesel engine and obtained a maximum predicted electrical output of 1.8 MW.

2.2.2 Stirling Cycle

A Stirling engine is a heat engine that operates in a closed cycle connecting two heat reservoirs. The engine consists of three main parts: a hot volume, a cold volume, and a regenerator [54]. The compressible working fluid in a Stirling cycle engine (which may be air, helium, hydrogen, or nitrogen among other gases) undergoes periodical compression and expansion at different temperatures to convert thermal energy into mechanical work [55]. The reliability, efficiency, and specific work output of a Stirling engine are significantly lower than those for the organic Rankine cycle (ORC; see below) over any given temperature range, but its been suggested as an alternative to the ORC for WHR in vehicles because of its simplicity and compactness, high thermodynamic

efficiency, and silent operation [54]. Güven et al. [54] simulated WHR from the exhaust gases of a 315 kW, 10.7 L heavy-duty Diesel engine using a Stirling engine and found that the studied system generated a mechanical power output of around 3 kW, corresponding to over 1.3 % of the engine's power or a fuel consumption reduction of around 1 %.

2.2.3 Kalina Cycle

In a Kalina cycle, a multicomponent (zeotropic) mixture is used as the working fluid. The concentration of the working fluid is varied over the cycle by supplementing condensation with absorption [56]. The use of a zeotropic mixture results in non-isothermal evaporation and condensation, potentially allowing the working fluid to achieve a good thermal match with both the heat source and the heat sink [57]. Consequently, the Kalina cycle can have quite high thermodynamic efficiencies. Despite the higher efficiencies, drawbacks of the cycle include high system complexity and cost [58]. Larsen et al. [57] showed that an enhanced Kalina cycle known as the Split-cycle could reach thermodynamic efficiencies of up to 23 % for WHR from the exhaust of a large marine Diesel engine using an ammonia/water mixture as the working fluid. Similarly, Mohammadkhani et al. [59] conducted simulations to evaluate the performance of a Kalina cycle for WHR from a 99 kW, 5.7 L Diesel engine. Their system consisted of a single-loop configuration with an ammonia/water mixture as the working fluid extracting heat from both the coolant and the exhaust gases. The predicted power recovery using this system was up to 22 kW at maximum engine power.

2.2.4 Organic Rankine Cycle

In a conventional Rankine cycle, water is pressurized, evaporated, and superheated before being expanded in a turbine and condensed. The organic Rankine cycle (ORC) is similar to the Rankine cycle, but uses a refrigerant or organic liquid as the working fluid instead of water. This has the advantage of making the technology compatible with virtually any external thermal energy source; it can operate with temperature differences between the heat source and sink ranging from approximately 30 to 500 °C [13]. Other advantages of the ORC include high flexibility, safe operation, low maintenance requirements, and good thermodynamic performance [60]. The ORC already established itself as a technology for generating power by converting heat from low- to medium-temperature heat sources [13], and several ORC manufacturers (e.g., Turboden, Opcon Powerbox, Orcan, and EXERGY) produce units for commercial stationary applications in various industrial sectors [39]. Numerous experimental and simulation studies have been conducted to evaluate the performance of the ORC for WHR from heavy-duty engines. The exhaust gases are favored as a heat source but the potential of the other heat sources (the CAC, the coolant, and the EGR cooler) has also been investigated; typical reported fuel consumption improvements are between 2 and 10 % [16, 17, 41, 60–64].

The main processes of the ORC are illustrated on the right of Fig. 2.4 and the corresponding temperature-entropy (Ts) diagram is shown on the right.

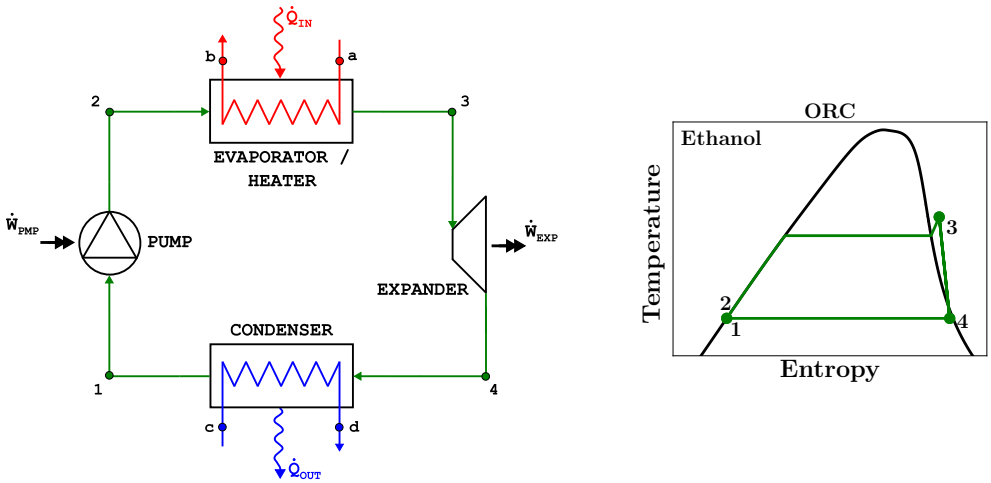

Fig. 2.4: Schematic overview of the ORC and the corresponding Ts-diagram.

The ORC involves a sequence of physical processes that are performed by the different components of the cycle: the pump, the evaporator, the expander, and the condenser. The thermodynamic processes performed by each component are described below, where the numbering of steps correspond to that used in Fig. 2.4. A more detailed treatment of the different components is provided in Section 2.3.

Pump ($1 \rightarrow 2$)

The main function of the pump is to pressurize the fluid by compressing it; the fluid enters the pump as a low-pressure liquid and exits as a high-pressure liquid. For simulations, it is sufficient to set inlet pump conditions equal to saturated liquid conditions. However, in practical systems a small amount of subcooling is needed to ensure that the fluid is in the liquid state at the pump inlet. In some cases, it may be necessary to have a significant amount of subcooling to avoid cavitation in the pump. In the Ts-diagram it is difficult to distinguish between point 1 and 2, because the isobars for liquid are very closely spaced.

Evaporator ($2 \rightarrow 3$)

The high pressure liquid from the pump enters the evaporator, where the heat is transferred from the heat source (a $\rightarrow$ b) to the working fluid ($2 \rightarrow 3$). During this process the heat source should provide enough energy to preheat, evaporate, and superheat the working fluid (corresponding to transitions from subcooled to saturated liquid, then to saturated vapor, and finally to superheated vapor). The main difference between the ORC and the other cycles studied in this thesis is in the evaporation process. In the ORC, the

fluid phase changes from liquid to vapor at a fixed pressure and temperature during evaporation. A small amount of superheating is necessary to ensure full vaporization of the fluid. For wet fluids (see Section 2.4) additional superheating may improve the performance and could even be necessary to prevent an excessively high liquid content at the end of expansion.

Expander (3 → 4)

The superheated working fluid leaving the evaporator enters the expander, where the high-pressure, high-temperature vapor expands, converting part of its thermal energy to mechanical movement that can in turn be converted into power.

Condenser (4 → 1)

In the condenser, the working fluid transitions to the subcooled liquid state (4 → 1) by rejecting the heat to the heat sink (c → d). Depending on the working fluid, it will enter the condenser either as a superheated vapor (at low pressure) or a two-phase mixture.

2.2.5 Transcritical Rankine Cycle

The transcritical Rankine cycle (TRC) has the same basic components as the ORC (see Fig. 2.4). The difference is that the working fluid is pressurized above its critical pressure at the pump outlet and therefore exists in a supercritical state with no clear distinction between liquid and vapor phases. Consequently no evaporation takes place between point 2 and 3, as shown in Fig. 2.5. In a transcritical cycle, the working fluid at high pressure is under supercritical conditions and under subcritical conditions at low pressure whereas in a supercritical cycle the fluid is in the supercritical state irrespective of the pressure.

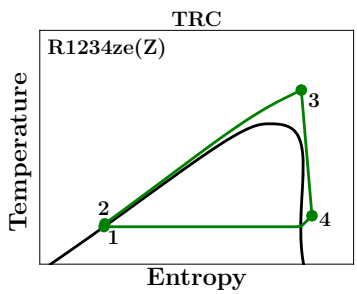

Fig. 2.5: Ts-diagram of the TRC.

Under supercritical conditions, the working fluid is not constrained to a fixed temperature interval; instead, its temperature increases gradually in the heater (2 → 3). The resulting temperature slope potentially allows for a better match with the heat source temperature profile, resulting in improved heat transfer and possibly better cycle performance. Additionally, avoiding the two-phase region during heat transfer allows the use of more

compact heat exchangers. The drawbacks of supercritical operation are the relatively high operating pressures, control difficulties related to operation close to the critical point, and potential issues relating to the thermal stability of organic fluids [40]. However, one of the most popular working fluids for the TRC is CO_2, which does not suffer from thermal instability [65]. Shi et al. [66] experimentally compared four CO_2-based TRC systems for WHR from a 243 kW, 8.4 L heavy-duty Diesel engine using an expansion valve instead of an expander. Based on their results, they estimated a maximum net power output of 3.5 kW. In a more recent simulation study using the same engine as the heat source, Li et al. [65] showed that a TRC with CO_2 could reduce fuel consumption by up to 2.3 %.

2.2.6 Trilateral Flash Cycle

The trilateral flash cycle (TFC) uses the same components and operating principles as the ORC (see Fig. 2.4). However, as shown in Fig 2.6, the working fluid is only heated to its liquid saturation point before being expanded (2 → 3) rather than being superheated.

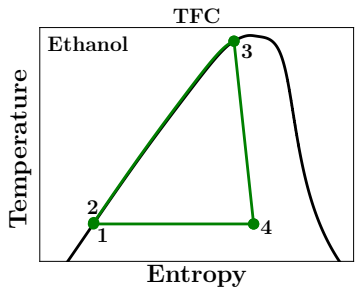

Fig. 2.6: Ts-diagram of the TFC.

Because the working fluid is in the saturated liquid state at the start of the expansion, the fluid remains in two-phase throughout the expansion process. Although experimental results for a two-phase expander with up to 76 % isentropic efficiency have been published [67], the lack of a commercially available efficient two-phase expanders is a significant impediment to the wider use of this cycle [68]. Choi et al. [69] simulated the TFC using water in combination with an ORC using R1234yf in a dual-loop configuration for WHR from the exhaust gases of a 69 MW marine engine. Their results indicated a maximum power output of over 2 MW, leading to a 2.8 % improvement in engine efficiency.

2.2.7 Organic Flash Cycle

The organic flash cycle (OFC) combines the principles of the ORC and TFC by flashing the saturated liquid to an intermediate pressure. It was originally developed for geothermal applications [70] and was later modified and enhanced to use for waste heat recovery [71, 72]. A schematic of the OFC is presented on the left of Fig. 2.7 with the corresponding Ts-diagram on the right.

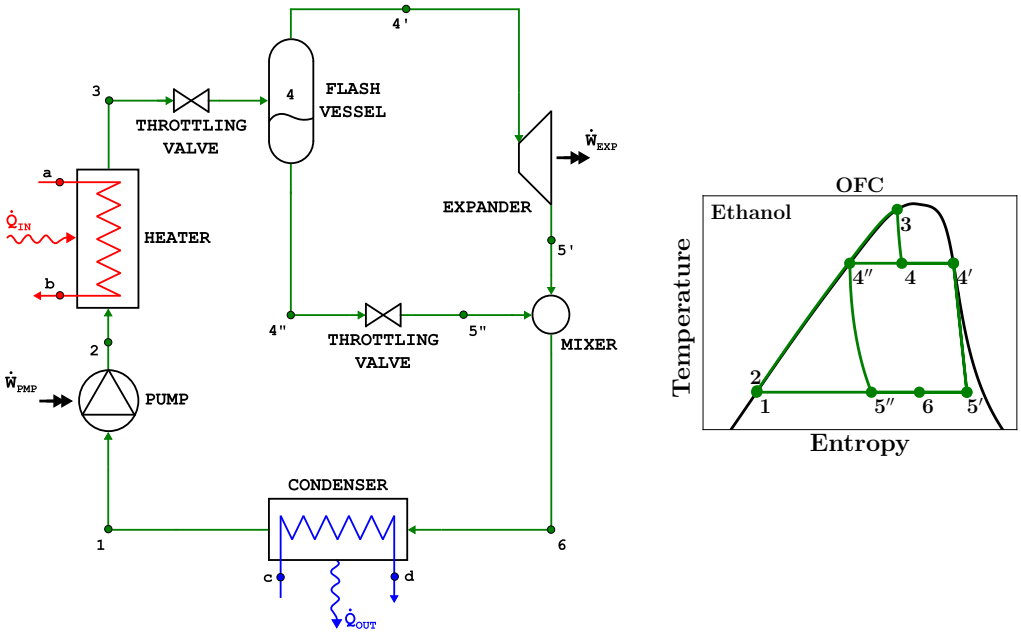

Fig. 2.7: Schematic overview of the OFC and the corresponding Ts-diagram.

In the OFC, like the TFC, the working fluid is compressed and heated to its liquid saturation point ($1 \rightarrow 3$). However, the TFC has a number of components not used in the ORC, which are described below.

Flash vessel ($3 \rightarrow 4$)

Instead of expanding directly as saturated liquid, the fluid is flashed to a lower pressure using a throttling valve. This creates a two-phase mixture that is separated in the flash vessel. The liquid part continues to the throttling valve, while the vapor enters the expander. The use of the intermediate pressure and flash vessel avoids the wet expansion at the cost of a reduced pressure and mass flow.

Throttling valve (4" $\rightarrow$ 5")

The pressure of the liquid in the flash vessel must be reduced before it enters the condenser; this is achieved using a second throttling valve that causes the the saturated liquid to become a two-phase mixture.

Mixer (5', 5" $\rightarrow$ 6)

The flows from the expander and the liquid throttling valve are mixed before they enter the condenser.

2.3 Cycle Components

Thermodynamic systems for waste heat recovery consist of many different components, but the ORC-derived cycles discussed in the preceding section all have four main components: the pump, the evaporator and condenser, and the expander.

2.3.1 Pump

Although configurations have been explored where the pump is directly coupled to the engine crankshaft [73] or the expander [74], the pump is almost always controlled via its own electric motor. Independent pump speed control maximizes the flexibility for controlling the mass flow rate of the working fluid, which improves the pump response. In addition, there are no restrictions on the location of the pump if it is not coupled to another device, which makes system packaging and integration easier [17].

Pumps for ORC applications are generally modeled by assuming a constant estimated pump efficiency without any detailed supporting study on the real performance of the pump under different operating conditions [75]. The efficiency is generally estimated to be quite high (between 65 % and 85 % [75]) compared to the reported experimental values, which are between 10 % and 50 % [76–78]. Accurate estimates of pump efficiency are crucial for small WHR systems because the power consumption of the pump can significantly affect the net power output, especially for low-temperature applications.

2.3.2 Heat Exchangers

Heat exchangers for WHR systems come in many shapes and types, including shell and tube, finned plate, and finned tube designs. They are typically characterized by their flow arrangement, e.g. parallel-flow, counter-flow, or cross-flow [79]. Shell and tube heat exchangers are generally used in large-scale applications, whereas finned plate heat exchangers are used in small-scale applications due to their compactness [17]. When designing heat exchangers, there is a trade-off between heat transfer and pressure drop: efforts to enhance heat transfer typically result in larger pressure drops [65]. The pressure drop across the heat exchangers is often ignored when modeling the WHR system. However, it is important to note that in reality the pressure drop can reduce the ORC system performance, especially in space-constrained applications where it is necessary to restrict the heat exchanger size while tolerating higher pressure drops [65]. Three different types of heat exchanger are used in the thermodynamic cycles examined in this thesis: the evaporator, the condenser, and possibly a recuperator.

Evaporator

The evaporator is located between the pump and the expander; its purpose is to transfer heat from the heat source to the cycle and to preheat, evaporate and superheat the fluid before it enters the expander. For automotive applications it is especially important to have a small pressure drop in the evaporator. For example, when recovering heat from the exhaust gases, the added pressure drop causes increased backpressure, leading to higher fuel consumption [80]. Additionally, in the case of coolant heat recovery, the pressures in the cycle are so low that an added pressure drop can significantly reduce performance.

Condenser

The condenser is located between the expander and the pump; its purpose is to condense and subcool the working fluid. For stationary applications and in engine test cells, the condenser is cooled by process water. In an automotive application, it can be cooled either by direct or indirect condensation. Direct condensation means that the working fluid is cooled by a radiator that in turn is cooled by air, either the ram air or the air flow from a radiator fan. Indirect condensation systems have an intermediate fluid, typically engine coolant, that takes the heat from the cycle and rejects it via the radiator, using either the engine's existing cooling system or a dedicated one. The size of the front heat exchanger is limited by the available space and depends on the presence of an engine radiator and possibly also a charge air cooler, EGR cooler, or air-conditioning condenser [78].

Recuperator

The recuperator transfers the heat from the working fluid at the expander outlet to the working fluid at the pump outlet. The recuperator increases the heat available for the cycle and reduces the amount of heat rejected to the environment through the condenser [81]. A recuperator can only be used if the expander outlet temperature is higher than the pump outlet temperature, which depends on the cycle conditions and the working fluid.

2.3.3 Expander

The expander converts the available energy in the working fluid into electrical or mechanical power, depending on the coupling. Although electrical coupling is associated with higher overall losses than mechanical coupling because of generator, storage, and supply losses, it allows the expander speed to be controlled independently. This optimizes the performance and the energy can be stored or used at the most convenient time. The best of both worlds can be obtained by adding a clutch to enable switching between mechanical and electrical coupling [22], although this increases the costs and complexity. Two types of expanders exist: the velocity type (or turbo-expander) and the volumetric type (or positive displacement expander) [82]. The most common velocity type expanders are axial and radial turbines, while the most common volumetric types are screw, scroll, piston, and vane expanders [17, 83]. Volumetric type expanders typically have lower flow rates, higher pressure ratios, and much lower rotational speeds than the velocity type [78].

2.4 Working Fluids

The performance of the thermodynamic cycle depends heavily on the choice of working fluid. Many different classes of working fluids are available, including hydrocarbons (HC), perfluorocarbons (PCF), chlorofluorocarbons (CFC, HCFC), hydrofluorocarbons (HFC), hydrofluoroolefins (HFO), ethers, alcohols, siloxanes, and inorganics (e.g. water). Despite extensive research on working fluids and their effects on cycle performance, no one fluid is optimal in all cases. This is mainly due to differences between applications, heat source conditions, initial fluid selection, the applied boundary conditions and system limitations, and the chosen selection criteria (e.g. packaging or environmental impact). The most relevant properties of working fluids are discussed below, followed by an explanation of the different methods for fluid selection. While the possibility of using mixtures is an important consideration for fluid selection, mixtures are considered outside the scope of this thesis and are therefore not discussed further.

2.4.1 Fluid Properties

Thermophysical properties

The thermodynamic performance of a working fluid is depends on several interdependent thermodynamic properties such as its critical point, latent and specific heat, density, and boiling temperature. The complexity of this interdependence makes it difficult to predict the best-performing working fluid for any given application, especially given that it varies with the conditions of the heat source.

The most effective heat transfer occurs when there is a good thermal match between the temperature profiles of the heat source and the cycle. To optimize the specific work extracted from the recovered heat, the pressure ratio over the expander can be increased by either increasing the evaporating pressure or reducing the condensing pressure in the system. Aside from the limitations relating to the fluid, the maximum pressure and temperature are limited by the choice of materials for the components. On the condensing side, having a pressure lower than the ambient pressure could cause air infiltration into the system. An important design constraint for expanders, especially turbines, is the vapor fraction after expansion; the amount of liquid in the vapor is often limited to prevent droplets from damaging the expander. The vapor fraction after expansion depends on the shape of the vapor saturation curve, which may be classified as wet, dry, or isentropic, as shown in Fig. 2.8. For wet fluids, superheating is often used to avoid wet conditions at the end of the expansion and to achieve higher power outputs. For isentropic fluids, superheating may increase the power output, although the effect is small. Conversely, for dry fluids, a high amount of superheating can even be detrimental [82, 84].

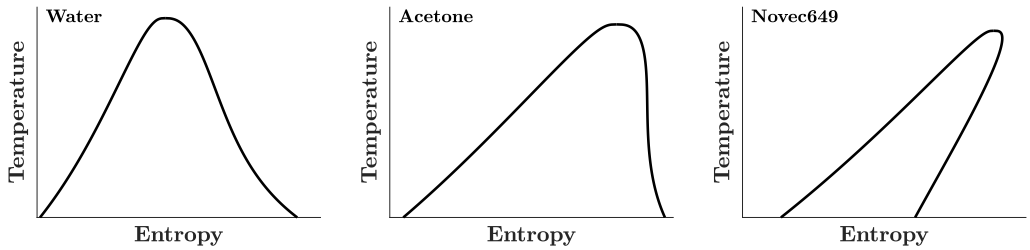

Fig. 2.8: Saturation curves for three types of fluids: wet (left), isentropic (middle), and dry (right).

The shape of the vapor saturation curve can be quantified using the definition for molecular complexity (σ) [85], as shown in equation 2.3: σ is positive for dry fluids, negative for wet fluids, and near zero for isentropic fluids [82, 85]. The higher the value of the molecular complexity (positive or negative), the steeper the slope of the vapor saturation curve.

$$\sigma = \frac{T_{\mathrm{cr}}}{R}\left(\frac{\partial s}{\partial T}\right)_{\mathrm{sv},T_{\mathrm{r}}=0.7} \tag{2.3}$$

Also important to consider are the transport properties of the fluids, such as their viscosity and thermal conductivity. These properties affect the heat transfer and pressure drop characteristics, which are especially important in heat exchanger design.

Thermal stability

At high temperatures, organic fluids may undergo chemical decomposition, which limits the maximum temperature of the cycle [78]. Although it is difficult to obtain thermal stability temperature data for many fluids, the maximum temperatures for several hydrocarbons, fluorocompounds, and refrigerants have been estimated to be above 300 °C [86, 87], although lower values of around 250 °C have also been reported [88]. While not a property of the working fluid, the degradation temperature of the lubricant oil may also be an important consideration if oil is mixed into the working fluid.

Component sizing, availability, and cost

The component size is especially important for automotive applications since there is limited space available. The volume flow rate has a direct effect on the sizing of the heat exchangers and expanders. Consequently, working fluids with high vapor densities are preferred [89], both at the expander inlet and outlet. Other important practical considerations are the availability and cost of the fluid. Techno-economic studies [78, 90] take into account all these aspects by finding optimal solutions that maximize net power output while minimizing system cost, weight and volume.

Material compatibility

For practical systems, it is necessary to carefully consider the working fluid's material compatibility in terms of factors such as its corrosiveness and compatibility with seals.

Environmental, safety, and health concerns

The environmental impact of a working fluid is evaluated based on its ozone depletion potential (ODP) and greenhouse warming potential (GWP). Under the Montreal Protocol, CFCs have been phased out over the last few years and HCFCs will be phased out between 2020 and 2030 because of their high ODP values [84]. In the EU, fluorinated greenhouse gases with GWPs above 150 are banned from use in air-conditioning systems for passenger cars and light-duty vehicles, and the European Commission is considering extending this ban to other vehicle classes including heavy duty vehicles [91]. Separately from the environmental impact, the flammability of the fluid has important implications for its safety in practical automotive applications. Properties detrimental to health such as toxicity and carcinogenicity must also be carefully considered when selecting a working fluid. Lion et al. [16] suggest that working fluid selection should be guided by the NFPA 704 Standard, which categorizes working fluids based on their health, flammability, and chemical instability-reactivity hazards.

2.4.2 Fluid Selection

The considerations mentioned above mean that in addition to offering good thermodynamic performance, the ideal fluid should be non-toxic, non-flammable, non-corrosive, thermally stable, cost-effective, and have low or zero GWP and ODP values [13]. Since no such fluid currently exists, compromises must be made when selecting a working fluid while ensuring the chosen properties of the fluid are suitable for the intended application. Methods for fluid selection can be conceptually divided into two groups:

Screening approach

In the screening approach, existing working fluids are identified from databases such as CoolProp [92] or REFPROP [93] and evaluated by performing cycle simulations using the given heat source conditions. This approach is the one most commonly used for fluid selection and also the one used in this thesis. A major effort was made by Preißinger et al. [94] who screened over 72 million chemical structures. They evaluated the performance of the fluids in two different ORC configurations and three different cooling concepts to generate a multi-criterion ranking for waste heat recovery in passenger cars and heavy-duty trucks. Their overall results revealed that there is a trade-off between optimal thermodynamic performance and safety issues: fluids with high net power output and low ODP are often highly flammable, while well-performing non-flammable working fluids often have environmental and toxicological drawbacks.

Molecular design approach

More recently, two alternative approaches were formulated for designing an optimal working fluid rather than selecting an existing one based on the properties contained in a database. The continuous molecular targeting (CoMT) approach uses a molecule-based thermodynamic model in which the parameters representing a molecule are treated as continuous. These parameters are optimized together with other process parameters, leading to an ideal hypothetical target molecule and a corresponding optimized process [95]. The parameters of the hypothetical molecule are subsequently compared to those of real fluids to find the closest existing alternative. In general, the hypothetical fluid will not perfectly match any real fluid, so it is usually impossible to find a fluid with optimal properties. However, the results of the CoMT optimization provide an upper bound on the performance of the process [96]. By contrast, computer-aided molecular design methods (CAMD) use a database containing a few chemical groups that are used to generate and search a vast number of conventional or novel molecular structures to identify the molecules offering the best performance [97].

Schilling et al. [98] used a combined CoMT-CAMD approach for the integrated design of ORCs and working fluids for optimal exhaust heat recovery in a heavy-duty vehicle during transient operation. An important finding was that considering a single operating point was insufficient to capture all aspects of transient behavior and led to suboptimal selection of working fluids.

3 Experimental Setups

Although there have been many studies on the use of ORCs for waste heat recovery, published experimental results concerning heavy-duty Diesel engines are relatively scarce. In most experimental studies investigating high-temperature heat sources, the exhaust gases are used as the main heat source, but some studies have also considered the EGR [26, 40, 99]. Turbine [77], piston [40], vane [100], scroll [101], and screw [102] expanders have been investigated in combination with water [103], refrigerants [101, 102, 104], ethanol [26], CO_2 [66], HFE [99], MM [100], or Novec649 [105] as the working fluid.

Experimental studies on the potential of the engine coolant as a heat source for waste heat recovery using an ORC are even fewer. Furukawa et al. [99] extracted the heat from a combination of the engine coolant, EGR, and exhaust gases of a heavy-duty engine using a turbine expander and HFE as the working fluid. For a light-duty engine, Smague et al. [106] studied the performance of an ORC for WHR from the coolant with a turbine expander and Novec649 as the working fluid using simulations and experiments.

The research presented in this thesis used two different experimental setups, both consisting of a heavy-duty Diesel engine connected to an organic Rankine cycle for waste heat recovery. This chapter first presents the specifications of the two 13 L heavy-duty Diesel engines that were used as heat sources and then describes the experimental setups used to investigate high- and low-temperature waste heat recovery. The results of these experiments are not presented in this chapter; these are given in Publications D, E, and G.

3.1 Heavy-Duty Diesel Engines

Two different heavy-duty Diesel engines were used, one for high-temperature waste heat recovery and one for low-temperature waste heat recovery. Basically, the engine used for LT-WHR (D13K540) is a more modern version of the engine used for HT-WHR (D13US) with a higher power output. The specifications of both engines are shown in Table 3.1.

Table 3.1: Specifications of the heavy-duty Diesel engines.

	Volvo D13 US	**Volvo D13K540**
Configuration	4 Stroke 6 Cylinder inline	4 Stroke 6 Cylinder inline
Aspiration	Turbocharged	Turbocharged
EGR	Long-route	Short-route
Peak power	373 kW (500 hp)	397 kW (540 hp)
Peak torque	2373 Nm	2600 Nm
Compression ratio	16.0:1	17.0:1
Bore x Stroke	131 x 158 mm	131 x 158 mm
Displacement	12.8 L	12.8 L
WHR setup	High-temperature	Low-temperature

Engine measurements were obtained using a NI compactRIO chassis with dedicated modules for temperature, analog, and digital signals. This was coupled to a LabVIEW interface [107] with which measurements were collected every 100 milliseconds and written to disk every second. The engine speed was set using a Schenck D900-1e water brake with its own control unit. The engine torque was controlled with a standard truck gas pedal that was mounted in the adjoining control room. Fuel flow was measured with an AVL 730 fuel balance and the engine coolant flow with a Rosemount 8800A vortex flow meter. The engine exhaust flow was measured using the pressure drop over a calibrated venturi tube with a Yokogawa differential pressure sensor. Pressure signals were obtained from WIKA A-10 analog pressure transmitters and the temperature signals using RS Pro Type K thermocouples. A summary of the measurement devices with the corresponding ranges and accuracies is shown in Table 3.2.

Table 3.2: Engine measurement devices and their accuracy.

Input	**Type**	**Range**	**Accuracy**	**Unit**
Engine speed	Schenck D900-1e	0 – 6500	± 2	rpm
Engine torque	Schenck D900-1e	-4000 – 4000	± 8	Nm
Fuel flow	AVL 730	0 – 150	± 0.9	kg/h
Exhaust flow	Yokogawa EJA110E	0 – 5000	± 2.75	Pa
Exhaust pressure	WIKA A-10	0 – 2.5	± 0.03	bar(g)
Coolant flow	Rosemount 8800A	0 – 10	± 0.07	L/s
Coolant pressure	WIKA A-10	0 – 4	± 0.02	bar(g)
Temperature	RS Pro Type K	-75 – 1100	± 1.5	°C

3.2 Engine Exhaust Waste Heat Recovery

The high-temperature experimental results were obtained with the Volvo D13 US engine from which the exhaust gases were used to evaporate water in a waste heat recovery setup. The engine and HT-WHR setup are shown in Fig. 3.1 and a schematic overview of the setup is shown in Fig. 3.2, which also shows the locations of the sensors. In the same way as for the engine measurements, measurements of the WHR system components were obtained using a NI compactRIO chassis coupled to a LabVIEW interface [107], sampling every 100 milliseconds and writing to disk every second. The expander speed and torque were obtained using the HBM T40B universal torque transducer. The mass flow was measured directly with the Micro Motion F025S coriolis meter. Pressure readings were obtained with WIKA A-10 pressure transmitters and temperatures with RS Pro Type K thermocouples. The accuracies of these devices are shown in Table 3.3.

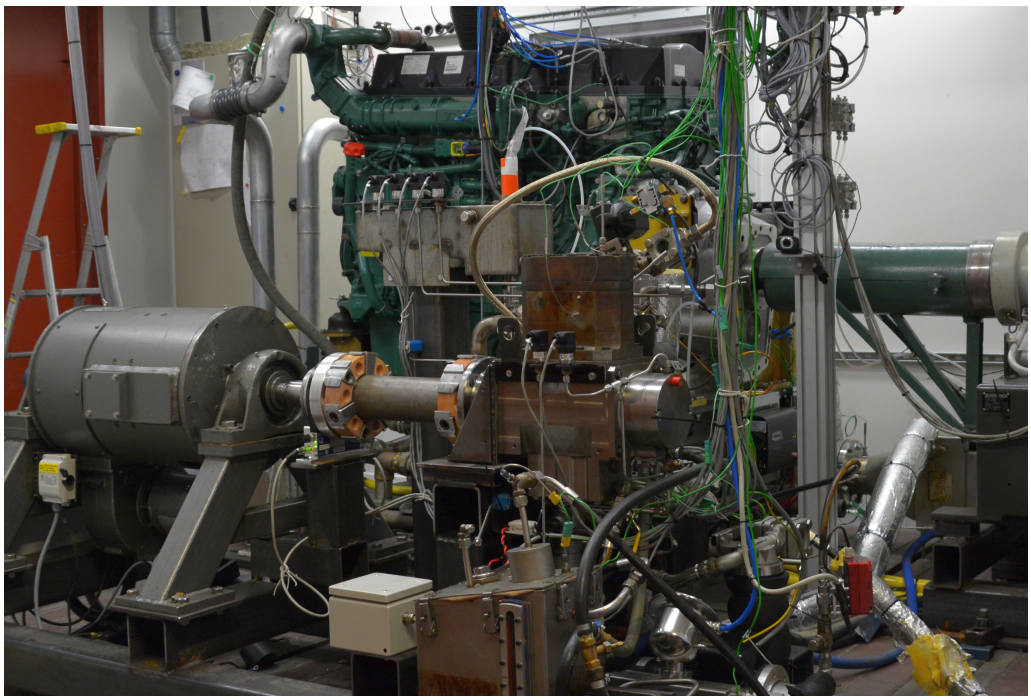

Fig. 3.1: Experimental setup for the exhaust waste heat recovery.

The specifications of the main WHR components are listed in Table 3.4. The HT-WHR system used demineralized water as the working fluid, which was placed in a reservoir open to the atmosphere. Water from the reservoir was pressurized by the pump; some of the pressurized water flowed into the evaporator and some returned to the reservoir via the controllable pump bypass valve (BPV). The pump bypass valve was used because even at the minimum pump speed the flow was too large to achieve superheating at

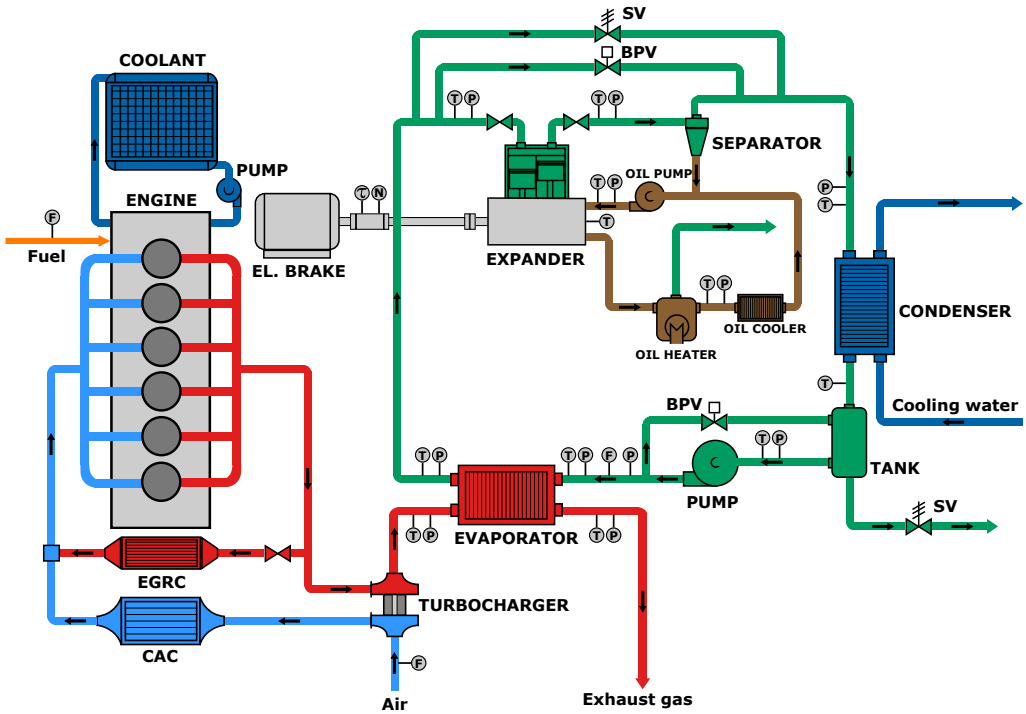

Fig. 3.2: Schematic of the exhaust waste heat recovery experimental setup.

the evaporator outlet under certain engine operating conditions. Although the pump is relatively insensitive to changes in system pressure, the use of the pump bypass valve meant that changes in the pressure considerably affected the flow through the evaporator, making it more difficult to control flow in the system. From the pump, the fluid entered the evaporator, which was developed specifically for this project. In the evaporator, the fluid was preheated, evaporated, and superheated using the exhaust gases from the engine. If the superheated conditions were not met (e.g. during start-up), the expander inlet and outlet valves were closed and the fluid flowed through the controllable expander bypass valve (BPV). When the steam was sufficiently superheated, the expander bypass valve

Table 3.3: Measurement devices accuracy.

Input	Type	Range	Accuracy	Unit
Expander speed	HBM T40B	0 – 20000	± 10	rpm
Expander torque	HBM T40B	-500 – 500	± 0.25	Nm
Mass flow	Micro Motion F025S	0 – 100	± 0.2	g/s
Cycle high pressure	WIKA A-10	0 – 60	± 0.6	bar(g)
Cycle low pressure	WIKA A-10	0 – 6	± 0.06	bar(g)
Temperature	RS Pro Type K	-75 – 1100	± 1.5	°C

was closed and steam entered the expander. The expander speed was controlled by the electric motor, which was connected to a variable frequency drive (VFD). The system pressure and the evaporator flow were determined by the engine operating conditions (i.e. heat input), pump speed, pump bypass valve position, and expander speed. During the experiments the mass flow was kept constant by varying the pump speed and pump bypass valve position to ensure superheated conditions at each engine operating point. The expander speed was varied, leading to changes in the system pressure, expander torque, and expander power. The expander was a reciprocating piston expander with a crankcase that requires its own oil circuit, where the oil was circulated by an oil pump. Due to (significant) steam leakage from the system in the crankcase, a separate oil heater was installed. The oil was heated to 140 °C to ensure that any water in the oil was evaporated and expelled to the environment. Because the oil pump could not tolerate such high temperatures, the oil was cooled before entering the oil pump again. On the cycle side, the oil was separated from the water prior to entering the condenser. In the condenser, the two-phase mixture was condensed and subcooled using the process water available in the test cell. From the condenser, the subcooled water entered the reservoir. Pressure relief valves were installed both on the high and low pressure side.

Table 3.4: HT component specifications.

Pump	
Brand	Danfoss PAH2
Type	Axial piston
Displacement	2 cm^3
Speed	1000 – 3000 rpm
Max. pressure	100 bar
Max. volume flow	360 L/min
Electric motor	Hoyer HMA2 90L-4
	230 V, 3-phase, 1.5 kW
Controller (VFD)	IMO iDrive EDX-220-21-E
Pump bypass valve	
Brand	Swagelok SS-1RS4
Type	Integral-bonnet needle
Controller	Hanbay MCL-000AF
Evaporator	
Brand	TitanX
Type	Plate, cross-counter flow
Max. pressure	35 bar
Max. temperature	350 °C
Max. heat load	n/a
Expander	
Brand	Voith
Type	Reciprocating piston
	2-cylinder
Displacement	0.8 L
Speed	600 – 3500 rpm
Electric motor	David McClure LTD
	400 V, 3-phase, 37 kW
Controller (VFD)	Parker DC590+ Integrator 2
Expander bypass valve	
Brand	Swagelok SS-18RS8
Type	Integral-bonnet needle
Controller	Hanbay MCL-000AF
Condenser	
Brand	Modine
Type	Plate, counter-current flow
Max. pressure	n/a
Max. temperature	n/a
Max. heat load	n/a

3.3 Engine Coolant Waste Heat Recovery

For the low-temperature experiments, the Volvo D13K540 engine was used with the engine coolant as the heat source for an organic Rankine cycle with R1233zd(E) as the working fluid. This engine and the LT-WHR setup are shown in Fig. 3.3 and a schematic overview is presented in Fig. 3.4, which also shows the locations of the sensors. In a similar manner to the experiments obtained with the engine and HT-WHR setup, measurements were performed using a NI compactRIO chassis coupled to a LabVIEW interface [107], sampling every 100 milliseconds and writing to disk every second. The expander speed and torque signals were measured with a HBM T22 torque transducer. The mass flow was measured directly with the Micro Motion F025S coriolis meter. Pressure readings were obtained with WIKA A-10 pressure transmitters and temperatures with RS Pro Type K thermocouples. The accuracies of these devices are shown in Table 3.5.

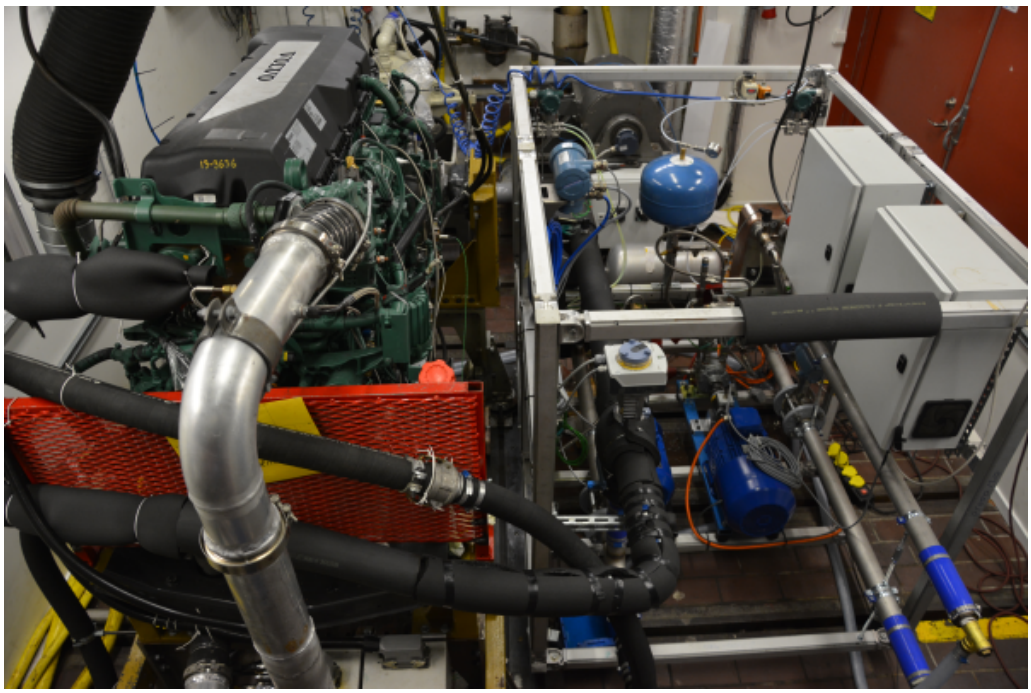

Fig. 3.3: Experimental setup for the coolant waste heat recovery.

Detailed specifications of the main components of the LT-WHR system are listed in Table 3.6 and 3.7. Although the LT-WHR setup shared many similarities with the HT-WHR setup, it used a different heat source and working fluid. In the LT-WHR setup, the engine coolant was used to preheat, evaporate and superheat the working fluid R1233zd(E). A coolant bypass valve was installed, which was only used during start-up to allow faster engine warm up. A plate heat exchanger cooled by the process water from the

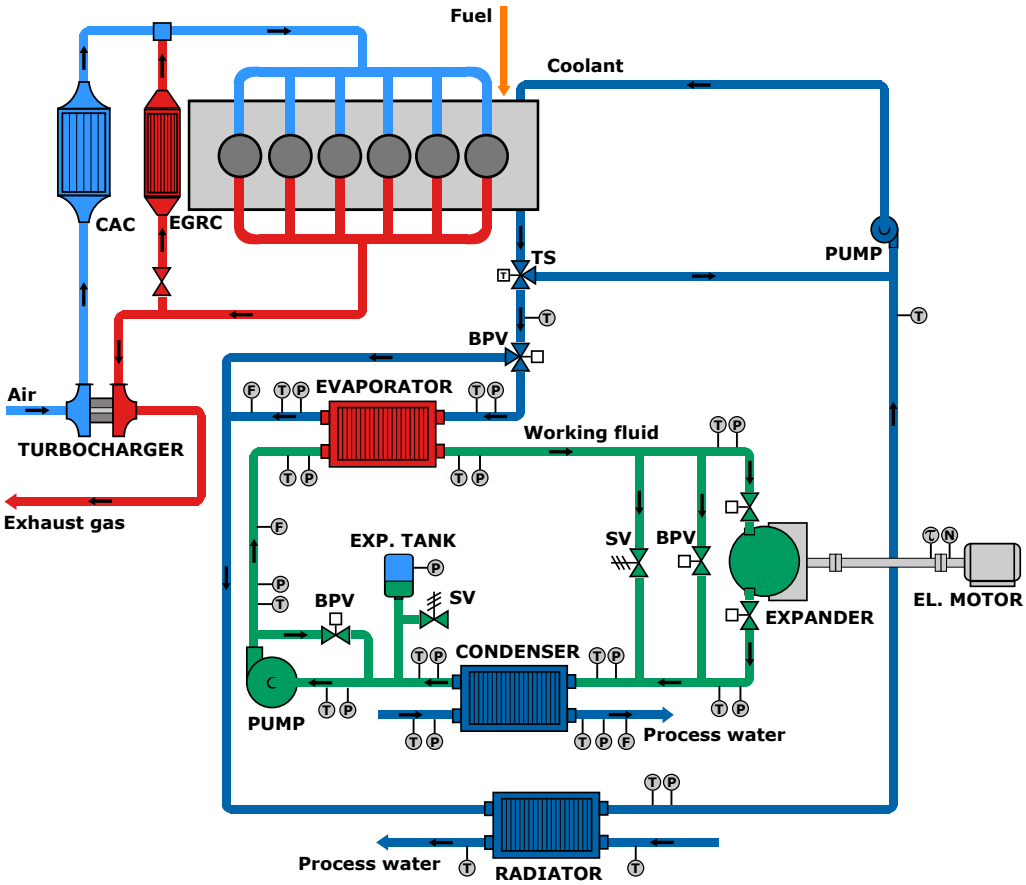

Fig. 3.4: Schematic of the coolant waste heat recovery experimental setup.

test cell functioned as the radiator. Another difference from the HT-WHR setup is the way pressure was regulated on the low pressure side. To regulate the condensing pressure (and thus the condensing temperature), an expansion tank was installed upstream of the pump. The expansion tank contained a membrane with air on one side and the working fluid on the other side so that the condensing pressure in the cycle could be regulated by adjusting the air pressure. From the expansion tank, the working fluid entered the pump where it was compressed before entering the evaporator. Although a pump bypass valve (BPV) was installed, it was always closed during the experimental campaigns. Solenoid valves were installed upstream and downstream of the expander to prevent the fluid from entering the expander if the superheating conditions were not met. In that case, the fluid flowed through the controllable expander bypass valve (BPV). When sufficiently superheated, the expander BPV closed and the expander inlet and outlet valves opened, while the expander speed was set by using the connected electric motor as a brake. Since the pump was insensitive to changes in pressure, the mass flow was controlled by the

Table 3.5: Low-temperature WHR measurement devices accuracy.

Input	Type	Range	Accuracy	Unit
Expander speed	HBM T22	0 – 3000	± 15	rpm
Expander torque	HBM T22	-100 – 100	± 0.5	Nm
Cycle flow	Micro Motion F025S	0 – 600	± 3.0	g/s
Cycle high pressure	WIKA A-10	0 – 10	± 0.05	bar(g)
Cycle low pressure	WIKA A-10	0 – 6	± 0.03	bar(g)
Air pressure	WIKA A-10	0 – 9	± 0.05	bar(g)
Temperature	RS Pro Type K	-75 – 1100	± 1.5	°C

pump speed and the evaporating pressure by the expander speed. The expander power was determined by the expander speed and corresponding torque, and depended on the engine operating point. The working fluid left the expander as low-pressure vapor and entered the condenser, where it was condensed and subcooled by the process water from the test cell. Since there was no temperature or flow control for the condenser, the pump inlet temperature of the working fluid was determined by the process water temperature.

Table 3.6: LT component specifications.

Pump	
Brand	Wanner-Hydracell G10
Type	Seal-less diaphragm pump
Displacement	0.023 L
Speed	100 – 1450 rpm
Max. pressure	69 bar
Max. volume flow	33.4 L/min
Electric motor	BEVI IE3 90-4-150
	250 V, 1450 rpm, 1.5 kW
Controller (VFD)	IMO iDrive EDX-220-21-E
Pump bypass valve	
Brand	Swagelok SS-18RS12MM
Type	Integral-bonnet needle
Controller	Hanbay MCL-000AF
Evaporator	
Brand	SWEP B250ASHx100
Type	Plate, counter-current
Max. pressure	46 bar
Max. temperature	n/a
Max. heat load	125 kW

Table 3.7: LT component specifications (continued).

Expander	
Brand	GAST 6AM-FRV-5A
Type	Sliding vane, 4 vanes
Displacement	0.152 L
Speed	200 – 3000 rpm
Electric motor	BEVI IE3 3SIE 112-M2
	400 V, 2920 rpm, 4.8 kW
Controller (VFD)	Delta C2000
Expander bypass valve	
Brand	Swagelok SS-18RS18MM
Type	Integral-bonnet needle
Controller	Hanbay MCL-000AF
Condenser	
Brand	SWEP B250ASHx60
Type	Plate, counter-current
Max. pressure	46 bar
Max. temperature	n/a
Max. heat load	116 kW
Coolant bypass valve	
Brand	Siemens VXG41
Type	3-Port seat valve
Controller	Siemens SAX61
Expansion tank	
Brand	Armatec AT 8321E12
Type	Diaphragm
Volume	12 L
Max. pressure	10 bar
Pressure regulator	SMC ITV1050
High-pressure safety valve	
Brand	Swagelok SS-R4S12MM
Type	Proportional relief valve
Low-pressure safety valve	
Brand	Swagelok SS-RL4S12MM
Type	Propertional relief valve
In-line filters	
Brand	Danfoss 148B5243
Type	Strainer

4 Modeling

Modeling of thermodynamic cycles for waste heat recovery and their components is important because it can help to explain the underlying physical phenomena, is less time-consuming and costly than experiments, and enables investigation of advanced topics such as thermo-economic optimization [108] or elaborate control strategies [90].

The pump flow is usually taken as a function of the pump's displacement and rotational speed [109], sometimes combined with a volumetric efficiency [110]. The required power is typically determined based on an estimated pump efficiency, typically between 65 and 85 % [75] even though much lower efficiencies have been observed in experiments [77]. Efficiency values can be derived from experiments [77], taken from manufacturer data, calibrated using steady-state performance maps [110], or calculated using affinity laws [111].

Heat exchangers are most commonly modeled using either moving boundary models or discretized models [112]. In a moving boundary model, the fluid flow in the heat exchanger is divided into as many control volumes as there are states (e.g., liquid, two-phase, vapor) in the fluid flow. The sizes of the control volumes vary, following the saturated liquid and vapor boundaries. In contrast, the finite volume approach involves discretizing the heat exchanger into a number of equal and constant control volumes [113].

The expander efficiency is often taken to be a fixed value between 10 and 85% [114, 115]. For more detailed modeling, three levels of expander models can be distinguished: empirical, semi-empirical, and deterministic [116]. Empirical models are based on expressions involving selected variables that are fitted on experimental data to obtain a generic performance estimate [117]. Semi-empirical models are based on a set of equations representing the physical processes occuring in the expander. Originally introduced by Lemort [118], such models have been widely adopted because of their adaptability to different types of expanders [119]. Deterministic models are based on comprehensive descriptions derived from the equations for conservation of mass and energy [116]. Examples include a mathematical model of a vane expander using its real geometry [120] and a detailed CFD model for shape optimization of an axial turbine [121].

In this thesis, modeling was used to predict the performance of the different thermodynamic cycles and cycle components, and to complement the experimental results. Two modeling approaches were used: 0D modeling and 1D modeling. The 0D models were used to evaluate the thermodynamic performance of the cycles under fixed boundary conditions. The equations for these models are presented in Section 4.1. The more detailed 1D models require calibration and validation against experimental data but can provide deeper insight into the performance of individual components. The equations for these models are presented in Section 4.2. The inputs for the simulations and the corresponding results are not discussed in this chapter but are presented in Publications A, B, C, D, E, and G.

4.1 0D-Modeling

4.1.1 Cycles

The thermodynamic cycle models were built using the Modelica [122] programming language and modeled by connecting individual components through nodes. Each node contains the thermodynamic state, which includes all of the thermodynamic properties of the working fluid and is defined by two independent properties (mostly pressure and enthalpy). Mathematical descriptions of each cycle and component are given below. All of the components were modeled using the following assumptions:

- The system is in a steady state
- There are no pressure losses in the system, including the heat exchangers and piping
- There are no heat losses to the environment
- Changes in kinetic and potential energy can be neglected
- Expansion in the throttling valves is isenthalpic
- There is perfect mixing and separation of the working fluids
- The isentropic efficiencies of the pump and expander are constant

The following section presents the modeling relations of each individual component in the thermodynamic cycles. The heat transferred from the source to the cycle depends on the source outlet temperature, which is either a fixed value or dependent on the pinch point. If the heat input into the cycle and the cycle pressure are known, one extra condition is needed to close the system of equations. The necessary equation depends on the type of cycle under consideration, as shown below. For reference, schematic depictions of the circuits and the corresponding Ts-diagrams for each cycle can be found in Section 2.2.

Organic Rankine Cycle

The system of equations for the ORC can be closed using four conditions. First, a saturated vapor condition can be imposed at the evaporator outlet or condenser inlet by defining the enthalpy ($h_{\text{evap,out}}$ or $h_{\text{cond,in}}$) as the saturated vapor enthalpy ($h_{\text{sat,vap}}$) at the corresponding pressure ($p_{\text{evap,out}}$ or $p_{\text{cond,in}}$). Alternatively, the superheating temperature ($T_{\text{evap,out}}$ or $T_{\text{cond,in}}$) at the corresponding saturation temperature (T_{sat}) can be set by specifying a degree of superheating (ΔT_{sup}). These four conditions can be expressed using the following four equations, of which only one can be defined:

$$\begin{cases} h_{\text{evap,out}} = h_{\text{sat,vap}}@\ p_{\text{evap,out}} & \text{Saturated vapor at evaporator outlet} \\ h_{\text{cond,in}} = h_{\text{sat,vap}}@\ p_{\text{cond,in}} & \text{Saturated vapor at condenser inlet} \\ T_{\text{evap,out}} = T_{\text{sat,evap}} + \Delta T_{\text{sup,evap}} & \text{Superheated temperature at evaporator outlet} \\ T_{\text{cond,in}} = T_{\text{sat,cond}} + \Delta T_{\text{sup,cond}} & \text{Superheated temperature at condenser inlet} \end{cases}$$

Transcritical Rankine Cycle

Since no evaporation occurs in the TRC, it is not possible to set conditions at the evaporator outlet. Therefore, either the enthalpy at the condenser inlet ($h_{\text{cond,in}}$) is set as the saturated vapor enthalpy ($h_{\text{sat,vap}}$) at the condenser pressure ($p_{\text{cond,in}}$) or the superheated temperature at the condenser inlet ($T_{\text{cond,in}}$) is set by adding a specified degree of superheating (ΔT_{sup}) to the saturation temperature at the condenser pressure ($T_{\text{sat,cond}}$). These conditions can be expressed mathematically using the following equations:

$$\begin{cases} h_{\text{cond,in}} = h_{\text{sat,vap}}@\ p_{\text{cond,in}} & \text{Saturated vapor at condenser inlet} \\ T_{\text{cond,in}} = T_{\text{sat,cond}} + \Delta T_{\text{sup,cond}} & \text{Superheated temperature at condenser inlet} \end{cases}$$

Trilateral Flash Cycle

For the TFC, there is only one condition at the evaporator outlet: saturated liquid at the outlet of the evaporator. Therefore, the enthalpy at the evaporator outlet ($h_{\text{evap,out}}$) is set to the saturated liquid enthalpy ($h_{\text{sat,liq}}$) at the evaporator pressure ($p_{\text{evap,out}}$). This condition is expressed mathematically below.

$$h_{\text{evap,out}} = h_{\text{sat,liq}}@\ p_{\text{evap,out}} \quad \text{Saturated liquid at evaporator outlet}$$

Organic Flash Cycle

As in the TFC, the enthalpy at the evaporator outlet ($h_{\text{evap,out}}$) in the OFC is set to the saturated liquid enthalpy ($h_{\text{sat,liq}}$) at the evaporator pressure ($p_{\text{evap,out}}$). An additional equation is needed to calculate the intermediate pressure at the flash vessel inlet ($p_{\text{fv,in}}$) using a fixed value for the pressure ratio (r_{p}).

$$\begin{aligned} h_{\text{evap,out}} &= h_{\text{sat,liq}}@\ p_{\text{evap,out}} && \text{Saturated liquid at evaporator outlet} \\ p_{\text{fv,in}} &= p_{\text{pmp,in}} + \frac{p_{\text{evap,out}} - p_{\text{pmp,in}}}{r_{\text{p}}} && \text{Intermediate pressure} \end{aligned}$$

4.1.2 Components

Each component is connected to other components through nodes that contain the thermodynamic state of the working fluid. The components are also defined by a number of fixed conditions that are set of the start of the simulations and do not change, and by a set of equations that are solved simultaneously for all components. The fixed conditions and equations for all cycle components are specified below.

4.1.2.1 Pump

Since the condensation temperature is set by either the minimum pressure or a temperature constraint, the pressure at the pump inlet ($p_{\mathrm{pmp,in}}$) is known. The working fluid is assumed to be saturated liquid at the inlet of the pump ($x_{\mathrm{pmp,in}} = 0$) and the isentropic efficiency of the pump ($\eta_{\mathrm{is,pmp}}$) is set to a fixed value. The pump outlet pressure ($p_{\mathrm{pmp,out}}$) is equal to the evaporating pressure, which is either set or calculated. Knowing this pressure, the isentropic ($h_{\mathrm{is,pmp}}$) and actual enthalpy ($h_{\mathrm{pmp,out}}$) at the pump outlet can be calculated and the power required by the pump ($\dot{W}_{\mathrm{pmp}}$) can be determined.

Fixed conditions:

$$p_{\mathrm{pmp,in}},\ x_{\mathrm{pmp,in}},\ \eta_{\mathrm{is,pmp}}$$

Equations:

$$h_{\mathrm{is,pmp}} = h(p_{\mathrm{pmp,out}},\ s_{\mathrm{pmp,in}}) \tag{4.1}$$

$$h_{\mathrm{pmp,out}} = h_{\mathrm{pmp,in}} + \frac{h_{\mathrm{is,pmp}} - h_{\mathrm{pmp,in}}}{\eta_{\mathrm{is,pmp}}} \tag{4.2}$$

$$\dot{W}_{\mathrm{pmp}} = \dot{m}_{\mathrm{c}}(h_{\mathrm{pmp,out}} - h_{\mathrm{pmp,in}}) \tag{4.3}$$

4.1.2.2 Heat Exchangers

In the cycle simulations, two different types of heat exchangers are used: an evaporator/heater and a condenser. This section only describes the evaporator/heater but presents equations for both types of heat exchanger.

In the evaporator, the inlet conditions for the heat source are known ($\dot{m}_{\mathrm{so}},\ p_{\mathrm{so,in}},\ T_{\mathrm{so,in}}$). Therefore, assuming that there is no pressure loss, the source outlet pressure ($p_{\mathrm{so,out}}$) is also known. The minimum required temperature difference at the pinch point ($\Delta T_{\mathrm{pp,so}}$) is set as a constraint; the location of the pinch point depends on where the limiting temperature difference occurs. The total heat transfer from the source is equal to the sum of the heat transfer from the source inlet to the pinch point location and from the pinch point to the source outlet. It is assumed that no external heat losses occur, so the heat transfer from the source is equal to the heat input into the cycle.

Evaporator/Heater

Fixed conditions:

$$\dot{m}_{\mathrm{so}},\ p_{\mathrm{so,in}},\ p_{\mathrm{so,out}},\ T_{\mathrm{so,in}},\ \Delta T_{\mathrm{pp,so}}$$

Equations:

$$\dot{Q}_{\mathrm{pp,so,in}} = \dot{m}_{\mathrm{so}}(h_{\mathrm{so,in}} - h_{\mathrm{pp,so}}) \tag{4.4}$$

$$\dot{Q}_{\mathrm{pp,so,out}} = \dot{m}_{\mathrm{so}}(h_{\mathrm{pp,so}} - h_{\mathrm{so,out}}) \tag{4.5}$$

$$\dot{Q}_{\mathrm{so}} = \dot{Q}_{\mathrm{so,pp,in}} + \dot{Q}_{\mathrm{so,pp,out}} \tag{4.6}$$

$$\dot{Q}_{\mathrm{evap}} = \dot{Q}_{\mathrm{so}} \tag{4.7}$$

$$\dot{Q}_{\mathrm{pp,evap,in}} = \dot{Q}_{\mathrm{so,pp,out}} \tag{4.8}$$

$$\dot{Q}_{\mathrm{evap}} = \dot{m}_{\mathrm{c}}(h_{\mathrm{evap,out}} - h_{\mathrm{evap,in}}) \tag{4.9}$$

$$\dot{Q}_{\mathrm{pp,evap,in}} = \dot{m}_{\mathrm{c}}(h_{\mathrm{pp,evap}} - h_{\mathrm{evap,in}}) \tag{4.10}$$

Condenser

Fixed conditions:

$$\dot{m}_{\mathrm{si}},\ p_{\mathrm{si,in}},\ p_{\mathrm{si,out}},\ T_{\mathrm{si,in}},\ \Delta T_{\mathrm{pp,si}},\ p_{\mathrm{cond,in}},\ p_{\mathrm{cond,out}},\ x_{\mathrm{cond,out}}$$

Equations:

$$\dot{Q}_{\mathrm{pp,si,in}} = \dot{m}_{\mathrm{si}}(h_{\mathrm{pp,si}} - h_{\mathrm{si,in}}) \tag{4.11}$$

$$\dot{Q}_{\mathrm{pp,si,out}} = \dot{m}_{\mathrm{si}}(h_{\mathrm{si,out}} - h_{\mathrm{pp,si}}) \tag{4.12}$$

$$\dot{Q}_{\mathrm{si}} = \dot{Q}_{\mathrm{si,pp,in}} + \dot{Q}_{\mathrm{si,pp,out}} \tag{4.13}$$

$$\dot{Q}_{\mathrm{cond}} = \dot{Q}_{\mathrm{si}} \tag{4.14}$$

$$\dot{Q}_{\mathrm{pp,cond,in}} = \dot{Q}_{\mathrm{si,pp,out}} \tag{4.15}$$

$$\dot{Q}_{\mathrm{cond}} = \dot{m}_{\mathrm{c}}(h_{\mathrm{cond,in}} - h_{\mathrm{cond,out}}) \tag{4.16}$$

$$\dot{Q}_{\mathrm{pp,cond,in}} = \dot{m}_{\mathrm{c}}(h_{\mathrm{cond,in}} - h_{\mathrm{pp,cond}}) \tag{4.17}$$

4.1.2.3 Expander

The isentropic efficiency of the expander ($\eta_{\text{is,exp}}$) is set to a constant value, and the expander outlet pressure ($p_{\text{exp,out}}$) is equal to the condensation pressure, which is known. Consequently, the isentropic ($h_{\text{is,exp}}$) and actual enthalpy ($h_{\text{exp,out}}$) at the expander outlet can be calculated, allowing the power produced by the expander ($\dot{W}_{\text{exp}}$) to be determined.

Fixed conditions:

$$p_{\text{exp,out}},\ \eta_{\text{is,exp}}$$

Equations:

$$h_{\text{is,exp}} = h(p_{\text{exp,out}},\ s_{\text{exp,in}}) \tag{4.18}$$

$$h_{\text{exp,out}} = h_{\text{exp,in}} - \eta_{\text{is,exp}}(h_{\text{exp,in}} - h_{\text{is,exp}}) \tag{4.19}$$

$$\dot{W}_{\text{exp}} = \dot{m}_{\text{c}}(h_{\text{exp,in}} - h_{\text{exp,out}}) \tag{4.20}$$

4.1.2.4 Flash Vessel

The intermediate pressure at the flash vessel inlet ($p_{\text{fv,in}}$) is calculated using a fixed value for the pressure ratio (r_{p}). Since it is assumed there are no pressure losses, the outlet pressure is equal to the inlet pressure ($p_{\text{fv,out}} = p_{\text{fv,in}}$). Knowing the vessel pressures and the cycle mass flow, the saturated liquid ($h_{\text{fv,out,liq}}$) and vapor ($h_{\text{fv,out,vap}}$) enthalpies can be calculated, as well as the mass flows exiting the vessel ($\dot{m}_{\text{fv,out,liq}}$ and $\dot{m}_{\text{fv,out,vap}}$).

Equations:

$$p_{\text{fv,in}} = p_{\text{pmp,in}} + \frac{p_{\text{evap,out}} - p_{\text{pmp,in}}}{r_{\text{p}}} \tag{4.21}$$

$$h_{\text{fv,out,liq}} = h_{\text{sat,liq}}@\ p_{\text{fv,out}} \tag{4.22}$$

$$h_{\text{fv,out,vap}} = h_{\text{sat,vap}}@\ p_{\text{fv,out}} \tag{4.23}$$

$$\dot{m}_{\text{fv,out,liq}} = (1 - x_{\text{fv,in}})\dot{m}_{\text{c}} \tag{4.24}$$

$$\dot{m}_{\text{fv,out,vap}} = x_{\text{fv,in}}\dot{m}_{\text{c}} \tag{4.25}$$

4.1.2.5 Throttling Valve

The throttling valve is assumed to be isenthalpic, so once the pressures in the system are known or calculated, the thermodynamic properties at the outlet are known.

Equations:

$$h_{\mathrm{tv,out}} = h_{\mathrm{tv,in}} \tag{4.26}$$

4.1.2.6 Mixer

Because the mixer operates at the condensing pressure and no pressure losses are assumed, the inlet and outlet pressures of the mixer ($p_{\mathrm{mxr,in}}$ and $p_{\mathrm{mxr,out}}$) are known. Since perfect mixing is assumed, the outlet mass ($\dot{m}_{\mathrm{mxr,out}}$) and energy flows are given by the sum of all the inlet quantities, as shown in Eq. (4.27) and (4.28).

Fixed conditions:

$$p_{\mathrm{mxr,in}},\ p_{\mathrm{mxr,out}}$$

Equations:

$$\dot{m}_{\mathrm{mxr,out}} = \sum_{i=1}^{n} \dot{m}_{\mathrm{mxr,i,in}} \tag{4.27}$$

$$(\dot{m}h)_{\mathrm{mxr,out}} = \sum_{i=1}^{n} (\dot{m}h)_{\mathrm{mxr,i,in}} \tag{4.28}$$

4.1.2.7 Cycle Performance

The performance of the cycle can be evaluated on the basis of the net shaft power ($\dot{W}_{\mathrm{net}}$), mechanical power ($\dot{W}_{\mathrm{mech}}$), electrical power ($\dot{W}_{\mathrm{el}}$), and the thermodynamic efficiency (η_{th}), which are defined in the equations below.

$$\dot{W}_{\mathrm{net}} = \dot{W}_{\mathrm{exp}} - \dot{W}_{\mathrm{pmp}} \tag{4.29}$$

$$\dot{W}_{\mathrm{mech}} = \dot{W}\eta_{\mathrm{mech}} \tag{4.30}$$

$$\dot{W}_{\mathrm{el}} = \dot{W}\eta_{\mathrm{el}} \tag{4.31}$$

$$\eta_{\mathrm{th}} = \frac{\dot{W}_{\mathrm{net}}}{\dot{Q}_{\mathrm{evap}}} \tag{4.32}$$

4.1.3 Modeling Approach

Simulations were performed using the solvers in Dymola [123], which was connected to the CoolProp database [92] to obtain data on the thermodynamic properties of the fluids. Pre- and post-processing of the simulation results was done with Python [124]. To evaluate the maximum power output within the given constraints, a golden section search was combined with a constraints checking framework, which is shown in Figure 4.1. The working fluid and evaporating pressure were the inputs for the simulations and the fixed cycle conditions (e.g., p_{con}, T_{cond}) were set before starting each simulation. The results of the simulation were evaluated with respect to the constraints (e.g. ΔT_{pp}, ΔT_{sup}). The chosen framework allowed for an automated checking of the constraints, thereby enabling evaluation of many working fluids and pressures for the different heat sources.

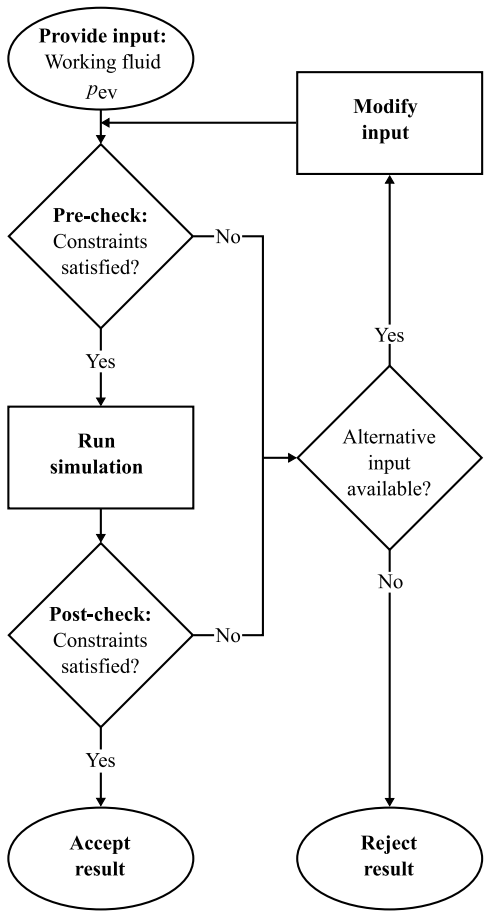

Fig. 4.1: Constraints checking framework

4.2 1D-Modeling

4.2.1 Cycle

Detailed models were only developed for the components of the (organic) Rankine cycle, although these component models could also be used in the the other thermodynamic cycles. This section presents the mathematical formulations of the component models, which were implemented in MATLAB [125] under the following assumptions:

- The system is in a steady state
- There are no pressure losses in the system, including the heat exchangers and piping
- Heat losses to the environment do not occur other than in the expander
- Changes in kinetic and potential energy can be neglected

The detailed models presented in this section are calibrated and/or validated against the experimental results. In addition to providing a more detailed understanding of the processes occurring within the ORC, these models can be used to predict how the cycle would perform outside the experimental range or with different working fluids. This section begins with the descriptions of the mathematical relations used to model the main components: the pump, the pump bypass valve, the evaporator, the expander, and the condenser. This is followed by a short description of the modeling approach, which explains how the cycle simulations were performed using the different component models.

4.2.2 Components

4.2.2.1 Pump

Pump performance is commonly modeled using affinity laws [111]. However, since pump data from the manufacturers was available, correlations based on this data were used instead, where the theoretical volume flow of the pump is adjusted for the pressure:

$$\dot{V}_{\mathrm{pmp}} = \dot{V}_{\mathrm{th}} - \dot{V}_{\mathrm{corr}} \frac{p_{\mathrm{pmp,out}}}{p_{\mathrm{max}}} \tag{4.33}$$

The theoretical flow ($\dot{V}_{\mathrm{th}}$) is defined as:

$$\dot{V}_{\mathrm{th}} = V_{\mathrm{pmp}} N_{\mathrm{pmp}} / 60 \tag{4.34}$$

With the relations for the volume flow known, the mass flow ($\dot{m}_{\mathrm{pmp}}$) can be determined:

$$\dot{m}_{\mathrm{pmp}} = \rho_{\mathrm{pmp,out}} \dot{V}_{\mathrm{pmp}} \tag{4.35}$$

The pump power can then be calculated using the pump efficiency (η_{pmp}):

$$\dot{W}_{\mathrm{pmp}} = \dot{m}_{\mathrm{pmp}}(h_{\mathrm{pmp,out}} - h_{\mathrm{pmp,in}})/\eta_{\mathrm{pmp}} \tag{4.36}$$

The efficiency of the pump can either be taken as a fixed value or be dependent on the pressure change over the pump.

4.2.2.2 Pump Bypass Valve

The pump bypass valve is modeled as an incompressible flow valve, as shown in Eq. (4.37). The discharge coefficient (C_{d}) and valve area (A) can be combined into an effective area (A_{bpv}) that depends on the position of the bypass valve and can be estimated using a series of linear functions based on experimental data.

$$\dot{m}_{\mathrm{bpv}} = C_{\mathrm{d}} A \sqrt{2\rho_{\mathrm{in}}(p_{\mathrm{in}} - p_{\mathrm{out}})} = A_{\mathrm{bpv}} \sqrt{2\rho_{\mathrm{in}}(p_{\mathrm{in}} - p_{\mathrm{out}})} \tag{4.37}$$

4.2.2.3 Evaporator

The evaporator that served as the basis for the modeling was specifically developed by TitanX for the experiments where the exhaust gases were used as the heat source. It is a cross-counter flow fin-type heat exchanger; a schematic depiction of its heat exchanger surface is presented in Fig. 4.2.

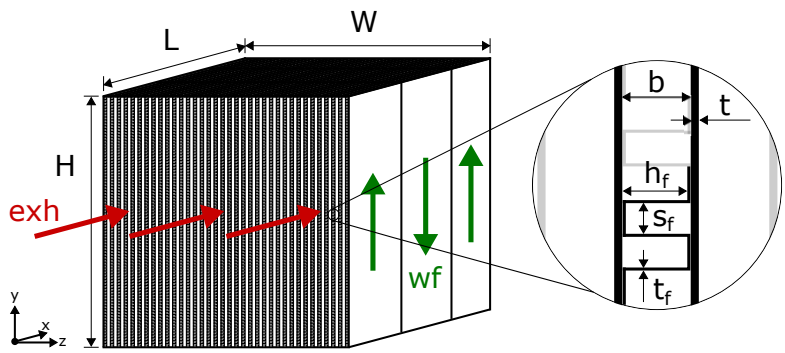

Fig. 4.2: Schematic illustration of the plates and fins of the exhaust evaporator.

Exhaust gases (exh) flow in the x-direction in a single pass, while the working fluid (wf) flows in the y-direction in three passes. The outer geometry of the heat exchanger is defined by its height (H), width (W), and length (L). The working fluid and exhaust gas are separated from each other by plates of thickness t with fins on both sides. These plates divide the heat exchanger into a number of channels (n_{ch}), where the distance between adjacent plates is the channel height (b). The fins are characterized by their thickness (t_{f}), spacing (s_{f}), strip flow length (L_{f}), pitch ($p_{\mathrm{f}} = s_{\mathrm{f}} + t_{\mathrm{f}}$), and height ($h_{\mathrm{f}} = b - t_{\mathrm{f}}$). Using these characteristics, the hydraulic diameter (D_{h}), flow area (A_{flow}), base area (A_{base}), and fin area (A_{fin}) can be determined based on fin-specific relations [126] below.

$$D_\mathrm{h} = \frac{4 s_\mathrm{f} b L_\mathrm{f}}{2(s_\mathrm{f} L_\mathrm{f} + b L_\mathrm{f} + t_\mathrm{f} b) + t_\mathrm{f} s_\mathrm{f}} \tag{4.38}$$

$$A_\mathrm{flow} = s_\mathrm{f} h_\mathrm{f} \tag{4.39}$$

$$A_\mathrm{base} = 2(s_\mathrm{f} L_\mathrm{f} + t_\mathrm{f}(s_\mathrm{f} - t_\mathrm{f})/2) \tag{4.40}$$

$$A_\mathrm{fin} = 2(h_\mathrm{f} L_\mathrm{f} + h_\mathrm{f} t_\mathrm{f}) \tag{4.41}$$

The number of fins for each pass and channel on both sides can then be calculated:

$$n_\mathrm{f,x,wf} = \frac{L}{p_\mathrm{f}}, \;\; n_\mathrm{f,y,wf} = \frac{H}{L_\mathrm{f}} \tag{4.42}$$

$$n_\mathrm{f,x,exh} = \frac{L}{L_\mathrm{f}}, \;\; n_\mathrm{f,y,exh} = \frac{H}{p_\mathrm{f}} \tag{4.43}$$

From this the total cross-sectional area (or total flow area) for the flow follows:

$$A_\mathrm{c,wf} = n_\mathrm{ch,wf} \frac{n_\mathrm{f,x,wf}}{n_\mathrm{pass,wf}} A_\mathrm{flow} \tag{4.44}$$

$$A_\mathrm{c,exh} = n_\mathrm{ch,exh} \frac{n_\mathrm{f,y,exh}}{n_\mathrm{pass,exh}} A_\mathrm{flow} \tag{4.45}$$

With these definitions and knowledge of the transport properties, the dimensionless numbers for heat transfer can be determined. The mass flow ($\dot{m}$), cross-sectional area (A_c), hydraulic diameter (D_h), and dynamic viscosity (μ) give the Reynolds number (Re):

$$\mathrm{Re} = \frac{\dot{m} D_\mathrm{h}}{\mu A_\mathrm{c}} \tag{4.46}$$

The Prandtl number (Pr) is calculated from the specific heat capacity (c_p), dynamic viscosity (μ), and thermal conductivity (λ):

$$\mathrm{Pr} = \frac{c_\mathrm{p} \mu}{\lambda} \tag{4.47}$$

The heat transfer coefficient (α) is determined from the Nusselt number (Nu):

$$\mathrm{Nu} = \frac{\alpha D_\mathrm{h}}{\mu} \tag{4.48}$$

To obtain the Nusselt number, fin-specific heat transfer relations for single- and two-phase are defined. For single-phase heat transfer, the following expression is used [126]:

$$\mathrm{Nu} = j \mathrm{Re} \mathrm{Pr}^{1/3} \tag{4.49}$$

Where:

$$j = 0.652\mathrm{Re}^{-0.540}\left(\frac{s_\mathrm{f}}{h_\mathrm{f}}\right)^{-0.154}\left(\frac{t_\mathrm{f}}{L_\mathrm{f}}\right)^{0.150}\left(\frac{t_\mathrm{f}}{s_\mathrm{f}}\right)^{-0.068} \cdot\left[1+5.269\cdot10^{-5}\mathrm{Re}^{1.34}\left(\frac{s_\mathrm{f}}{h_\mathrm{f}}\right)^{0.504}\left(\frac{t_\mathrm{f}}{L_\mathrm{f}}\right)^{0.456}\left(\frac{t_\mathrm{f}}{s_\mathrm{f}}\right)^{-1.06}\right]^{0.1} \tag{4.50}$$

The two-phase heat transfer coefficient is the sum of the nucleate boiling (α_nb) and convective (α_cv) components [126]:

$$\alpha = \alpha_\mathrm{nb} + \alpha_\mathrm{cv} \tag{4.51}$$

The nucleate boiling component is a function of the heat flux ($\dot{q}$), the molecular weight (M_w), and the reduced pressure (p_crit); it is defined as:

$$\alpha_\mathrm{nb} = 55\dot{q}^{2/3}MW^{-1/2}\left(\frac{p}{p_\mathrm{crit}}\right)^{0.225}\left[-\log_{10}\left(\frac{p}{p_\mathrm{crit}}\right)\right]^{-0.55} \tag{4.52}$$

The convective component is obtained from the saturated liquid heat transfer coefficient (α_l), which is calculated from the saturated liquid properties using Eq. (4.49). This coefficient is multiplied with with a factor (F) that depends on the steam quality (x) and the saturated liquid and vapor densities (ρ_l, ρ_v) and viscosities (μ_l, μ_v):

$$\alpha_\mathrm{cv} = F\alpha_\mathrm{l} \tag{4.53}$$

$$F = \left(1+\frac{28}{X_\mathrm{tt}}\right)^{0.372} \tag{4.54}$$

$$X_\mathrm{tt} = \left(\frac{1-x}{x}\right)^{0.9}\left(\frac{\rho_\mathrm{v}}{\rho_\mathrm{l}}\right)^{0.5}\left(\frac{\mu_\mathrm{v}}{\mu_\mathrm{l}}\right)^{0.1} \tag{4.55}$$

To calculate the heat transfer from the exhaust gas to the working fluid, the evaporator is discretized into a number of elements; a representative discretization scheme is shown in Fig. 4.3. For each element, the heat transfer relations are solved based on the average state of that element and the heat transfer surface (A_s) is defined as the sum of the base (A_base) and fin (A_fin) surface areas:

$$A_\mathrm{s,el} = A_\mathrm{base,el} + A_\mathrm{fin,el} \tag{4.56}$$

The heat transfer is calculated for all channels simultaneously by multiplying the total surface area of the element by its number of channels:

$$A_\mathrm{s,el,tot} = n_\mathrm{ch,wf}A_\mathrm{s,el} \tag{4.57}$$

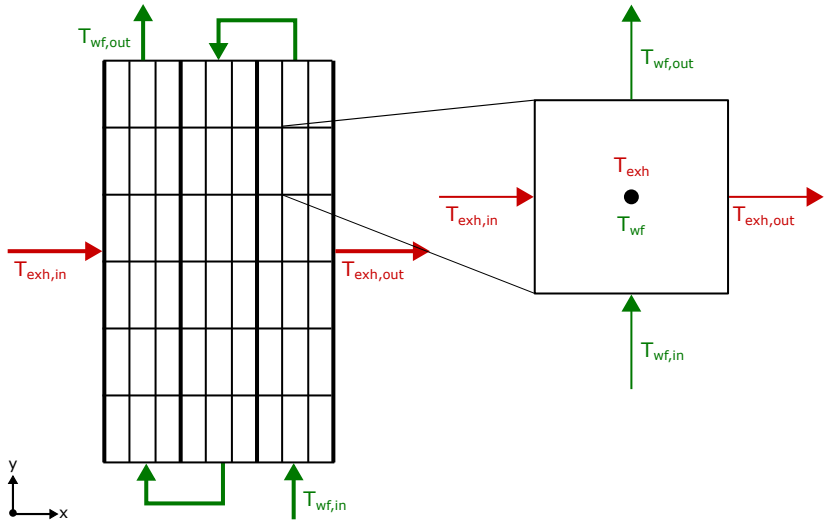

Fig. 4.3: Representative discretization scheme for the exhaust evaporator.

Knowing the total surface area, the heat transfer for each element can be calculated:

$$\dot{Q}_{\mathrm{el}} = U_{\mathrm{el}} A_{\mathrm{s,el,tot}} (T_{\mathrm{exh,el}} - T_{\mathrm{wf,el}}) \tag{4.58}$$

Here, the overall heat transfer coefficient (U) consists of the several distinct contributions:

$$\frac{1}{U} = \frac{1}{\alpha_{\mathrm{wf}}} + \frac{t_{\mathrm{w}}}{\lambda_{\mathrm{w}}} + \frac{1}{\alpha_{\mathrm{exh}}} \approx \frac{1}{\alpha_{\mathrm{wf}}} + \frac{1}{\alpha_{\mathrm{exh}}} \tag{4.59}$$

4.2.2.4 Expander

The expander model is based on a two-cylinder uniflow reciprocating piston expander. The high pressure, high temperature steam is admitted through the inlet port, which is closed by a valve attached to a valve spring and periodically opened by a push-rod mounted to the piston head. The steam exits at a reduced pressure and temperature through the outlet port at the bottom, which is uncovered when the piston travels down. The expander operation is described by a semi-empirical model that was originally developed for a scroll expander [118] and then adapted for reciprocating piston operation [127, 128]. The model is schematically depicted in Fig. 4.4; it accounts for the pressure drop on the suction and exhaust sides of the expansion, expansion and compression in the cylinder, internal and external heat losses, and mass leakage to the environment. Importantly, it also includes the ability to predict performance for a range of different working fluids. The model represents a single cylinder, so its predicted mass flows and energy changes must be multiplied by the number of cylinders in the expander when comparing its output to experimental results.

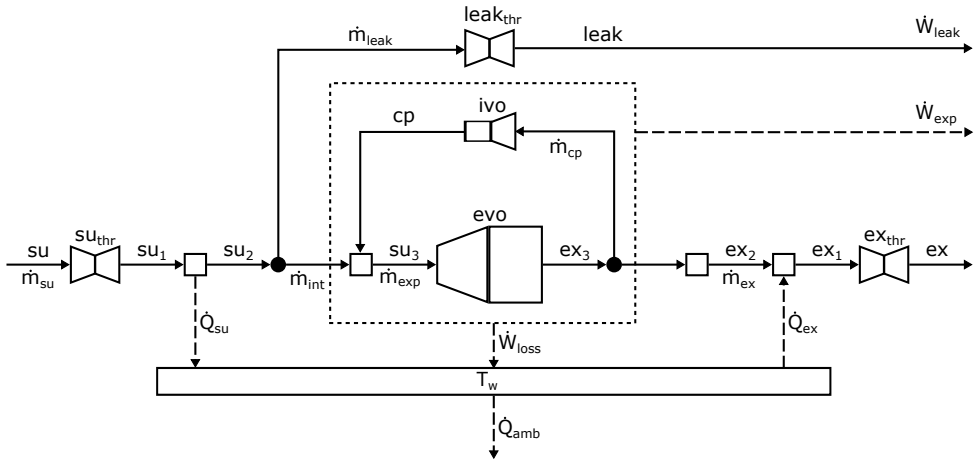

Fig. 4.4: The semi-empirical model piston expander model.

The semi-empirical model uses thermodynamic equations containing tuning parameters whose values must be determined using a calibration procedure that is based on experimental data. By using time-averaged parameters and properties, the dynamic and sequential operation of the expander is modeled as a steady-state operation in which multiple physical processes occur simultaneously. This section describes the physical processes that occur during expander operation and the adaptations needed to model the expander operation with different working fluids.

Supply pressure drop ($\mathbf{su} \rightarrow \mathbf{su_1}$)

As shown in Eq. (4.60), the adiabatic supply pressure drop is modeled by treating the supply mass flow as an isentropic flow ($s_{\mathrm{su,thr}} = s_{\mathrm{su}}$) through a converging nozzle. Subsequently, the kinetic energy is converted into enthalpy ($h_{\mathrm{su1}} = h_{\mathrm{su}}$) at constant pressure. The supply diameter (d_{su}) represents the mean effective diameter, which is determined during the calibration of the expander model.

$$\dot{m}_{\mathrm{su}} = \rho_{\mathrm{su}} \frac{\pi d_{\mathrm{su}}^2}{4} \sqrt{2(h_{\mathrm{su}} - h_{\mathrm{su,thr}})} \tag{4.60}$$

To account for supersonic flow, the throat pressure ($p_{\mathrm{su,thr}}$) is defined as the maximum of the outlet pressure (p_{su1}) and the critical pressure ($p_{\mathrm{crit,su}}$):

$$p_{\mathrm{su,thr}} = \max(p_{\mathrm{su1}}, p_{\mathrm{crit,su}}) \tag{4.61}$$

The critical supply pressure is determined based on the relation for a perfect gas [129]:

$$p_{\mathrm{crit,su}} = p_{\mathrm{su}} \left(\frac{2}{\gamma_{\mathrm{su}} + 1} \right)^{\left(\frac{\gamma_{\mathrm{su}}}{\gamma_{\mathrm{su}} - 1} \right)} \tag{4.62}$$

Supply heat transfer ($\mathbf{su_1 \rightarrow su_2}$)

The supply heat transfer is assumed to be isobaric ($p_{su2} = p_{su1}$) and is calculated using a fictitious envelope (representing the metal parts of the expander) with a uniform wall temperature (T_w). The relation for a single-stream steady-flow heat exchanger [130] is used to calculate the supply heat transfer, which is expressed as

$$\dot{Q}_{su} = \dot{m}_{su} c_{p,su1} \left[1 - e^{\left(\frac{-AU_{su}}{\dot{m}_{su} c_{p,su1}} \right)} \right] (T_{su1} - T_w) \tag{4.63}$$

The global heat transfer coefficient (AU_{su}) can be calculated with Eq. (4.64) by correcting the nominal global heat transfer coefficient ($AU_{su,n}$) for deviations in mass flow ($\dot{m}_{su}$) from the nominal flow ($\dot{m}_{su,n}$), which is computed using the relation for turbulent flow in a smooth tube [130] assuming constant fluid properties.

$$AU_{su} = AU_{su,n} \left(\frac{\dot{m}_{su}}{\dot{m}_{su,n}} \right)^{0.8} \tag{4.64}$$

Having determined the heat transfer, the enthalpy after heat transfer (h_{su2}) follows:

$$h_{su2} = h_{su1} - \frac{\dot{Q}_{su}}{\dot{m}_{su}} \tag{4.65}$$

Leakage mass flow rate ($\mathbf{su_2 \rightarrow leak}$)

The leakage mass flow in Eq. (4.66) is calculated by combining the isentropic nozzle ($s_{leak,thr} = s_{su2}$) with the isobaric diffuser ($p_{leak} = p_{leak,thr}$, $h_{leak} = h_{su2}$) in the same way as is done when calculating the supply pressure drop. The average effective leakage area (A_{leak}) must be determined during the calibration.

$$\dot{m}_{leak} = \rho_{leak,thr} A_{leak} \sqrt{2(h_{su2} - h_{leak,thr})} \tag{4.66}$$

Since the leakage flow enters the expander crankcase rather than returning, the throat pressure is the greater of the ambient pressure (p_{amb}) and the critical pressure ($p_{crit,leak}$):

$$p_{leak,thr} = \max(p_{amb}, p_{crit,leak}) \tag{4.67}$$

$$p_{crit,leak} = p_{su2} \left(\frac{2}{\gamma_{su2} + 1} \right)^{\left(\frac{\gamma_{su2}}{\gamma_{su2} - 1} \right)} \tag{4.68}$$

Since part of the mass flow is rejected to the environment ($\dot{m}_{leak}$), the supply flow ($\dot{m}_{su}$) is reduced to the internal flow available for expansion ($\dot{m}_{int}$), expressed as

$$\dot{m}_{int} = \dot{m}_{su} - \dot{m}_{leak} \tag{4.69}$$

Expander inlet mixing ($\mathbf{su_2 \rightarrow su_3}$)

In the cylinder, some of the mass is compressed ($\dot{m}_{\mathrm{cp}}$) and added to the internal mass ($\dot{m}_{\mathrm{int}}$) under isobaric conditions ($p_{\mathrm{su3}} = p_{\mathrm{su2}}$), in accordance with Eq. (4.70). The enthalpy at the start of the expansion (h_{su3}) can then be computed using Eq. (4.71).

$$\dot{m}_{\mathrm{exp}} = \dot{m}_{\mathrm{int}} + \dot{m}_{\mathrm{cp}} \tag{4.70}$$

$$h_{\mathrm{su3}} = \frac{\dot{m}_{\mathrm{int}} h_{\mathrm{su2}} + \dot{m}_{\mathrm{cp}} h_{\mathrm{cp}}}{\dot{m}_{\mathrm{exp}}} \tag{4.71}$$

Expansion ($\mathbf{su_3 \rightarrow ex_3}$)

Eq. (4.72) shows the total mass displaced in the expander, which is the available mass at inlet valve closing ($\rho_{\mathrm{su3}} f_{\mathrm{a}} V_{\mathrm{s}}$) multiplied by the rotational speed of the expander (N_{exp}).

$$\dot{m}_{\mathrm{exp}} = \frac{N_{\mathrm{exp}}}{60} \rho_{\mathrm{su3}} f_{\mathrm{a}} V_{\mathrm{s}} \tag{4.72}$$

The internal power during the expansion ($\dot{W}_{\mathrm{int,exp}}$) can be divided into three components: suction at constant pressure ($V_{\mathrm{c}} \rightarrow V_{\mathrm{ivc}}$), adiabatic and reversible expansion ($V_{\mathrm{ivc}} \rightarrow V_{\mathrm{evo}}$), and discharge at constant volume ($p_{\mathrm{evo}} \rightarrow p_{\mathrm{ex3}}$), giving the following expression:

$$\dot{W}_{\mathrm{int,exp}} = \dot{m}_{\mathrm{exp}} (h_{\mathrm{su3}} - h_{\mathrm{evo}}) + \frac{\dot{m}_{\mathrm{exp}}}{\rho_{\mathrm{evo}}} (p_{\mathrm{evo}} - p_{\mathrm{ex3}}) \tag{4.73}$$

The density at the end of the reversible expansion ($s_{\mathrm{evo}} = s_{\mathrm{su3}}$) is given by

$$\rho_{\mathrm{evo}} = \frac{\rho_{\mathrm{su3}}}{r_{\mathrm{v,exp}}} \tag{4.74}$$

With the inlet enthalpy (h_{su3}), the internal expansion power ($\dot{W}_{\mathrm{int,exp}}$), and the mass flow ($\dot{m}_{\mathrm{exp}}$) known, the expander exhaust enthalpy follows:

$$h_{\mathrm{ex3}} = h_{\mathrm{su3}} - \frac{\dot{W}_{\mathrm{int,exp}}}{\dot{m}_{\mathrm{exp}}} \tag{4.75}$$

Compression ($\mathbf{ex_3 \rightarrow cp}$)

During compression, the total displaced mass over time is the mass trapped in the cylinder after the exhaust valve closes ($\rho_{\mathrm{ex3}} f_{\mathrm{p}} V_{\mathrm{s}}$) multiplied by the expander speed (N_{exp}):

$$\dot{m}_{\mathrm{cp}} = \frac{N_{\mathrm{exp}}}{60} \rho_{\mathrm{ex3}} f_{\mathrm{p}} V_{\mathrm{s}} \tag{4.76}$$

The internal power during the compression stroke is defined as:

$$\dot{W}_{\mathrm{int,cp}} = \dot{m}_{\mathrm{cp}}(h_{\mathrm{ivo}} - h_{\mathrm{ex3}}) + \frac{\dot{m}_{\mathrm{cp}}}{\rho_{\mathrm{ivo}}}(p_{\mathrm{cp}} - p_{\mathrm{ivo}}) \tag{4.77}$$

After the reversible compression ($s_{\mathrm{ivo}} = s_{\mathrm{ex3}}$), the density in the cylinder will be equal to

$$\rho_{\mathrm{ivo}} = \rho_{\mathrm{ex3}} r_{\mathrm{v,cp}} \tag{4.78}$$

When the inlet valve opens, the pressures equalize ($p_{\mathrm{cp}} = p_{\mathrm{su2}}$) and the enthalpy becomes

$$h_{\mathrm{cp}} = h_{\mathrm{ex3}} + \frac{\dot{W}_{\mathrm{int,cp}}}{\dot{m}_{\mathrm{cp}}} \tag{4.79}$$

Expander exhaust mixing ($\mathbf{ex_3} \rightarrow \mathbf{ex_2}$)

Since the leakage flow is rejected to the environment, no mixing occurs, which means constant thermodynamic properties ($p_{\mathrm{ex2}} = p_{\mathrm{ex3}}$, $h_{\mathrm{ex2}} = h_{\mathrm{ex3}}$) and mass flow ($\dot{m}_{\mathrm{ex}} = \dot{m}_{\mathrm{int}}$).

Exhaust heat transfer ($\mathbf{ex_2} \rightarrow \mathbf{ex_1}$)

The isobaric ($p_{\mathrm{ex1}} = p_{\mathrm{ex2}}$) exhaust heat transfer is determined using the expression for a single-stream steady-flow heat exchanger [130], scaling the global heat transfer coefficient (AU_{ex}) by the exhaust mass flow ($\dot{m}_{\mathrm{ex}}$). The enthalpy (h_{ex1}) then follows:

$$\dot{Q}_{\mathrm{ex}} = \dot{m}_{\mathrm{ex}} c_{\mathrm{p,ex2}} \left[1 - e^{\left(\frac{-AU_{\mathrm{ex}}}{\dot{m}_{\mathrm{ex}} c_{\mathrm{p,ex2}}}\right)}\right] (T_{\mathrm{w}} - T_{\mathrm{ex2}}) \tag{4.80}$$

$$AU_{\mathrm{ex}} = AU_{\mathrm{ex,n}} \left(\frac{\dot{m}_{\mathrm{ex}}}{\dot{m}_{\mathrm{ex,n}}}\right)^{0.8} \tag{4.81}$$

$$h_{\mathrm{ex1}} = h_{\mathrm{ex2}} + \frac{\dot{Q}_{\mathrm{ex}}}{\dot{m}_{\mathrm{ex}}} \tag{4.82}$$

Exhaust pressure drop ($\mathbf{ex_1} \rightarrow \mathbf{ex}$)

The adiabatic exhaust pressure drop is determined by combining the isentropic nozzle ($s_{\mathrm{ex,thr}} = s_{\mathrm{ex1}}$) with the isobaric diffuser ($h_{\mathrm{ex}} = h_{\mathrm{ex1}}$) to obtain the corresponding pressure downstream of the nozzle while the throat pressure is limited by the critical pressure:

$$\dot{m}_{\mathrm{ex}} = \rho_{\mathrm{ex1}} \frac{\pi d_{\mathrm{ex}}^2}{4} \sqrt{2(h_{\mathrm{ex1}} - h_{\mathrm{ex,thr}})} \tag{4.83}$$

$$p_{\mathrm{ex,thr}} = \max(p_{\mathrm{ex}}, p_{\mathrm{crit,ex}}) \tag{4.84}$$

$$p_{\mathrm{crit,ex}} = p_{\mathrm{ex1}} \left(\frac{2}{\gamma_{\mathrm{ex1}} + 1} \right)^{\left(\frac{\gamma_{\mathrm{ex1}}}{\gamma_{\mathrm{ex1}} - 1} \right)} \tag{4.85}$$

Ambient heat transfer

The ambient heat transfer depends on the global heat transfer coefficient (AU_{amb}) and the difference between the wall temperature (T_{w}) and the ambient temperature (T_{amb}):

$$\dot{Q}_{\mathrm{amb}} = AU_{\mathrm{amb}}(T_{\mathrm{w}} - T_{\mathrm{amb}}) \tag{4.86}$$

Energy balance

The internal power output and net shaft power of the expander are given by

$$\dot{W}_{\mathrm{int}} = \dot{W}_{\mathrm{int,exp}} - \dot{W}_{\mathrm{int,cp}} \tag{4.87}$$

$$\dot{W}_{\mathrm{exp}} = \dot{W}_{\mathrm{int}} - \dot{W}_{\mathrm{loss}} \tag{4.88}$$

The losses in the expander are represented by three different terms:

$$\dot{W}_{\mathrm{loss}} = \dot{W}_{\mathrm{loss,0}} + \alpha_{\mathrm{loss}} \dot{W}_{\mathrm{int}} + 2\pi C_{\mathrm{loss}} \frac{N_{\mathrm{exp}}}{60} \tag{4.89}$$

To calculate the wall temperature (T_{w}), the energy balance based on the four different contributors to the heat transfer is solved using the following expression:

$$\dot{Q}_{\mathrm{su}} + \dot{W}_{\mathrm{loss}} = \dot{Q}_{\mathrm{ex}} + \dot{Q}_{\mathrm{amb}} \tag{4.90}$$

The total energy balance over the expander is then defined as:

$$\dot{m}_{\mathrm{su}} h_{\mathrm{su}} - \dot{m}_{\mathrm{ex}} h_{\mathrm{ex}} = \dot{W}_{\mathrm{exp}} + \dot{W}_{\mathrm{leak}} + \dot{Q}_{\mathrm{amb}} \tag{4.91}$$

Expander performance

The non-dimensional performance of the expander can be expressed using a filling factor and an isentropic efficiency. The definition of the filling factor (ϕ_{f}) for a piston expander [128] is shown in Eq. (4.92). For expansion in the two-phase region, an isentropic filling factor is introduced in Eq. (4.93). This factor depends on the isentropic exhaust density ($\rho_{\mathrm{ex,is}}$), meaning isentropic expansion is assumed ($s_{\mathrm{ex}} = s_{\mathrm{su}}$).

$$\phi_{\mathrm{f}} = \frac{\dot{m}_{\mathrm{su}}}{\dot{m}_{\mathrm{th}}} = \frac{\dot{m}_{\mathrm{su}}}{\frac{N_{\mathrm{exp}}}{60}(\rho_{\mathrm{su}} f_{\mathrm{a}} - \rho_{\mathrm{ex}} f_{\mathrm{p}}) V_{\mathrm{s}}} \tag{4.92}$$

$$\phi_{\mathrm{f,is}} = \frac{\dot{m}_{\mathrm{su}}}{\frac{N_{\mathrm{exp}}}{60}(\rho_{\mathrm{su}} f_{\mathrm{a}} - \rho_{\mathrm{ex,is}} f_{\mathrm{p}}) V_{\mathrm{s}}} \tag{4.93}$$

Since the definition of the isentropic efficiency assumes adiabatic operation (which is typically not the case for a large reciprocating piston expander), it cannot be used to evaluate the performance of the expander [118]. Instead, the expander efficiency defined in Eq. (4.94) is used, which is based on the expander shaft power ($\dot{W}_{\mathrm{exp}}$).

$$\eta_{\mathrm{exp}} = \frac{\dot{W}_{\mathrm{exp}}}{\dot{W}_{\mathrm{is}}} = \frac{2\pi\tau_{\mathrm{exp}}\frac{N_{\mathrm{exp}}}{60}}{\dot{m}_{\mathrm{su}}(h_{\mathrm{su}} - h_{\mathrm{ex,is}})} \tag{4.94}$$

From the expander efficiency, the shaft power can be calculated. However, the expander outlet enthalpy is still unknown because the definition does not include the leakage power and heat loss terms. The isentropic effectiveness (ϵ_{is}) however does includes these terms:

$$\begin{aligned}
\epsilon_{\mathrm{is}} =& \frac{\dot{m}_{\mathrm{su}}(h_{\mathrm{su}} - h_{\mathrm{ex}})}{\dot{m}_{\mathrm{su}}(h_{\mathrm{su}} - h_{\mathrm{ex,is}})} \\
=& \frac{\dot{W}_{\mathrm{exp}} + \dot{m}_{\mathrm{leak}}(h_{\mathrm{leak}} - h_{\mathrm{ex}}) + \dot{Q}_{\mathrm{amb}}}{\dot{W}_{\mathrm{is}}} \\
=& \epsilon_{\mathrm{is,sh}} + \frac{\dot{W}_{\mathrm{leak}}}{\dot{W}_{\mathrm{is}}} + \frac{\dot{Q}_{\mathrm{amb}}}{\dot{W}_{\mathrm{is}}}
\end{aligned} \tag{4.95}$$

Change of Working Fluid

To evaluate expander performance for fluids other than water, the model can be extended using relations previously developed for scroll expanders [131, 132]. Assuming the change of fluid only affects the thermodynamic properties and the global heat transfer coefficients (AU_{su} and AU_{ex}), the heat transfer coefficients can be modified to simulate different working fluids. The heat transfer coefficients are typically expressed as functions of the Nusselt number (Nu), thermal conductivity (λ), and a reference length (L):

$$U = \frac{\mathrm{Nu}\lambda}{L} \tag{4.96}$$

The Nusselt number (Nu) is calculated a for a turbulent flow in a smooth tube [130] where $m = 0.4$ in the case of heating and $m = 0.3$ for cooling:

$$\mathrm{Nu} = 0.023\mathrm{Re}^{0.8}\mathrm{Pr}^{m} \tag{4.97}$$

$$\mathrm{Re} = \frac{\rho v d}{\mu} = \frac{4\dot{m}}{\pi\mu D} \tag{4.98}$$

$$\mathrm{Pr} = \frac{c_{\mathrm{p}}\mu}{\lambda} \tag{4.99}$$

The new global heat transfer coefficient can now be expressed in relation to the reference:

$$\frac{AU}{AU_{\text{ref}}} = \frac{\text{Nu}\lambda}{\text{Nu}_{\text{ref}}\lambda_{\text{ref}}} \tag{4.100}$$

Filling in the dimensionless numbers and rewriting gives:

$$\frac{AU}{AU_{\text{ref}}} = \left(\frac{\text{Re}}{\text{Re}_{\text{ref}}}\right)^{0.8} \left(\frac{\text{Pr}}{\text{Pr}_{\text{ref}}}\right)^{m} \left(\frac{\lambda}{\lambda_{\text{ref}}}\right) \tag{4.101}$$

$$AU = AU_{\text{ref}} \left(\frac{\dot{m}}{\dot{m}_{\text{ref}}}\right)^{0.8} \left(\frac{\mu}{\mu_{\text{ref}}}\right)^{m-0.8} \left(\frac{c_{\text{p}}}{c_{\text{p,ref}}}\right)^{m} \left(\frac{\lambda}{\lambda_{\text{ref}}}\right)^{1-m} \tag{4.102}$$

4.2.2.5 Condenser

The condenser is not modeled in detail; instead it is modeled as as a heat sink for which the rejected heat is the energy change over the condenser:

$$\dot{Q}_{\text{cond}} = \dot{m}_{\text{cond}}(h_{\text{cond,in}} - h_{\text{cond,out}}) \tag{4.103}$$

4.2.3 Modeling Approach

The simulations were performed using MATLAB [125] with fluid maps for the thermodynamic and transport properties, which were obtained from the CoolProp [92] database. The pump speed was adjusted to satisfy the superheating constraint and for every pump speed the expander speed was varied over the specified range. Using a golden section search, the expander speed giving the maximum power output for a specific engine operating point was determined. At each combination of engine operating point, pump speed, and expander speed, the evaporator pressure was determined using a constrained non-linear solver (*fmincon*) by matching the pump and expander mass flows.

5 Summary of Publications

Publication A

"Thermodynamic Potential of Twelve Working Fluids in Rankine and Flash Cycles for Waste Heat Recovery in Heavy Duty Diesel Engines"

The goal of this initial simulation study was to assess the maximum thermodynamic potential of four selected thermodynamic cycles for waste heat recovery from different heat sources in a heavy-duty Diesel engine. Twelve working fluids were selected and simulated in four thermodynamic cycles: the organic Rankine cycle (ORC), the transcritical Rankine cycle (TRC), the trilateral flash cycle (TFC), and the single flash cycle (SFC). In subsequent publications, the SFC is referred to instead as the organic flash cycle (OFC). Optimistic boundary conditions and constraints were imposed to determine the best possible performance for each combination of heat source, working fluid, and thermodynamic cycle. The first step was to evaluate the potential for WHR from the four heat sources: the CAC, the coolant, the EGRC, and the exhaust gases. An energy and exergy analysis over the full operating range of the engine revealed that all four heat sources had potential for WHR both in terms of quantity and quality. A representative A50 (151 kW) engine operating point was selected to study the performance of the different cycles and working fluids. The best performance for the CAC was achieved with the TFC and SFC, regardless of the choice of working fluid, showing a maximum power output of 2 kW. For the coolant, the best power output of around 5 kW was achieved with the ORC. In the case of the EGRC, the best performance of 8 kW was achieved using the TRC with methanol as the working fluid. In the ORC and TRC, acetone and ethanol gave the best performance with power outputs between 6 and 7 kW. For the exhaust gases, all cycles achieved good recoveries of 5 to 6 kW, where the best result was achieved with acetone in the ORC. Additionally, the effect of varying the engine and cycle conditions was investigated by performing a sensitivity analysis on the five most relevant constraints: the condensation temperature, the source outlet temperature, the maximum degree of superheating, the engine operating points, and the expander isentropic efficiencies. The sensitivity analysis revealed that variations in all five constraints caused significant changes in cycle power output, with deviations ranging from 1 to 8 kW.

Published in Energy (2018)

Author contributions: All authors conceived of the presented idea. The author of this thesis performed the modeling, simulations, and analysis and wrote the manuscript with contributions from all authors.

Publication B

"Thermodynamic Cycle and Working Fluid Selection for Waste Heat Recovery in a Heavy Duty Diesel Engine"

This publication presented an extended and more practical study on the thermodynamic performance of the four cycles considered for waste heat recovery from the different heat sources in a heavy-duty engine. The study reported in the previous publication was augmented by increasing the number of working fluids from 12 to 56. Additionally, more stringent boundary conditions and constraints were imposed to obtain a more realistic representation of the thermodynamic performance. Three heat sources (the coolant, EGRC, and exhaust gases) and four thermodynamic cycles (the ORC, TRC, TFC, and OFC) were simulated for a 100 kW engine operating point. The highest outputs were obtained with the ORC and TRC when using the EGRC and exhaust gases as the heat source, with power outputs of around 2.5 kW and 5 kW, respectively. The ORC performed best for the coolant, delivering a maximum power output of 1.5 kW. The TFC gave a slightly lower performance at 2 kW for the EGRC, 4 kW for the exhaust gases and 1 kW for the coolant. The OFC performed worst, with power outputs of 1.5 kW for the EGRC, 3 kW for the exhaust, and 0.5 kW for the coolant. In general, the best performing working fluids were acetone, benzene, cyclopentane, ethanol, and methanol. Despite achieving lower power outputs, R1233zd(E), MM, and Novec649 were also identified as good candidates because of their low flammability and toxicity.

Published as SAE Technical Paper 2018-01-1371 (2018)

Author contributions: All authors conceived of the presented idea. The author of this thesis performed the modeling, simulations, and analysis and wrote the manuscript with contributions from all authors.

Publication C

"Combining Low- and High-Temperature Heat Sources in a Heavy Duty Diesel Engine for Maximum Waste Heat Recovery Using Rankine and Flash Cycles"

For the two previous studies, each heat source was considered individually for waste heat recovery. In this publication, different heat sources were combined using two single-loop configurations. The first configuration (Conf-1) combined the CAC, coolant, EGRC, and exhaust gases in series, while the second configuration (Conf-2) combined the CAC, EGRC, and exhaust gases in series. Four thermodynamic cycles (the ORC, TRC, TFC, and OFC) were simulated with fifty working fluids and a recuperator was added to study its effect on the cycle performance. The two configurations were simulated at three engine operating points that are dominant in the long haul duty cycle (A25, A50, and A75) and weighted based on the relative time spent at each of these operating point during the driving cycle. For Conf-1, the highest power outputs were obtained for the ORC with ammonia, sulfurdioxide, acetone, cyclopentane, and R1234ze(Z), which gave weighted power outputs between 6.4 and 7.1 kW. For Conf-2, both the ORC and TRC performed best, giving power outputs between 6.8 and 8.2 kW with acetone, methanol, cyclopentane, ethanol, and isohexane as the working fluid. The TFC and especially the OFC performed considerably worse. The use of a recuperator significantly increased net power output (up to 25 %) for Conf-1 and increased the thermodynamic efficiency but not the net power output for Conf-2. The improved thermodynamic efficiency reduced the load on the condenser, which is an important consideration for automotive applications.

Published in Proceedings of 2nd ETA Conference, Berlin, Germany (2018)

Author contributions: All authors conceived of the presented idea. The author of this thesis performed the modeling, simulations, and analysis and wrote the manuscript with contributions from all authors.

Publication D

"Experimental Investigation and Modeling of a Reciprocating Piston Expander for Waste Heat Recovery from a Truck Engine"

An experimental setup with a two-cylinder reciprocating piston expander was constructed to recover waste heat from the exhaust gases of a 12.8 L heavy-duty Diesel engine using water as the working fluid. This publication focused on the performance of the reciprocating piston expander in the setup. Based on the experimental results, a semi-empirical model of the expander was calibrated. Subsequently, this model was adapted so that it could be used to predict the effects of different working fluids and changes in geometry. During the experimental campaign, the expander performance was measured at 41 experimental points for four engine operating points (between 75 and 151 kW) over a range of expander speeds (between 200 and 1800 rpm). The measured expander shaft power ranged from 0.1 to 3 kW, corresponding to a relative power output of 0.1 to 2.6 % of the engine power. Using the semi-empirical model, the separate effects of the valve clearance and timing, heat losses, mechanical losses, pressure drop, and leakage were quantified. Simulations using six different working fluids showed that the expander's filling factor (i.e. volumetric efficiencies) varied between 0.5 and 2.2 and its isentropic effectiveness (i.e. efficiencies) varied between 0.01 and 0.50, depending on the cycle conditions and working fluid. Simulations of the dominant engine operating points in a driving cycle showed that the best performance was achieved with acetone and R1233zd(E) using an expander with an optimized built-in volume ratio and inlet valve timing.

Published in Applied Thermal Engineering (2021)

Author contributions: All authors conceived of the presented idea. The author of this thesis planned and carried out the experiments, performed the modeling, simulations, and analysis, and wrote the manuscript with contributions from all authors.

Publication E

"Exhaust Waste Heat Recovery from a Heavy-Duty Truck Engine: Experiments and Simulations"

The high-temperature waste heat recovery setup described in paper D, in which the heat is recovered from the exhaust gases of a 12.8 L heavy-duty Diesel engine using water as the working fluid, was used to evaluate the performance of the full Rankine cycle. The experimental results from the previous publication were extended with five additional experimental sets whose results were used to calibrate and validate models of the main components in the cycle, namely the pump, pump bypass valve, evaporator, expander, and condenser. The experiments enabled the development of more detailed component models that could be used to estimate the performance of the system under conditions outside the experimental range, with different working fluids, and over a driving cycle. Experimental results with expander power output measurements were obtained for a limited range of engine operating points, revealing an expander power between 0.1 and 3 kW with water as the working fluid. Using steady-state models calibrated against the experimental data, the performance of the WHR system was simulated over the full operating range of the engine during a long haul driving cycle. With water as the working fluid, the predicted net power output ranged between 0.5 and 5.7 kW during the driving cycle. Simulations were also performed with cyclopentane and ethanol as the working fluids instead of water; in these cases, the net power output varied between 1.8 and 9.6 kW and between 1.0 and 7.8 kW, respectively. The recovered energy relative to the engine power (which is roughly equal to the reduction in fuel consumption) during the driving cycle was 3.4 % for cyclopentane, 2.5 % for ethanol, and 1.6 % for water.

Submitted to Energy (2021)

Author contributions: All authors conceived of the presented idea. The author of this thesis planned and carried out the experiments, performed the modeling, simulations, and analysis, and wrote the manuscript with contributions from all authors. Olof Erlandsson performed the modeling and simulations of the TitanX heat exchanger model.

Publication F

"Optimization and Evaluation of a Low Temperature Waste Heat Recovery System for a Heavy Duty Engine over a Transient Cycle"

Engine experiments on a 12.7 L heavy-duty Diesel engine were combined with a multi-linear regression analysis to evaluate the effect of elevated coolant temperatures on the indicated engine efficiency at a range of engine loads and speeds. The results of these experiments were used as inputs for steady-state ORC models to predict the recoverable power using ten different working fluids in a dual-loop configuration with the exhaust gases and the coolant as the heat sources. During the experiments, the engine coolant temperature was increased from 80 to 140 °C with no noticeable effect on the engine efficiency, although the exhaust gas outlet temperature and coolant heat transfer were affected. The simulations with an engine coolant temperature of 140 °C showed that cyclopentane was the best performing working fluid for heat recovery from the coolant, giving a maximum power output of 3.5 kW. Methanol performed best for the exhaust gases, giving a maximum recovery of around 11 kW. The engine data and steady-state simulation results for cyclopentane and methanol were used to predict the recovery performance over the world harmonized transient cycle (WHTC). It was found that raising the coolant temperature could improve the fuel consumption reduction from 5.3 % to 9 % when using both the exhaust and coolant as heat sources for waste heat recovery.

Published as SAE Technical Paper 2020-01-2033 (2020)

Author contributions: The paper was written by Vikram Singh. The experimental work was done by Vikram Singh with assistance from Xiufei Li and with Sebastian Verhelst acting as the supervisor for the work done. The Rankine cycle modeling and simulations were performed by the author of this thesis with Karin Munch and Sven B. Andersson acting as supervisors.

Publication G

"Experimental Results of an Organic Rankine Cycle with R1233zd(E) for Waste Heat Recovery from the Coolant of a Heavy-Duty Truck Engine"

To complement the experimental setup for high-temperature waste heat recovery, an experimental setup with an ORC for low-temperature waste heat recovery was constructed. In this setup, the heat from the engine coolant of a 12.8 L heavy-duty Diesel engine was recovered using R1233zd(E) as the working fluid. Nine engine operating points (A25 – C75) were tested at various pump and expander speeds. The maximum expander shaft power was 1.2 kW, the maximum estimated net power was 0.7 kW, and the maximum net power relative to the engine was 0.7 %. Filling factors (i.e. volumetric effiencies) and expander efficiencies ranged from 0.9 to 1.6 and 0.3 to 0.8, respectively. A simple cycle model was developed using empirical models that were fitted to the experimental results. In addition to this standard cycle model, an optimum model was defined using more optimistic but still realistic efficiencies for the pump and expander. Simulations were performed using both the standard and optimum model with typical radiator mass flows and inlet temperatures for a long haul driving cycle. The predicted recovered energy relative to the engine power (i.e. the predicted reduction in fuel consumption) was 0.73 % for the standard system and 1.29 % for the optimum system.

Submitted to Energy Conversion and Management (2021)

Author contributions: All authors conceived of the presented idea. The author of this thesis designed and constructed the experimental setup, planned and carried out the experiments, performed the modeling, simulations, and analysis, and wrote the manuscript with contributions from all authors.

6 Discussion

This chapter compares the performance of the low- and high-temperature WHR systems and investigates their performance under conditions outside the ranges available from the experiments. The results presented in this chapter are based on the experimental data, the calibrated models, and the driving cycles reported in Publication E and G for high- and low-temperature WHR, respectively. It must be kept in mind that these systems were not optimized and better performance should be achievable. To facilitate comparison, results are given identifiers indicating whether they relate to low-temperature (LT) or high-temperature (HT) WHR. Additionally, the temperature range is indicated by the letter T followed by a number and the condensing pressure is indicated by the letter P followed by a number. For example, results referring to low-temperature WHR with heat source temperatures starting at 75 °C and a condensing pressure of 3 bar would have the identifier LT_T075P3.

The discussion is divided into three main topics. Section 6.1 compares low- and high-temperature waste heat recovery systems, evaluating the range of operating conditions in the cycle and the performance achieved during two different driving cycles. Section 6.2 presents simulations conducted to determine how the power output and heat rejection are affected by raising the coolant temperature while keeping the mass flow and heat transfer rate from the engine constant over a driving cycle. Finally, Section 6.3 discusses the heat rejection during a driving cycle.

6.1 Low-Temperature vs. High-Temperature WHR

This section compares the operating conditions and performance of the ORCs for low-temperature waste heat recovery (LT-WHR) and high-temperature waste heat recovery (HT-WHR). The results of the steady-state cycle simulations for both systems (taken from Publications E and G) are shown in Table 6.1. In these simulations, R1233zd(E) was used as working fluid in the LT-WHR system and cyclopentane in the HT-WHR system. Simulations were performed for 16 grid points that represent the whole engine operating range during a driving cycle. Because of differences in the available data for LT-WHR and HT-WHR, different driving cycle were simulated for the two systems.

Table 6.1: Range of cycle conditions at 16 engine operating points for low-temperature and high-temperature WHR. Two different driving cycles were used.

	$\dot{m}_{\mathrm{pmp}}$ g/s	p_{cond} bar	p_{evap} bar	T_{cond} °C	T_{evap} °C	$T_{\mathrm{exp,in}}$ °C	$T_{\mathrm{exp,out}}$ °C
LT_T075P3	145 - 440	3.0	4.4 - 7.4	51	64 - 85	70 - 88	61 - 70
HT_T240P1	39 - 142	1.1	19 - 31	52	180 - 211	194 - 225	90 - 137

	$\dot{Q}_{\mathrm{cond}}$ kW	$\dot{Q}_{\mathrm{evap}}$ kW	$\dot{W}_{\mathrm{pmp}}$ kW	$\dot{W}_{\mathrm{expr}}$ kW	$\dot{W}_{\mathrm{net}}$ kW	η_{th} %	η_{exp} %
LT_T075P3	27.9 - 88.1	28.6 - 91.7	0.2 - 0.7	0.8 - 2.4	0.5 - 1.7	1.8 - 2.0	32 - 70
HT_T240P1	17.4 - 75.0	22.7 - 90.2	0.2 - 1.1	2.0 - 11	1.7 - 9.6	7.7 - 11	40 - 51

As expected, the evaporating pressures (p_{evap}) and temperatures (T_{evap}) in the LT-WHR system are much lower than in the HT-WHR system because of the lower temperature of the heat source. Although two different driving cycles were used as inputs for the simulations, the heat transfer rate in the evaporator ($\dot{Q}_{\mathrm{evap}}$) is very similar for both systems. To extract the same amount of heat at lower pressures and temperatures, higher mass flows ($\dot{m}_{\mathrm{pmp}}$) are required. Because of the chosen condensing pressures (p_{cond}), the condensing temperatures (T_{cond}) are almost the same for the working fluids in both systems. Because these condensing temperatures are relatively low, rejecting heat to the environment may be difficult; this issue is discussed in more in detail in Section 6.3. The absolute values of the pump power ($\dot{W}_{\mathrm{pmp}}$) in both systems are very similar. However, the pump power relative to the expander power ($\dot{W}_{\mathrm{exp}}$) is much higher for the LT-WHR system because it has lower pump efficiencies and higher mass flows. The net power ($\dot{W}_{\mathrm{net}}$) is much higher in the HT-WHR system because of its superior ability to convert the extracted heat into power, indicated by its greater thermodynamic efficiency (η_{th}). Since the HT-WHR has lower mass flows and lower expander efficiencies (η_{exp}), the higher expander power is attributable to the higher pressure ratio in the system, which results in a higher specific work.

The steady-state results were used to generate performance maps of both systems over the full operating range of the engine. These maps are shown in Fig. 6.1. As previously shown in Table 6.1, the net power output is much higher for the HT-WHR system.

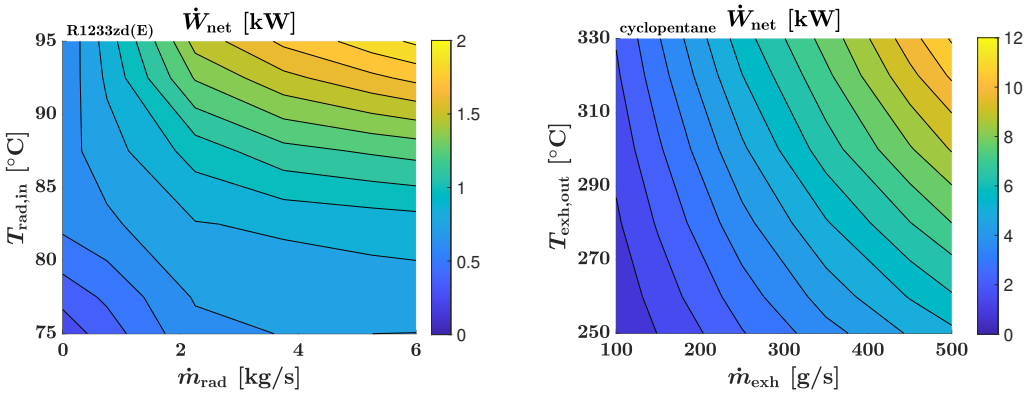

Fig. 6.1: Net power for low-temperature (left) and high-temperature (right) WHR as a function of the flow and temperature. The values at the edges were linearly extrapolated.

These performance maps were used to calculate the instantaneous power output during the driving cycle (no transient effects were taken into account). The integrated results are shown in Table 6.2. Because different driving cycles were simulated for the two systems, their performance was compared based on the relative output, which is defined as:

$$W = \frac{W}{W_{\text{eng}}} \tag{6.1}$$

The results show that the potential energy recovery achievable for the LT-WHR system is around 0.7 % of the total engine work and 3.4 % for the HT-WHR system. Additionally, the driving cycle analysis shows that in the LT-WHR system the energy consumption of the pump significantly affects the net recovered energy.

Table 6.2: Driving cycle performance as a percentage of the total brake engine power. Different driving cycles were used for high-temperature and low-temperature WHR.

	W_{eng} MJ	$W_{\text{pmp,el}}$ %	$W_{\text{exp,mech}}$ %	$W_{\text{exp,el}}$ %	$W_{\text{net}}{}^{*}$ %
LT_T075P3	408	0.41	0.98	0.15	0.73
HT_T240P1	333	0.49	3.50	0.35	3.37

* $W_{\text{net}} = W_{\text{exp,mech}} + W_{\text{exp,el}} - W_{\text{pmp,el}}$

6.2 Elevated Engine Coolant Temperatures

This section compares the operating conditions and performance of the LT-WHR system at two radiator inlet temperatures ranges of the engine coolant: the normal range (75 to 95 °C) and a range that was increased with 20 K (95 to 115 °C). The results of steady-state cycle simulations under these conditions are shown in Table 6.3, where R1233zd(E) was used as working fluid. Simulations were performed for 16 grid points spanning the full engine operating range during a driving cycle.

Table 6.3: Cycle conditions for 16 engine operating points and two coolant temperature ranges.

	$\dot{m}_{\mathrm{pmp}}$ g/s	p_{cond} bar	p_{evap} bar	T_{cond} °C	T_{evap} °C	$T_{\mathrm{exp,in}}$ °C	$T_{\mathrm{exp,out}}$ °C
LT_T075P3	145 - 440	3.0	4.4 - 7.4	51	64 - 85	70 - 88	61 - 70
LT_T095P3	258 - 1387	3.0	6.3 - 10	51	78 - 98	82 - 100	67 - 73

	$\dot{Q}_{\mathrm{cond}}$ kW	$\dot{Q}_{\mathrm{evap}}$ kW	$\dot{W}_{\mathrm{pmp}}$ kW	$\dot{W}_{\mathrm{expr}}$ kW	$\dot{W}_{\mathrm{net}}$ kW	η_{th} %	η_{exp} %
LT_T075P3	27.9 - 88.1	28.6 - 91.7	0.2 - 0.7	0.8 - 2.4	0.5 - 1.7	1.8 - 2.0	32 - 70
LT_T095P3	51.1 - 282	52.8 - 297	0.4 - 2.7	1.5 - 7.6	1.0 - 4.9	1.7 - 2.0	24 - 39

The elevated coolant temperatures enable the use of higher evaporating pressures (p_{evap}) and temperatures (T_{evap}). Additionally, more heat can be extracted from the heat source ($\dot{Q}_{\mathrm{evap}}$), leading to higher mass flows ($\dot{m}_{\mathrm{pmp}}$). Although the elevated coolant temperatures allow for a higher heat transfer rate from the engine to the cycle, they could also reduce the heat transfer rate to the engine coolant during combustion, an effect not taken into account here. In the studied system, the higher heat transfer rate was the reason for the improved performance; this is visible from the thermodynamic efficiency (η_{th}), which is almost equal for both systems. Expander efficiencies (η_{exp}) have dropped, although it must be considered that a simple empirical model for the expander was used which might not be suitable for elevated coolant temperatures. As before, these results were used to generate performance maps covering the engine operating range, as shown in Fig. 6.2. These maps show that raising the coolant temperature can lead to significant improvements in potential net power output. Raising the coolant temperature with 20 K led to three times the power output of the LT-WHR system.

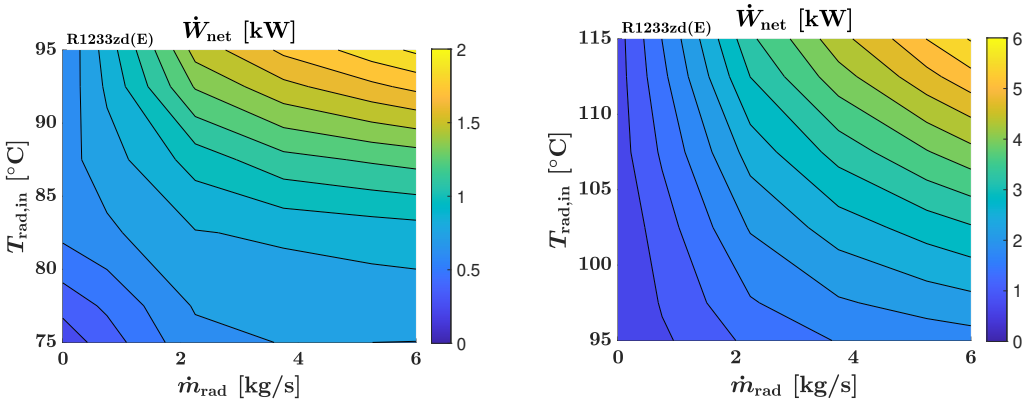

Fig. 6.2: Net shaft power as a function of the radiator mass flow and inlet temperature. The values at the edges were linearly extrapolated

These performance maps were used to calculate the instantaneous power output during the driving cycle (no transient effects were taken into account) for the normal and elevated coolant temperature ranges, giving the result shown in Fig. 6.3. The coolant temperatures in the LT_T095P3 case where 20 K higher than those in the LT_T075P3 simulations but the mass flow and total available heat were kept constant.

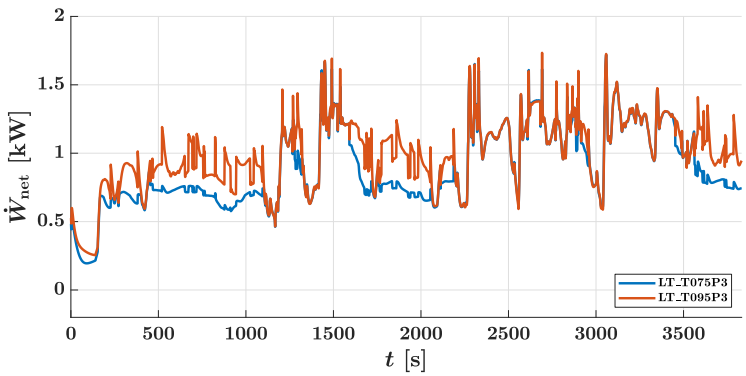

Fig. 6.3: Net shaft power over the driving cycle for the normal and elevated radiator inlet temperatures.

The net power output for the normal coolant temperatures (LT_T075P3, plotted in blue) was between 0.2 and 1.6 kW during the driving cycle. Surprisingly, the results for the elevated coolant temperatures (LT_T095P3, in orange) are only slightly better, although the potential is much higher. The reason is visible in Fig. 6.4, which shows the LT_T075P3 values of the heat rejected in the condenser ($\dot{Q}_{\text{cond}}$) and the radiator ($\dot{Q}_{\text{rad}}$), which together constitute the total rejected heat, as defined in Eq. (6.2).

$$\dot{Q}_{\text{amb}} = \dot{Q}_{\text{rad}} + \dot{Q}_{\text{cond}} \tag{6.2}$$

Since there was no coupling to the engine performance in the simulations, the total rejected heat ($\dot{Q}_{\text{amb}}$) was kept constant. Fig. 6.4 shows even at normal coolant temperatures, there was little available heat left to extract by the LT-WHR system. This means that even when the coolant temperature is raised by 20 K, not much more heat is available. Therefore, while the system with elevated temperatures has a much higher potential for energy recovery, it could not extract much more heat from the system, limiting its power output. Additionally, while a higher pressure ratio would lead to increased specific work, the efficiency of this expander is inversely proportional to the pressure ratio. Since the expander already operated at maximum speed (3000 rpm), the pressure ratio could not be decreased, leading to lower expander efficiencies for the LT_T095P3 case.

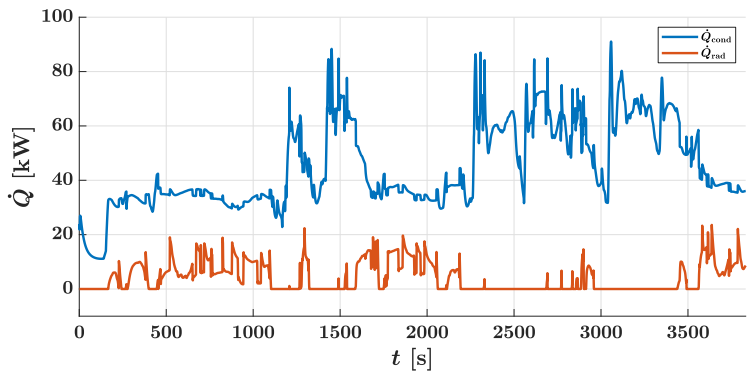

Fig. 6.4: Condenser and radiator heat transfer rates in the LT_T075P3 case during the driving cycle.

The integrated results are shown in Table 6.4, together with the total rejected heat during the driving cycle. The total recovered energy relative to the total required engine work is approximately 0.7 % in the normal coolant temperature case and 0.8 % in the elevated coolant temperature case.

Table 6.4: Driving cycle performance as a percentage of the total brake engine power.

	W_{eng} MJ	Q_{rad} MJ	Q_{cond} MJ	$W_{\text{pmp,el}}$ %	$W_{\text{exp,mech}}$ %	$W_{\text{exp,el}}$ %	$W_{\text{net}}{}^{*}$ %
LT_T075P3	408	16	172	0.41	0.98	0.15	0.73
LT_T095P3	408	0	188	0.51	1.12	0.18	0.80

* $W_{\text{net}} = W_{\text{exp,mech}} + W_{\text{exp,el}} - W_{\text{pmp,el}}$

6.3 Heat Rejection

One of the biggest challenges in automotive WHR is the heat rejection to the surroundings, where several configurations for heat rejection are possible in a truck [133]. The working fluid can be cooled by the ambient air (direct condensation), either by using the ram air or a fan. Another option is to use an intermediate fluid such as the engine coolant to condense the working fluid (indirect condensation). For the fluids examined in this chapter, only direct condensation is viable because of the low condensing temperatures of the fluids at the chosen condensing pressures. Although it can significantly affect the performance of WHR systems [109], the power consumption of the fan is not taken into account in this work. The big advantage of using the coolant for heat recovery is that no extra heat is added to the system, unlike in the case of exhaust heat recovery.

One way to enhance the heat transfer rate is by raising the condensing pressure and thereby raising the condensing temperature. To investigate this effect, the condensing pressure was raised to 2 bar for the HT-WHR system and to 5 bar for the LT-WHR system, resulting in a temperature of around 70 °C in both systems. The performance of the LT-WHR and HT-WHR systems under these conditions is shown in Table 6.5.

Table 6.5: Cycle conditions for 16 engine operating points using elevated condensing pressures.

	$\dot{m}_{pmp}$ g/s	p_{cond} bar	p_{evap} bar	T_{cond} °C	T_{evap} °C	$T_{exp,in}$ °C	$T_{exp,out}$ °C
LT_T075P5	34 - 293	5.0	4.3 - 7.6	69	63 - 86	71 - 88	72 - 79
LT_T095P5	143 - 589	5.0	7.5 - 11	69	85 - 104	89 - 107	78 - 86
HT_T240P2	35 - 139	2.0	25 - 35	72	197 - 220	209 - 233	100 - 140

	$\dot{Q}_{cond}$ kW	$\dot{Q}_{evap}$ kW	$\dot{W}_{pmp}$ kW	$\dot{W}_{expr}$ kW	$\dot{W}_{net}$ kW	η_{th} %	η_{exp} %
LT_T075P5	6.0 - 52.6	6.1 - 54.1	0.1 - 0.7	0.0 - 1.6	0.0 - 1.0	0.2 - 3.9	0 - 70
LT_T095P5	25.7 - 110	26.4 - 114	0.3 - 1.3	0.8 - 3.3	0.5 - 1.8	1.6 - 1.8	35 - 70
HT_T240P2	14.9 - 68.7	19.7 - 82.4	0.3 - 1.4	1.3 - 9.4	1.0 - 7.9	5.2 - 9.6	33 - 52

The results clearly show that increasing the condensing pressure severely reduces performance. This is especially true for the LT-WHR system, where the pressure ratios were already low and are reduced even further by raising the condensing pressure. Fig. 6.5 shows the net shaft power output of the LT-WHR system during the driving cycle for the normal (P3) and elevated condensing pressures (P5) as well as the normal (T075) and elevated coolant temperatures (T095). The biggest impact on the performance is seen for the normal coolant temperatures; at the elevated condensing pressure, the pressure ratio is so low at certain engine operating points that no power can be produced.

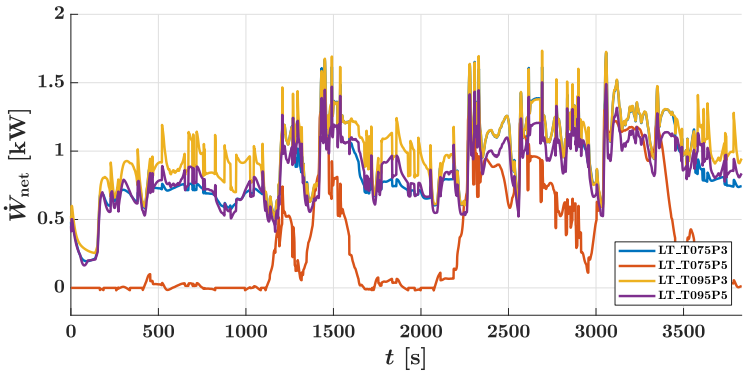

Fig. 6.5: Net power for normal and elevated condensing pressures during the driving cycle.

Fig. 6.6 shows the net shaft power output for the HT-WHR system with cyclopentane for normal and elevated condensing pressures. As a consequence of the higher condensing pressure, the net power output is significantly lower throughout the driving cycle.

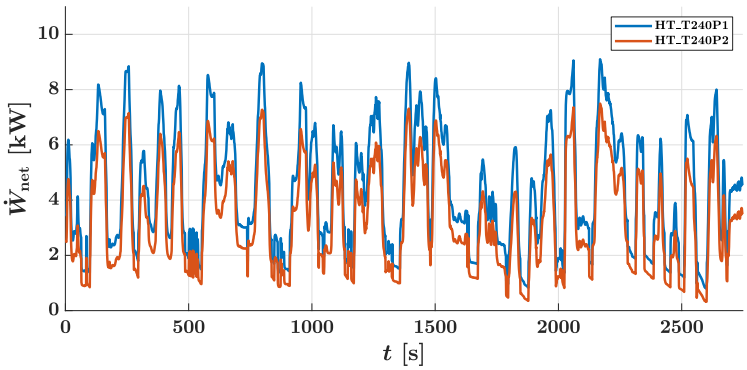

Fig. 6.6: Net power for normal and elevated condensing pressures during the driving cycle.

The integrated results for the whole driving cycle are shown in Table 6.6. Raising the condensing pressure reduced the performance of the LT_T075 system from 0.7 to 0.3 %, the LT_T095 from 0.8 to 0.6 %, and the HT_T240 from 3.4 to 2.5 % .

Table 6.6: Driving cycle performance as a percentage of the total brake engine power. Two different driving cycles were used for high-temperature and low-temperature WHR.

	W_{eng} MJ	$W_{\text{pmp,el}}$ %	$W_{\text{exp,mech}}$ %	$W_{\text{exp,el}}$ %	$W_{\text{net}}{}^{*}$ %
LT_T075P5	408	0.34	0.53	0.07	0.26
LT_T095P5	408	0.65	1.11	0.18	0.64
HT_T240P2	333	0.64	2.89	0.27	2.52

* $W_{\text{net}} = W_{\text{exp,mech}} + W_{\text{exp,el}} - W_{\text{pmp,el}}$

7 Conclusions

The overall aim of this thesis was to evaluate the thermodynamic performance achievable with four different thermodynamic cycles using the low- and high-temperature heat sources in heavy-duty engines for long haul trucks. To this end, the potential heat sources inside the engine were identified, after which preliminary simulations were performed to identify the best performing combination(s) of heat source, thermodynamic cycle, and working fluid. Experiments and more detailed modeling were then conducted to obtain more realistic evaluations of the achievable performance of the identified systems and to obtain better insights into the physical phenomena governing their behavior. The conclusions presented below draw on the experimental results and simulations to answer the four research question formulated in Section 1.3.

Potential heat sources in a heavy-duty engine

Based on an energy and exergy analysis covering the full operating range of a heavy-duty engine, four heat sources with potential for waste heat recovery (WHR) were identified. The exhaust gas recirculation cooler (EGRC) and the exhaust gases are high-temperature (HT) heat sources, while the engine coolant and the charge air cooler (CAC) are low-temperature (LT) heat sources. The engine coolant is the most promising low-temperature source because of its stable and high energy flow, although its temperature is relatively low. The exhaust gases are the high-temperature source with the greatest potential due to their high energy content and relatively high temperature.

Selection of heat sources, thermodynamic cycles, and working fluids

Four thermodynamic cycles for WHR were selected for further investigation: the organic Rankine cycle (ORC), the transcritical Rankine cycle (TRC), the trilateral flash cycle (TFC), and the organic flash cycle (OFC). Simulations of these cycles were performed for a large selection of working fluids using the four previously mentioned heat sources under representative engine operating conditions. Because the performance depends on the heat source, the operating conditions, and the chosen limitations and constraints, it is difficult to find a perfect combination of heat source, cycle, and working fluid. However, the results permit some generalization. The best performing HT heat source was the exhaust gas and the best performing cycles for HT sources were the ORC and TRC. Relative power outputs of up to 5 % were achieved using these cycles to recover heat from the exhaust gas. Although the ORC and TRC delivered comparable outputs in this case, the ORC was favored because it is a more established technology and has lower cycle pressures. The ORC also achieved the best performance for the LT heat sources with relative power outputs of up to 1.5 %. Generally, the best performance was obtained with acetone, benzene, cyclopentane, ethanol, or methanol as the working fluid. Good non-flammable and non-toxic working fluids were R1233zd(E), MM, and Novec649, although they achieved a lower power output.

The heat sources were also combined in series using a single loop WHR system. Two combinations were considered, one including all four heat sources (CAC-Coolant-EGRC-Exhaust) and one without the engine coolant (CAC-EGRC-Exhaust). The best performing cycles and working fluids in these simulations were in line with the previously presented results. The peak relative power output for the CAC-Coolant-EGRC-Exhaust system was around 7 %, while that for the CAC-EGRC-Exhaust system was around 8 %. Simulations of a dual-loop ORC WHR system were also performed for a transient driving cycle (WHTC), using cyclopentane for coolant heat recovery and methanol for exhaust heat recovery. This system was predicted to reduce fuel consumption by up to 9 %.

Performance evaluation of LT- and HT-WHR systems

To support and validate the results from the cycle simulations, two experimental setups were constructed: a high-temperature setup consisting of a Rankine cycle (RC) with water that was used to recover the heat from the exhaust gases of a heavy-duty engine, and a low-temperature setup consisting of an ORC coupled to a heavy-duty engine that recovered heat from the engine coolant using R1233zd(E) as the working fluid. In addition to providing valuable insights into WHR performance, experimental measurements obtained with these setups were used to calibrate and validate detailed cycle component models. The outputs of the experimental WHR systems were lower than the previously predicted potential from the simulations, mainly because of the relatively low expander efficiencies and system limitations that made it impossible to extract all of the available heat. The detailed component models were used to simulate typical conditions during a driving cycle. These simulations indicated that the LT-WHR system could recover 0.73 % of the total required engine work, while the HT-WHR achieved 3.37 %.

Although the LT-WHR system performed considerably less than the HT-WHR system, there are some advantages to using the engine coolant as a heat source. First, its relatively low temperature means that the cycle temperatures and corresponding pressures are low. This affects the choice for components and materials, potentially reducing the associated costs. Another advantage is that the recovered heat is not added to the cooling load of the truck (as is the case for exhaust heat recovery), although the heat must be rejected at lower temperatures. The range of temperatures and mass flows in the cycle is also limited, which could be an advantage for control of the system.

Performance considerations and improvements

The performance of any thermodynamic cycle depends on the efficiencies of its components, and the experimental results showed that the studied systems were no exception to this rule. Low expander efficiencies led to low expander shaft power outputs and low pump efficiencies could significantly reduce the net power output. While good efficiencies are certainly important for HT-WHR systems, they are especially important for LT-WHR systems because their lower pressures and temperatures mean that even small losses

can lead to large performance penalties. And, since the pump power is such a large portion of the expander power, it is important to select both an efficient expander and an efficient pump. This means that especially for LT-WHR systems, careful considerations are important during the design phase related to component efficiencies and dimensions along with the dimensioning of the piping system and the suction pressure at the inlet of the pump. Other important considerations for automotive WHR include costs and the packaging. While it is possible to evaluate these other considerations using a techno-economic optimization, the focus of this work was on thermodynamic performance of the systems and, therefore, this was not included in the thesis.

Rejecting the heat to the surroundings may be more important for the performance of WHR systems than extracting the heat from the heat source, especially for LT-WHR systems. When using low condensing temperatures, the only feasible option for heat rejection is direct condensation, i.e. rejecting the heat using the ram air of the vehicle or the air flow from an (additional) external fan. Increasing the condensing pressure in the cycle leads to higher condensing temperatures and thus enhances heat transfer, albeit at the cost of a lower pressure ratio and thus reduced cycle performance. Simulations showed that during a driving cycle under normal engine operating conditions, increasing the condensing temperature from 50 to 70 °C reduced the relative recovered energy from 0.7 to 0.3 % for the LT-WHR system and from 3.37 to 2.5 % for the HT-WHR system.

The only feasible way of achieving efficient low-temperature waste heat recovery is to increase the engine coolant temperature. Elevated coolant temperatures allow for higher pressures and temperatures in the cycle, improving the specific work. Higher temperatures could enhance heat extraction and thus increase power output, while raising the evaporating pressure in the cycle could make it possible to increase the condensing pressure, which is important for heat rejection. Although simulations based on the experimental LT-WHR setup showed that raising the coolant temperature by 20 K caused only minor improvements in the relative recovered energy (from 0.73 % to 0.80 %), this was mainly due to limitations of the studied system. Other steady-state cycle simulations over a transient driving cycle have shown that recovering the heat from the engine coolant at a temperature of 140 °C could reduce the fuel consumption by almost 4.5 %, whereas only a 0.5 % reduction was predicted for an engine coolant temperature of 80 °C. Experimental results reported in the same publications showed that the indicated efficiency of the engine was not significantly changed by raising the coolant temperature; an important conclusion if the efficiency of the whole system is taken into account.

8 Future Outlook

It is difficult to say what the future role of waste heat recovery systems for heavy-duty engines may be. This is not because their potential benefits are in question but because of the uncertain role of the internal combustion engine in future transportation. Projections suggest that by 2070, the dominant energy sources for heavy-duty transportation will be fuel cells or batteries [5]. However, apart from the difficulty of predicting long-term technological developments, these same projections suggest that in 2050 the majority of trucks will still be propelled by an internal combustion engine. Therefore, to reduce the impact of heavy-duty transportation on CO_2 emissions, it is crucial to improve the engine efficiency. Waste heat recovery is a powerful technology for this purpose because among the available emissions reduction technologies, it offers some of the highest possible reductions in fuel consumption. Based on the previously presented conclusions and underlying research, a number of suggestions for future research can be formulated:

- The experimental setups and detailed simulation models for low-temperature and high-temperature were developed separately in this work. However, to realize the full potential of WHR, it may be better to combine these two systems into one. Detailed dynamic simulation models could be used to develop control strategies for such a system and experiments could then be performed to validate these strategies and evaluate their performance. As an alternative to the standard Diesel engine, a heavy-duty engine with hydrogen combustion could be used as the heat source.

- The potential benefits of elevated coolant temperatures could be further explored by performing experiments with a combined engine and WHR system that permits coolant temperatures above 150 °C. The full system efficiency (i.e. the efficiency of both the engine and the WHR system) should be evaluated. In this study, the lubricant oil of the engine can be taken as an additional heat source and studied for its potential for WHR.

- Another possibility is to study not only the engine and WHR system as separate systems, but as a system integrated in a hybrid electric truck. The goal would be to optimize the thermal-electric system as a whole, including the air-conditioning system, electric generators and batteries, engine cooling systems, waste heat recovery systems, and so on. While this would be challenging (especially for academic research) because of the massive scope and the availability of data and equipment, a full system approach has the potential to deliver the greatest performance gains possible.

- Because of the importance of heat rejection during driving, a detailed study on radiator performance could be highly beneficial. Topics could include the effect and improvement of heat transfer characteristics during condensation as well as fan power consumption optimization during typical driving conditions.

References

[1] IPCC, *Climate Change 2014: Synthesis Report. Contribution of Working Groups I, II and III to the Fifth Assessment Report of the Intergovernmental Panel on Climate Change*. IPCC, 2014.

[2] H. Ritchie and M. Roser, "Co2 and greenhouse gas emissions," *Our World in Data*, 2017. Accessed: 2020-12-31.

[3] European Environment Agency (EEA), "National emissions reported to the UNFCCC and to the EU Greenhouse Gas Monitoring Mechanism 2017." `https://www.eea.europa.eu/ds_resolveuid/a6e1bc85fbed4989b0fd6739c443739a`. Accessed: 2020-12-15.

[4] Environmental Protection Agency (EPA), "Fast facts U.S. Transportation Sector Greenhouse Gas Emissions 1990 – 2018," 2020.

[5] International Energy Agency, *Energy Technology Perspectives 2020*. 2020.

[6] ICCT, "CO2 emissions and fuel consumption standards for heavy-duty vehicles in the European Union," 2018.

[7] European Parliament, Council of the European Union, "Regulation (EU) 2019/1242 - Setting CO2 emission performance standards for new heavy-duty vehicles," 2019.

[8] W. Jevons, *The Coal Question: An Inquiry Concerning the Progress of the Nation, and the Probable Exhaustion of our Coal-mines*. Macmillan, 1865.

[9] European Environment Agency (EEA), "EEA greenhouse gas - data viewer. CO2, Heavy duty trucks and buses, Emissions - EU-27, 2020." `https://www.eea.europa.eu/data-and-maps/data/data-viewers/greenhouse-gases-viewer`. Accessed: 2020-01-02.

[10] G. Singh, L. Breton, L. Gravel, and K. Howden, "Overview of the VTO Advanced Combustion Engine R&D Program," *U.S. Department of Energy (DOE) Presentation*, 2016.

[11] Environmental Protection Agency (EPA), "Inventory of U.S. Greenhouse Gas Emissions and Sinks," 2020.

[12] Z. Su, M. Zhang, P. Xu, Z. Zhao, Z. Wang, H. Huang, and T. Ouyang, "Opportunities and strategies for multigrade waste heat utilization in various industries: A recent review," *Energy Conversion and Management*, vol. 229, feb 2021.

[13] P. Colonna, E. Casati, C. Trapp, T. Mathijssen, J. Larjola, T. Turunen-Saaresti, and A. Uusitalo, "ORC Power Systems: From the Concept to Current Technology, Applications, and an Outlook to the Future," *Journal of Engineering for Gas Turbines and Power*, vol. 137, no. 10, 2015.

[14] P. S. Patel and E. F. Doyle, "Compounding the Truck Diesel Engine with an Organic Rankine-Cycle System," in *SAE Technical Paper Series*, vol. 1, 1976.

[15] A. Joshi, "Review of Vehicle Engine Efficiency and Emissions," *SAE Technical Paper 2020-01-0352*, 2020.

[16] S. Lion, C. N. Michos, I. Vlaskos, C. Rouaud, and R. Taccani, "A review of waste heat recovery and Organic Rankine Cycles (ORC) in on-off highway vehicle Heavy Duty Diesel Engine applications," *Renewable and Sustainable Energy Reviews*, vol. 79, 2017.

[17] B. Xu, D. Rathod, A. Yebi, Z. Filipi, S. Onori, and M. Hoffman, "A comprehensive review of organic rankine cycle waste heat recovery systems in heavy-duty diesel engine applications," *Renewable and Sustainable Energy Reviews*, vol. 107, 2019.

[18] T. Endo, S. Kawajiri, Y. Kojima, K. Takahashi, T. Baba, S. Ibaraki, T. Takahashi, and M. Shinohara, "Study on Maximizing Exergy in Automotive Engines," *SAE Transactions: Journal of Engines*, vol. 116, 2007.

[19] R. Freymann, W. Strobl, and A. Obieglo, "The turbosteamer: A system introducing the principle of cogeneration in automotive applications," *MTZ worldwide*, vol. 69, no. 5, 2008.

[20] R. Freymann, J. Ringler, M. Seifert, and T. Horst, "The Second Generation Turbosteamer," *MTZ worldwide*, vol. 73, feb 2012.

[21] A. Carstensen, A. Horn, J. Klammer, and J. Gockel, "Waste Heat Recovery in Passenger Cars and Trucks," *MTZ worldwide*, vol. 80, no. 4, 2019.

[22] F. Ekström, "A mild hybrid SIDI turbo passenger car engine with Rankine waste heat recovery," *SAE Technical Paper 2019-24-0194*, 2019.

[23] J. Rijpkema, F. Ekström, K. Munch, and S. B. Andersson, "Experimental results of a waste heat recovery system with ethanol using the exhaust gases of a light-duty engine," in *Proceedings of the 5th International Seminar on ORC Power Systems*, 2019.

[24] J. O'Connor, M. Borz, D. Ruth, J. Han, C. Paul, A. Imren, D. Haworth, J. Martin, A. Boehman, J. Li, K. Heffelfinger, S. McLaughlin, R. Morton, A. Andersson, and A. Karlsson, "Optimization of an Advanced Combustion Strategy Towards 55% BTE for the Volvo SuperTruck Program," *SAE International Journal of Engines*, vol. 10, no. 3, 2017.

[25] S. Thantla, J. Fridh, A. Erlandsson, and J. Aspfors, "Performance Analysis of Volumetric Expanders in Heavy-Duty Truck Waste Heat Recovery," *SAE Technical Paper 2019-01-2266*, 2019.

[26] F. Bettoja, A. Perosino, V. Lemort, L. Guillaume, T. Reiche, and T. Wagner, "NoWaste: Waste Heat Re-use for Greener Truck," *Transportation Research Procedia*, vol. 14, 2016.

[27] J. Heywood, *Internal Combustion Engine Fundamentals*. McGraw-Hill, 1988.

[28] R. Van Basshuysen and F. Schaefer, *Internal Combustion Engine Handbook, 2nd English Edition*. SAE International, 2016.

[29] K. Mollenhauer, K. Johnson, and H. Tschöke, *Handbook of Diesel Engines*. Springer Berlin Heidelberg, 2010.

[30] "DieselNet: Emission standards - United States)." `https://www.dieselnet.com/standards/cycles/esc.php`. Accessed: 2021-02-05.

[31] "DieselNet: Emission test cycles - European Stationary Cycle (ESC)." `https://dieselnet.com/standards/us/index.php`. Accessed: 2021-01-04.

[32] S. Edwards, J. Eitel, E. Pantow, P. Geskes, R. Lutz, and J. Tepas, "Waste Heat Recovery: The Next Challenge for Commercial Vehicle Thermomanagement," *SAE International Journal of Commercial Vehicles*, vol. 5, no. 1, 2012.

[33] A. García, J. Monsalve-Serrano, S. Martinez-Boggio, P. Gaillard, O. Poussin, and A. A. Amer, "Dual fuel combustion and hybrid electric powertrains as potential solution to achieve 2025 emissions targets in medium duty trucks sector," *Energy Conversion and Management*, vol. 224, 2020.

[34] F. Hofer, W. Gruber, B. Raser, and H. Theißl, "Technology Scenarios for Fulfilling Future EU CO2 Targets for Commercial Vehicle Fleets," *ATZheavy duty worldwide*, vol. 13, no. 1, 2020.

[35] S. Pischinger, J. Schaub, F. Aubeck, and D. van der Put, "Powertrain Concepts for Heavy-duty Applications to Meet 2030 CO2 Regulations," *ATZheavy duty worldwide*, vol. 13, no. 3, 2020.

[36] A. Smallbone, B. Jia, P. Atkins, and A. P. Roskilly, "The impact of disruptive powertrain technologies on energy consumption and carbon dioxide emissions from heavy-duty vehicles," *Energy Conversion and Management: X*, vol. 6, 2020.

[37] K. Eichler, Y. Jeihouni, and C. Ritterskamp, "Fuel Economy Benefits for Commercial Diesel Engines with Waste Heat Recovery," *SAE International Journal of Commercial Vehicles*, vol. 8, 2015.

[38] H. Aghaali and H.-E. Ångström, "A review of turbocompounding as a waste heat recovery system for internal combustion engines," *Renewable and Sustainable Energy Reviews*, vol. 49, 2015.

[39] E. Garofalo, M. Bevione, L. Cecchini, F. Mattiussi, and A. Chiolerio, "Waste Heat to Power: Technologies, Current Applications, and Future Potential," *Energy Technology*, vol. 8, 2020.

[40] G. Latz, *Waste Heat Recovery from Combustion Engines based on the Rankine Cycle*. PhD thesis, 2016.

[41] R. Saidur, M. Rezaei, W. Muzammil, M. Hassan, S. Paria, and M. Hasanuzzaman, "Technologies to recover exhaust heat from internal combustion engines," *Renewable and Sustainable Energy Reviews*, vol. 16, 2012.

[42] N. Espinosa, M. Lazard, L. Aixala, and H. Scherrer, "Modeling a Thermoelectric Generator Applied to Diesel Automotive Heat Recovery," *Journal of Electronic Materials*, vol. 39, no. 9, 2010.

[43] A. E. Risseh, H.-P. Nee, O. Erlandsson, K. Brinkfeldt, A. Contet, F. Frobenius lng, G. Gaiser, A. Saramat, T. Skare, S. Nee, and J. Dellrud, "Design of a Thermoelectric Generator for Waste Heat Recovery Application on a Drivable Heavy Duty Vehicle," *SAE International Journal of Commercial Vehicles*, vol. 10, 2017.

[44] M. He, E. Wang, Y. Zhang, W. Zhang, F. Zhang, and C. Zhao, "Performance analysis of a multilayer thermoelectric generator for exhaust heat recovery of a heavy-duty diesel engine," *Applied Energy*, vol. 274, 2020.

[45] M. A. G. Timmer, K. de Blok, and T. H. van der Meer, "Review on the conversion of thermoacoustic power into electricity," *The Journal of the Acoustical Society of America*, vol. 143, 2018.

[46] W. Bou Nader, J. Chamoun, and C. Dumand, "Thermoacoustic engine as waste heat recovery system on extended range hybrid electric vehicles," *Energy Conversion and Management*, vol. 215, 2020.

[47] J. Zhou, M. Karlsson, and M. Abom, "Study of thermoacoustic engine for automotive exhaust waste heat recovery," *SAE Technical Papers*, 2019.

[48] J. Zhou, M. Karlsson, and M. Abom, "Designing Regenerators of Thermoacoustic Engines for Automotive Waste Heat Recovery," in *SAE Technical Papers*, vol. 2020-April, 2020.

[49] J. Szargut, D. Morris, and F. Steward, *Exergy analysis of thermal, chemical, and metallurgical processes*. Hemisphere, 1988.

[50] J. Rijpkema, S. Andersson, and K. Munch, "Thermodynamic Cycle and Working Fluid Selection for Waste Heat Recovery in a Heavy Duty Diesel Engine," *SAE Technical Paper 2018-01-1371*, 2018.

[51] W. B. Nader, C. Mansour, C. Dumand, and M. Nemer, "Brayton cycles as waste heat recovery systems on series hybrid electric vehicles," *Energy Conversion and Management*, vol. 168, 2018.

[52] D. Di Battista, F. Fatigati, R. Carapellucci, and R. Cipollone, "Inverted Brayton Cycle for waste heat recovery in reciprocating internal combustion engines," *Applied Energy*, vol. 253, 2019.

[53] A. Uusitalo, A. Ameli, and T. Turunen-Saaresti, "Thermodynamic and turbomachinery design analysis of supercritical Brayton cycles for exhaust gas heat recovery," *Energy*, vol. 167, 2019.

[54] M. Güven, H. Bedir, and G. Anlas, "Optimization and application of Stirling engine for waste heat recovery from a heavy-duty truck engine," *Energy Conversion and Management*, vol. 180, 2019.

[55] K. Wang, S. R. Sanders, S. Dubey, F. H. Choo, and F. Duan, "Stirling cycle engines for recovering low and moderate temperature heat: A review," *Renewable and Sustainable Energy Reviews*, vol. 62, 2016.

[56] A. I. Kalina, "Combined cycle and waste heat recovery power systems based on a novel thermodynamic energy cycle utilizing low-temperature heat for power generation," *Am. Soc. Mech. Eng., (Pap.); (United States)*, 1983.

[57] U. Larsen, T.-V. Nguyen, T. Knudsen, and F. Haglind, "System analysis and optimisation of a Kalina split-cycle for waste heat recovery on large marine diesel engines," *Energy*, vol. 64, 2014.

[58] S. Zhu, K. Zhang, and K. Deng, "A review of waste heat recovery from the marine engine with highly efficient bottoming power cycles," *Renewable and Sustainable Energy Reviews*, vol. 120, 2020.

[59] F. Mohammadkhani and M. Yari, "A 0D model for diesel engine simulation and employing a transcritical dual loop Organic Rankine Cycle (ORC) for waste heat recovery from its exhaust and coolant: Thermodynamic and economic analysis," *Applied Thermal Engineering*, vol. 150, 2019.

[60] A. Mahmoudi, M. Fazli, and M. R. Morad, "A recent review of waste heat recovery by Organic Rankine Cycle," *Applied Thermal Engineering*, vol. 143, 2018.

[61] A. T. Hoang, "Waste heat recovery from diesel engines based on Organic Rankine Cycle," *Applied Energy*, vol. 231, 2018.

[62] M. E. Mondejar, J. G. Andreasen, L. Pierobon, U. Larsen, M. Thern, and F. Haglind, "A review of the use of organic Rankine cycle power systems for maritime applications," *Renewable and Sustainable Energy Reviews*, vol. 91, 2018.

[63] C. Sprouse and C. Depcik, "Review of organic Rankine cycles for internal combustion engine exhaust waste heat recovery," *Applied Thermal Engineering*, vol. 51, 2013.

[64] T. Wang, Y. Zhang, Z. Peng, and G. Shu, "A review of researches on thermal exhaust heat recovery with Rankine cycle," *Renewable and Sustainable Energy Reviews*, vol. 15, 2011.

[65] X. Li, J. Song, G. Yu, Y. Liang, H. Tian, G. Shu, and C. N. Markides, "Organic Rankine cycle systems for engine waste-heat recovery: Heat exchanger design in space-constrained applications," *Energy Conversion and Management*, vol. 199, 2019.

[66] L. Shi, G. Shu, H. Tian, G. Huang, T. Chen, X. Li, and D. Li, "Experimental comparison between four CO 2 -based transcritical Rankine cycle (CTRC) systems for engine waste heat recovery," *Energy Conversion and Management*, vol. 150, 2017.

[67] I. Smith, N. Stosic, and A. Kovacevic, "Power recovery from low cost two-phase expanders," in *Transactions-Geothermal Resources Council*, 2001.

[68] A. Baccioli and M. Antonelli, "Organic Flash Cycles: Off-design behavior and control strategies of two different cycle architectures for Waste Heat Recovery applications," *Energy Conversion and Management*, vol. 157, 2018.

[69] B. C. Choi and Y. M. Kim, "Thermodynamic analysis of a dual loop heat recovery system with trilateral cycle applied to exhaust gases of internal combustion engine for propulsion of the 6800 TEU container ship," *Energy*, vol. 58, 2013.

[70] R. DiPippo, *Geothermal Power Plants - Principles, Applications, Case Studies and Environmental Impact (4th Edition)*. Elsevier, 2016.

[71] T. Ho, S. S. Mao, and R. Greif, "Comparison of the Organic Flash Cycle (OFC) to other advanced vapor cycles for intermediate and high temperature waste heat reclamation and solar thermal energy," *Energy*, vol. 42, no. 1, 2012.

[72] T. Ho, S. S. Mao, and R. Greif, "Increased power production through enhancements to the Organic Flash Cycle (OFC)," *Energy*, vol. 45, 2012.

[73] F. Willems, F. Kupper, G. Rascanu, and E. Feru, "Integrated Energy and Emission Management for Diesel Engines with Waste Heat Recovery Using Dynamic Models," *Oil & Gas Science and Technology Revue d'IFP Energies nouvelles*, vol. 70, 2015.

[74] D. T. Hountalas, G. C. Mavropoulos, C. Katsanos, and W. Knecht, "Improvement of bottoming cycle efficiency and heat rejection for HD truck applications by utilization of EGR and CAC heat," *Energy Conversion and Management*, vol. 53, no. 1, 2012.

[75] G. Cavazzini, F. Giacomel, A. Benato, and S. Bari, "Influence of the Fluid-Dynamic Properties of Organic Fluids on Pump Performance," in *5th International Seminar on ORC power Systems*, 2019.

[76] G. Carraro, P. Pallis, A. D. Leontaritis, S. Karellas, P. Vourliotis, S. Rech, and A. Lazzaretto, "Experimental performance evaluation of a multi-diaphragm pump of a micro-ORC system," *Energy Procedia*, vol. 129, 2017.

[77] L. Guillaume, A. Legros, A. Desideri, and V. Lemort, "Performance of a radial-inflow turbine integrated in an ORC system and designed for a WHR on truck application: An experimental comparison between R245fa and R1233zd," *Applied Energy*, vol. 186, 2017.

[78] S. Quoilin, M. V. D. Broek, S. Declaye, P. Dewallef, and V. Lemort, "Techno-economic survey of organic rankine cycle (ORC) systems," *Renewable and Sustainable Energy Reviews*, vol. 22, 2013.

[79] M. Hatami, D. Ganji, and M. Gorji-Bandpy, "A review of different heat exchangers designs for increasing the diesel exhaust waste heat recovery," *Renewable and Sustainable Energy Reviews*, vol. 37, 2014.

[80] D. Di Battista, M. Di Bartolomeo, C. Villante, and R. Cipollone, "A Model Approach to the Sizing of an ORC Unit for WHR in Transportation Sector," *SAE International Journal of Commercial Vehicles*, vol. 10, no. 2, 2017.

[81] S. Amicabile, J. I. Lee, and D. Kum, "A comprehensive design methodology of organic Rankine cycles for the waste heat recovery of automotive heavy-duty diesel engines," *Applied Thermal Engineering*, vol. 87, 2015.

[82] J. Bao and L. Zhao, "A review of working fluid and expander selections for organic Rankine cycle," *Renewable and Sustainable Energy Reviews*, vol. 24, 2013.

[83] Y. Zhao, G. Liu, L. Li, Q. Yang, B. Tang, and Y. Liu, "Expansion devices for organic Rankine cycle (ORC) using in low temperature heat recovery: A review," *Energy Conversion and Management*, vol. 199, 2019.

[84] H. Chen, D. Y. Goswami, and E. K. Stefanakos, "A Review of Thermodynamic Cycles and Working Fluids for the Conversion of Low-grade Heat," *Renewable and Sustainable Energy Reviews*, vol. 14, no. 9, 2010.

[85] C. Invernizzi, P. Iora, and P. Silva, "Bottoming micro-Rankine cycles for micro-gas turbines," *Applied Thermal Engineering*, vol. 27, no. 1, 2007.

[86] E. Macchi and M. Astolfi, *Organic Rankine Cycle (ORC) Power Systems: Technologies and Applications*. Elsevier Science, 2016.

[87] R. Scaccabarozzi, M. Tavano, C. M. Invernizzi, and E. Martelli, "Comparison of working fluids and cycle optimization for heat recovery ORCs from large internal combustion engines," *Energy*, vol. 158, 2018.

[88] X. Dai, L. Shi, Q. An, and W. Qian, "Screening of hydrocarbons as supercritical ORCs working fluids by thermal stability," *Energy Conversion and Management*, vol. 126, 2016.

[89] S. Quoilin, *Sustainable Energy Conversion Through the Use of Organic Rankine Cycles for Waste Heat Recovery and Solar Applications.* PhD thesis, 2011.

[90] M. Imran, F. Haglind, V. Lemort, and A. Meroni, "Optimization of organic rankine cycle power systems for waste heat recovery on heavy-duty vehicles considering the performance, cost, mass and volume of the system," *Energy*, vol. 180, 2019.

[91] G. Latz, S. Andersson, and K. Munch, "Comparison of Working Fluids in Both Subcritical and Supercritical Rankine Cycles for Waste-Heat Recovery Systems in Heavy-Duty Vehicles," *SAE Technical Paper 2012-01-1200*, 2012.

[92] I. H. Bell, J. Wronski, S. Quoilin, and V. Lemort, "Pure and pseudo-pure fluid thermophysical property evaluation and the open-source thermophysical property library CoolProp," *Industrial and Engineering Chemistry Research*, vol. 53, no. 6, 2014.

[93] E. W. Lemmon, M. L. Huber, and M. O. McLinden, *NIST Standard Reference Database 23: Reference Fluid Thermodynamic and Transport Properties - REFPROP*. National Institute of Standards and Technology, Standard Reference Data Program, Gaithersburg, 9.1 ed., 2013.

[94] M. Preißinger, J. A. Schwöbel, A. Klamt, and D. Brüggemann, "Multi-criteria evaluation of several million working fluids for waste heat recovery by means of Organic Rankine Cycle in passenger cars and heavy-duty trucks," *Applied Energy*, 2017.

[95] A. Bardow, K. Steur, and J. Gross, "Continuous-Molecular Targeting for Integrated Solvent and Process Design," *Industrial & Engineering Chemistry Research*, vol. 49, 2010.

[96] M. Lampe, M. Stavrou, H. M. Bücker, J. Gross, and A. Bardow, "Simultaneous Optimization of Working Fluid and Process for Organic Rankine Cycles Using PC-SAFT," *Industrial & Engineering Chemistry Research*, vol. 53, 2014.

[97] A. I. Papadopoulos, M. Stijepovic, and P. Linke, "On the systematic design and selection of optimal working fluids for Organic Rankine Cycles," *Applied Thermal Engineering*, vol. 30, 2010.

[98] J. Schilling, K. Eichler, B. Kölsch, S. Pischinger, and A. Bardow, "Integrated design of working fluid and organic Rankine cycle utilizing transient exhaust gases of heavy-duty vehicles," *Applied Energy*, vol. 255, 2019.

[99] T. Furukawa, M. Nakamura, K. Machida, and K. Shimokawa, "A Study of the Rankine Cycle Generating System for Heavy Duty HV Trucks," apr 2014.

[100] V. Vodicka, L. Guillaume, J. Mascuch, and V. Lemort, "Testing and Modeling a Vane Expander used in an ORC Working With Hexamethyldisiloxane (MM)," in *Proceedings of the 3rd International Seminar on ORC Power Systems. ASME ORC 2015*, 2015.

[101] L. Guillaume and V. Lemort, "Comparison of different ORC typologies for heavy-duty trucks by means of a thermo-economic optimization," *Energy*, vol. 182, 2019.

[102] K. Yang, H. Zhang, S. Song, J. Zhang, Y. Wu, Y. Zhang, H. Wang, Y. Chang, and C. Bei, "Performance Analysis of the Vehicle Diesel Engine-ORC Combined System Based on a Screw Expander," *Energies*, vol. 7, 2014.

[103] D. Seher, T. Lengenfelder, J. Gerhardt, N. Eisenmenger, M. Hackner, and I. Krinn, "Waste Heat Recovery for Commercial Vehicles with a Rankine Process," *21 st Aachen Colloquium Automobile and Engine Technology*, 2012.

[104] Y.-Q. Zhang, Y.-T. Wu, G.-D. Xia, C.-F. Ma, W.-N. Ji, S.-W. Liu, K. Yang, and F.-B. Yang, "Development and experimental study on organic Rankine cycle system with single-screw expander for waste heat recovery from exhaust of diesel engine," *Energy*, vol. 77, 2014.

[105] F. Alshammari and A. Pesyridis, "Experimental study of organic Rankine cycle system and expander performance for heavy-duty diesel engine," *Energy Conversion and Management*, vol. 199, 2019.

[106] P. Smague, P. Leduc, and A. Leroux, "Development of a 48V ORC turbo-pump for waste heat recovery in the coolant of light duty and commercial vehicles," in *Proceedings of the 5th International Seminar on ORC Power Systems*, 2019.

[107] NI, *LabVIEW, Version 2019 SP1*, 2019.

[108] M. Imran, R. Pili, M. Usman, and F. Haglind, "Dynamic modeling and control strategies of organic Rankine cycle systems: Methods and challenges," *Applied Energy*, vol. 276, 2020.

[109] F. Galuppo, T. Reiche, V. Lemort, P. Dufour, and M. Nadri, "Organic Rankine Cycle based waste heat recovery modeling and control of the low pressure side using direct condensation and dedicated fans," *Energy*, 2020.

[110] M. C. Esposito, N. Pompini, A. Gambarotta, V. Chandrasekaran, J. Zhou, and M. Canova, "Nonlinear model predictive control of an Organic Rankine Cycle for exhaust waste heat recovery in automotive engines," *IFAC-PapersOnLine*, vol. 28, 2015.

[111] M. Hebeler, P. Ebeling, W. Tegethoff, and J. Köhler, "Exhaust Waste Heat Recovery for Intercity Bus Climatisation Using Rankine Technology with Focus on Topology Design," in *Proceedings of the 5th International Seminar on ORC Power Systems*, pp. 1–8, 2019.

[112] E. Feru, B. de Jager, F. Willems, and M. Steinbuch, "Two-phase plate-fin heat exchanger modeling for waste heat recovery systems in diesel engines," *Applied Energy*, vol. 133, 2014.

[113] A. Desideri, B. Dechesne, J. Wronski, M. van den Broek, S. Gusev, V. Lemort, and S. Quoilin, "Comparison of Moving Boundary and Finite-Volume Heat Exchanger Models in the Modelica Language," *Energies*, vol. 9, 2016.

[114] F. Alshammari, A. Pesyridis, A. Karvountzis-Kontakiotis, B. Franchetti, and Y. Pesmazoglou, "Experimental study of a small scale organic Rankine cycle waste heat recovery system for a heavy duty diesel engine with focus on the radial inflow turbine expander performance," *Applied Energy*, vol. 215, 2018.

[115] M. Imran, M. Usman, B.-S. Park, and D.-H. Lee, "Volumetric expanders for low grade heat and waste heat recovery applications," *Renewable and Sustainable Energy Reviews*, 2016.

[116] V. Lemort, L. Guillaume, L. A., S. Declaye, and S. Quoilin, "A comparison of piston, screw and scroll expanders for small scale Rankine cycle systems," *Proceedings of the 3rd international conference on microgeneration and related technologies.*, 2013.

[117] S. Declaye, S. Quoilin, L. Guillaume, and V. Lemort, "Experimental study on an open-drive scroll expander integrated into an ORC (Organic Rankine Cycle) system with R245fa as working fluid," *Energy*, vol. 55, 2013.

[118] V. Lemort, *Contribution To the Characterization of Scroll Machines in Compressor and Expander Modes.* PhD thesis, 2008.

[119] D. Ziviani, N. A. James, F. A. Accorsi, J. E. Braun, and E. A. Groll, "Experimental and numerical analyses of a 5 kWe oil-free open-drive scroll expander for small-scale organic Rankine cycle (ORC) applications," *Applied Energy*, vol. 230, 2018.

[120] V. Vodicka, V. Novotny, Z. Zeleny, J. Mascuch, and M. Kolovratnik, "Theoretical and experimental investigations on the radial and axial leakages within a rotary vane expander," *Energy*, vol. 189, 2019.

[121] A. Rubino, S. Vitale, P. Colonna, and M. Pini, "Fully-turbulent adjoint method for the unsteady shape optimization of multi-row turbomachinery," *Aerospace Science and Technology*, vol. 106, 2020.

[122] *Modelica language specification, Version 3.3*, 2012.

[123] *Dymola, Version 2016 FD01*, 2016.

[124] *Python language reference, Version 2.7.13*, 2017.

[125] MathWorks, *MATLAB, Version R2019a*, 2019.

[126] R. Webb and K. Nae-Hyun, *Principles of Enhanced Heat Transfer.* CRC Press, 2005.

[127] Y. Glavatskaya, P. Podevin, V. Lemort, O. Shonda, and G. Descombes, "Reciprocating Expander for an Exhaust Heat Recovery Rankine Cycle for a Passenger Car Application," *Energies*, vol. 5, no. 6, 2012.

[128] J.-F. Oudkerk, *Contribution to the Characterization of Piston Expanders for their Use in Small-Scale Power Production Systems*. PhD thesis, 2016.

[129] F. White, *Fluid Mechanics*. McGraw-Hill, 2009.

[130] A. F. Mills, *Basic Heat & Mass Transfer*. Prentice Hall, 1999.

[131] A. Giuffrida, "Modelling the performance of a scroll expander for small organic Rankine cycles when changing the working fluid," *Applied Thermal Engineering*, vol. 70, no. 1, 2014.

[132] M. A. Ancona, M. Bianchi, L. Branchini, A. D. Pascale, F. Melino, S. Ottaviano, and A. Peretto, "Performance Prediction and Design Optimization of a kW-size Reciprocating Piston Expander working with Low-GWP Fluids," in *5th International Seminar on ORC Power Systems*, 2019.

[133] L. Guillaume, *On the design of waste heat recovery organic Rankine cycle systems for engines of long-haul trucks*. PhD thesis, University of Liege, 2017.